UNIVERSITY OF CALIFORNIA
RIVERSIDE

Solid State Materials for Hydrogen Production, Ionic Conduction and Oxygen Reduction

A Dissertation submitted in partial satisfaction
of the requirements for the degree of

Doctor of Philosophy

in

Materials Science and Engineering

by

Chengyu Mao

March 2016

Dissertation Committee:

- Dr. Pingyun Feng, Chairperson
- Dr. Yadong Yin
- Dr. Leonard J. Mueller

The Dissertation of Chengyu Mao is approved:

_____

_____

_____

Committee Chairperson

University of California, Riverside

Acknowledgement

The past five years are one of the most critical periods of my lifetime. It witnessed the grow of my knowledge, broaden my experience in life and deepen my understanding in philosophy. I could never reach the heights and explored the depths and finished my Ph.D. smoothly without the guidance, support, help and efforts of a lot of people.

First of all, my deepest gratitude and respect is to my mentor Prof. Pingyun Feng for her generous support, valuable guidance and infectious enthusiasm, both in academic and in life. Her endless patience and the enthusiasm towards work helped me overcome many difficulties during my Ph.D. Her creative idea and insightful guidance made my research much more productive. Her precious personalities also influenced me a lot in my daily life. She is definitely my role model in future life and career.

I am also grateful to Prof. Xianhui Bu at CSULB for his valuable discussions and suggestion that helped me a lot to solve problems in my research and deal with difficulties in life. It is my great luck and pleasure to have such a collaborator.

I am greatly indebted to many past and current members of Prof. Feng group and my collaborator for their creating a rich working experience, intellectual stimulation and friendship: Dr. Tao Wu, Dr. Qipu Lin, Dr. Fan Zuo, Dr. Quanguo Zhai, Dr. Xiang Zhao, Dr. Yang Hou, Dr. Le Wang, Dr. Aiguo Kong, Dr. Shoutian Zhen, Dr. Koroush Sasan, Dr. Jikai Liu, Dr. Xiao Wei, Dr Na Li, Dr. Lei Ge, Dr. Xiaoxin Zou,Dr. Zhonghua Li, Fei Bu, Xitong Chen, Yuan Wang, Kudla Ryan, Zhao Zhao and Shilei Xie. I thank Dr. Krassimir N. Bozhilov, Dr.

Ilkeun Lee and Mathias Rommelfanger for assistance in using facilities in CFAMM, Dr. Dan Borchardt for assistance in using optical facilities in Chemistry Department.

I am also thankful to my defense committee members – Professor Yadong Yin and Professor Leonard J. Mueller, for their valuable help, comments and advice on my study, research and dissertation.

There are many others who deserve many thanks. I would like to thank the staff in both Materials Science and Engineering Program and Depart of Chemistry for their kindly service and help.

Most importantly, I must thank my parents Yanchun and Nianqun who had brought me to this world for their understandings and continuous support, and all of other family members for everything they have done for me.

Last but not least, I thank Weili Miao, Zhiye Tang, Tingjun Wu, Qunchao Hong, Kelvin An and all friends who have helped me and shared my happiness and sorrow.

Dedication

To My FAMILY

ABSTRACT OF THE DISSERTATION

Solid State Materials for Hydrogen Production, Ionic Conduction and Oxygen Reduction

by

Chengyu Mao

Doctor of Philosophy, Graduate Program in Materials Science and Engineering
University of California, Riverside, March 2016
Dr. Pingyun Feng, Chairperson

Fuel cells convert chemical energy directly into electricity with high efficiency and low pollutant emission via redox reactions at the anode and cathode. The implementation of hydrogen fuel cell depends on the large scale production of hydrogen. Though ''hydrogen economy" scenario looks attractive, a breakthrough in hydrogen production. An efficient fuel cell is also dependent on a good ionic conductor between the electrodes and good electrocatalysts for oxygen reduction reactions.

Artificial photosynthesis, which can convert solar energy directly into chemical energy is critical for sustainable energy supply and environmental conservation. Here, we demonstrate a facile synthetic method for generating one-dimensional crystalline rutile photoanode with simultaneous Ti^{3+} self-doping inside the sample. A subsequent

hydrothermal treatment in N_2H_4 can further enhance its performance in photoelectrochemical water splitting.

Additionally, we demonstrate an anion stripping method that convert neutral metal-organic frameworks into cationic ones. Anion conductivity can be potentially achieved for the first place in anion-conducting MOFs that could be utilized in anion exchange membrane fuel cells and reduce the usage of electrocatalysts.

Recently, MOFs have also been used as precursors or templates to synthesize new forms of porous carbons because they offer a number of unique advantages. One particular area in which MOF-derived heteroatom-decorated carbon materials can play an important role is the catalysis for oxygen reduction reactions. We report the synthesis, characterizations, and electrocatalytic activities of nitrogen doped hierarchically porous spherical carbon shells embedded with Fe nanoparticles through the simultaneous decomposition and evolution of an iron containing MOFs. Our strategy for MIL-100-Fe into ORR catalysts with specific morphology can also be extended to an enormous pool of MOF materials, which provides an avenue to develop various doped carbon materials for fuel cells and other applications.

Table of Contents

List of Figures

Chapter 1
An Overview of Technologies for Fuel Cell

1.1 Fuel cell technology

Fuel cells convert chemical energy directly into electricity with high efficiency and low pollutant emission via redox reactions at the anode and cathode.[1] Unlike batteries, fuel cell is an open system where the electrodes are charge-transfer media while active species undergoing the redox reactions are fed from outside the cell. Taking hydrogen fuel cell for example (Figure 1-1), fuel (hydrogen gas here) is pumped onto the cathode and split into electrons and protons. While the electrons flow outside the anode, provide electricity power to the external circuit and finally end up at the cathode to reduce oxidant (e.g., oxygen and air), the protons would diffuse through the cell towards cathode and combine with the reduced species into water.[2]

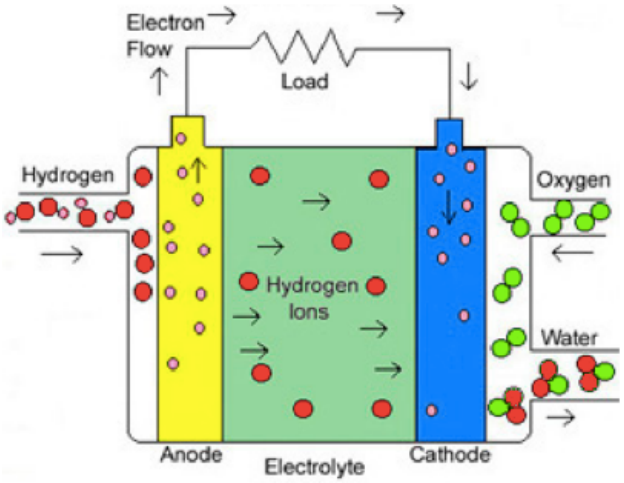

Figure 1- 1. Schematics of a fuel cell. Reprinted with permission from Ref 2. Copyright 2015 American Chemical Society

The US Department of Energy (DOE) has set up certain guidelines for fuel cell technology development. The current targets are to develop a fuel cell system for portable power (<250W) with an energy density of 900 Wh/L, and a fuel cell system for transportation with 60% peak efficiency, 5000 hour durable at the cost of $30/kW.[3] Not limited by Carnot cycle, fuel cell can be operating with high electricity efficiency of 60-70%, much higher than conventional engines in use today (Figure 1-2). If the waste heat can be collected and used, 90% efficiency is possible.[1]

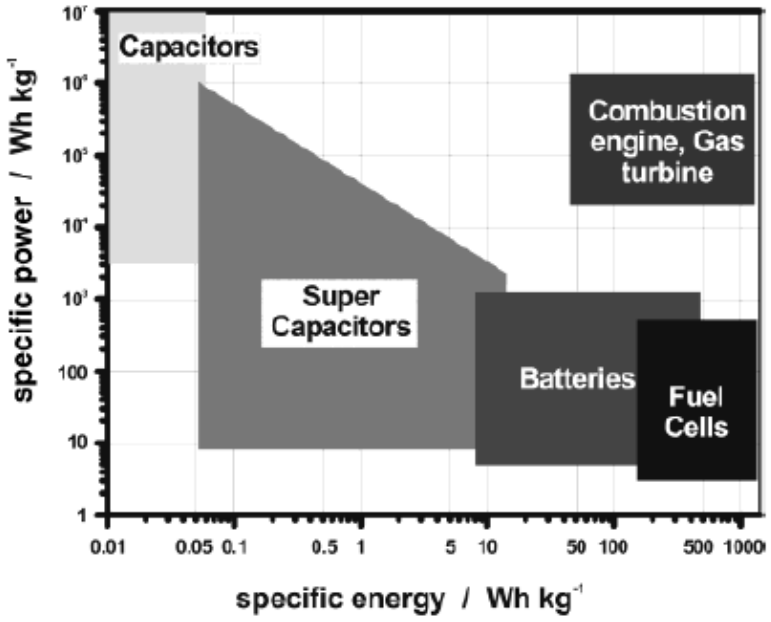

Figure 1- 2. Simplified Ragone plot of the energy storage domains for various electrochemical energy conversion devices compared to conventional thermal engines. Reprinted with permission from Ref. 1. Copyright 2004 American Chemical Society

The implementation of hydrogen fuel cell depends on the large scale production of hydrogen. Though ‘‘hydrogen economy” scenario looks attractive, a breakthrough in hydrogen production and storage has to be made.[4] Generating hydrogen from water by

using solar light will be discussed in the following part of this introduction, followed by solid ionic conductor and electrode materials, which are also critical for the fuel-cell technology.

1.2 Hydrogen production from direct water splitting by solar light

1.2.1 Photocatalytic water splitting

With the ever increasing global energy consumption, there has never been such an urgency to seek alternative clean and renewable energy to replace fossil fuel like coal, natural gas and crude oil. Efficient utilization of solar energy, which is irradiating the Earth surface ($1.3 \cdot 10^5$ TW) and exceeding the human energy consumption by four orders of magnitude, could alleviate current energy crisis and secure a sustainable growth.[5] Solar energy can be converted directly into electricity by photovoltaics cells. However, electricity is either not easy to store nor to distribute over a long distance. On the other hand, water splitting under solar irradiation has received much attention for large-scale production of renewable hydrogen, as demonstrated in Figure 1-3.[6] Unlike electricity, solar hydrogen is storable, transportable and can be used to generate electricity efficiently when it is combined with fuel-cell technology. Moreover, hydrogen is applicable as feedstock in modern chemical industry. It can also be used as a cheap reagent for the exothermic formation of methane, methanol or other hydrocarbons by recycling atmospheric CO_2 as carbon source.

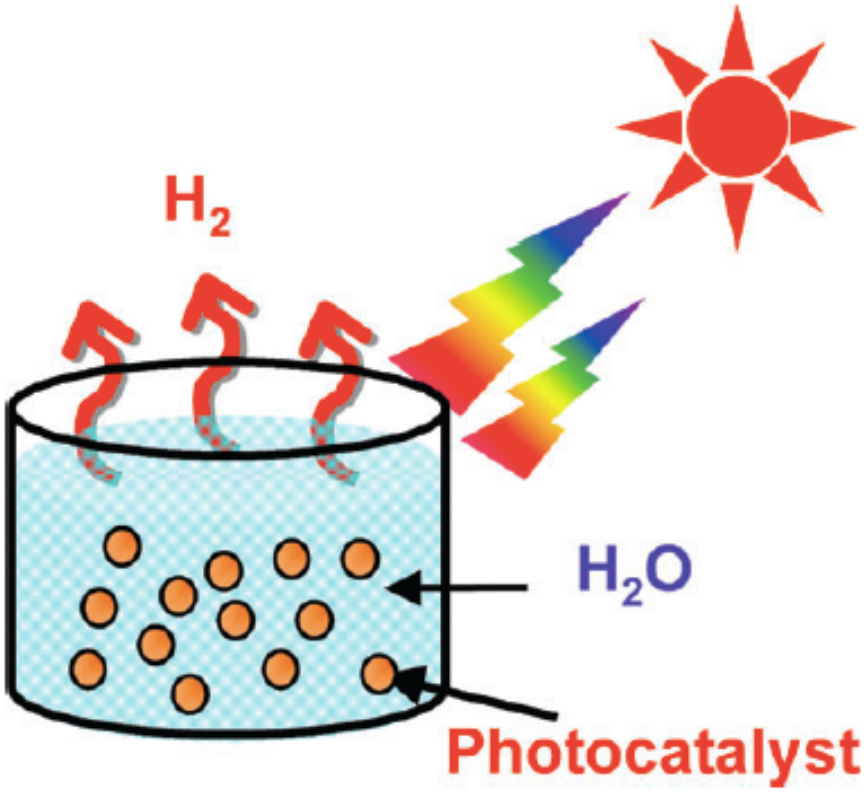

Figure 1- 3. Solar hydrogen production from water. Reprinted with permission from Ref.6. Copyright 2009 Royal Society of Chemistry

Since the first photo-assisted electrochemical water oxidation on TiO_2 electrode was discovered by Honda and Fujishima in the early 1970s[7] (Figure 1-4), photocatalytic and photoelectrochemical (PEC) water splitting on semiconductor materials are widely and extensively investigated.

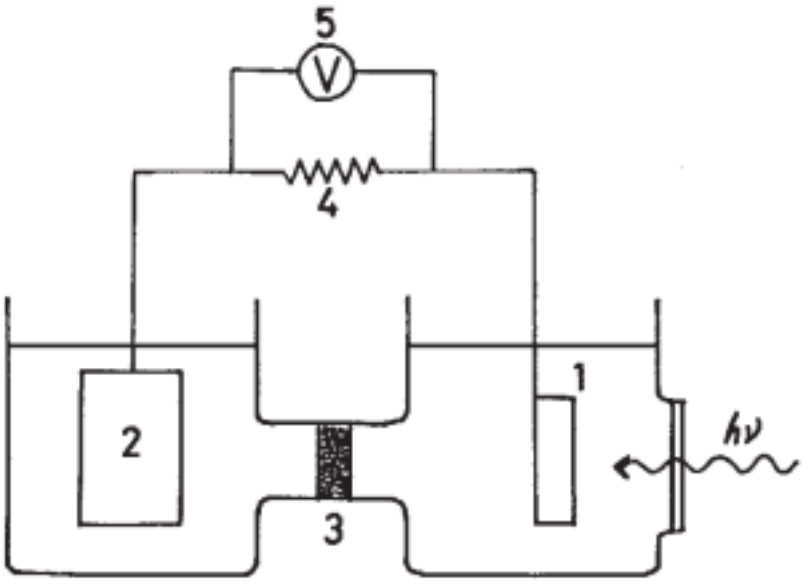

Figure 1- 4. Honda-Fujishima water splitting using a TiO_2 photoelectrode. Reprinted with permission from Ref. 7. Copyright 1972 Natural Publish Group

Splitting one molecular H_2O into hydrogen and oxygen is an uphill reaction in which 237 kJ/mol Gibbs free energy is required under standard condition, corresponding to 1.23 V per electron transferred according Nernst equation.

$$H_2O \rightarrow H_2 + \frac{1}{2}O_2, \qquad \Delta G = +237kJ\ mol^{-1}$$

However, water itself is transparent and can't absorb solar light. To drive the above reaction with light, a semiconductor material has to be used to absorb photons with energy higher than 1.23 eV and convert the energy into H_2 and O_2. When a semiconductor absorbs photons with energy higher than its band gap, electrons in the valence band will be excited into the conduction band, leaving equal amount of holes in the valence band. These photo generated electrons and holes can drive reduction and oxidation reactions

respectively, if the charge injections into corresponding reactants are thermodynamically favorable. The whole process described above for water splitting by the use of light is demonstrated in Figure 1-5.[5]

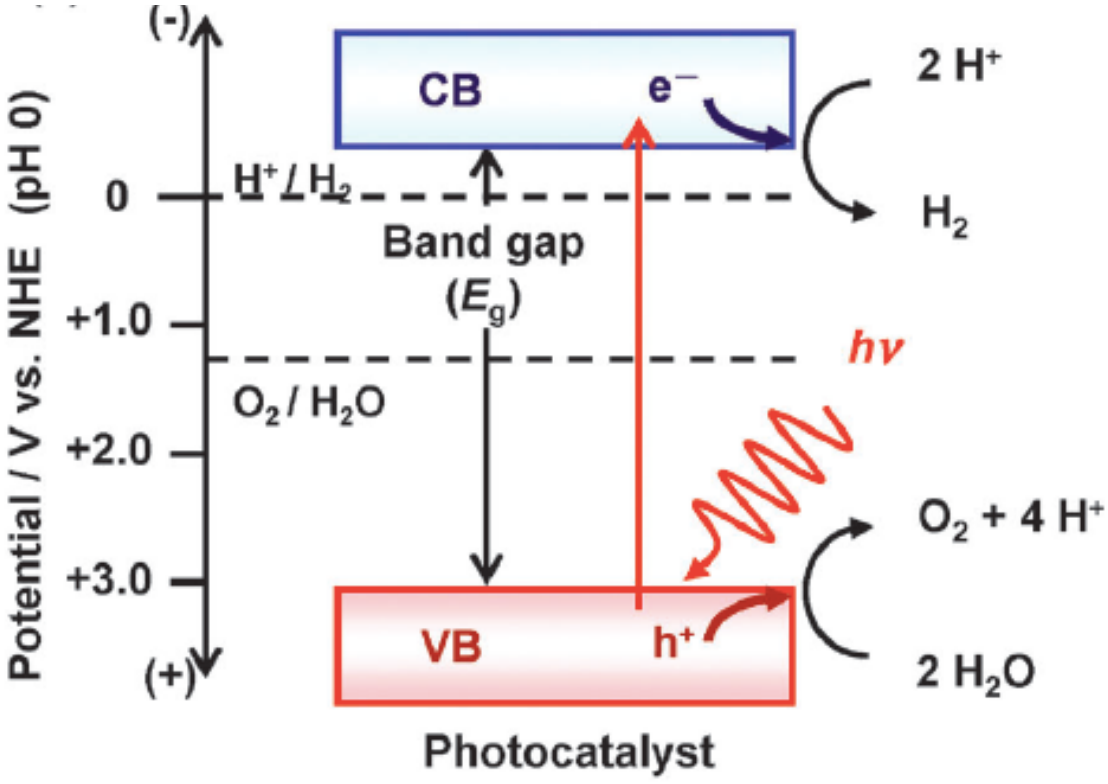

Figure 1- 5. Energy diagram of photocatalytic water splitting by a single semiconductor. Reprinted with permission from Ref.5. Copyright 2014 Royal Society of Chemistry

Ideally, a semiconductor can drive the hydrogen evolution reaction and oxygen evolution reaction from water under illumination if it has a conduction band (CB) more negative then H^+/H_2 redox potential and a valence band (VB) more positive than O_2/H_2O redox potential. Figure 1-6 shows band structure of commonly seen semiconductors and their relationship with redox potentials of water splitting.[6] However, photogenerated charge carriers (electrons and holes) within the semiconductor have to travel to

semiconductor-liquid junction in order to participate in the gas evolution reactions. Due to the concentrations and kinetic overpotentials required to drive forward the reactions, 1.6-2.4 eV per electron-hole pair generated is frequently reported to account for the losses.[8]

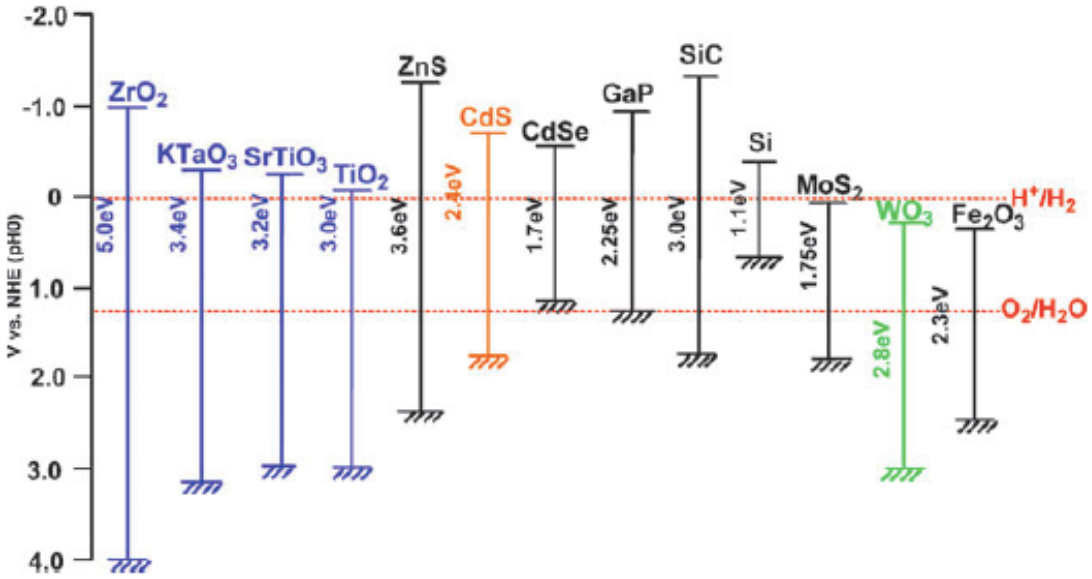

Figure 1- 6. Band structure of commonly seen semiconductors and their relationship with redox potentials of water splitting. Reprinted with permission from Ref.6. Copyright 2009 Royal Society of Chemistry.

Nature itself demonstrates its own effective strategy to utilize solar energy by spatially separating electron-involved reductions and oxygen evolution in photosystem I and II respectively. Similarity, multiple semiconductors can be connected in series, in which the reduction of water can occur on one photocatalyst concurrently with the oxidization of water on the other photocatalyst at the existence of revisable redox shuttle. In some cases, interparticle electron transfer is made possible by intimate contact between two

photocatalysts and the water splitting can proceed even in the absence of reversible redox shuttles. This configuration is proposed as "Z-scheme" and demonstrated by Figure 1-7.[5]

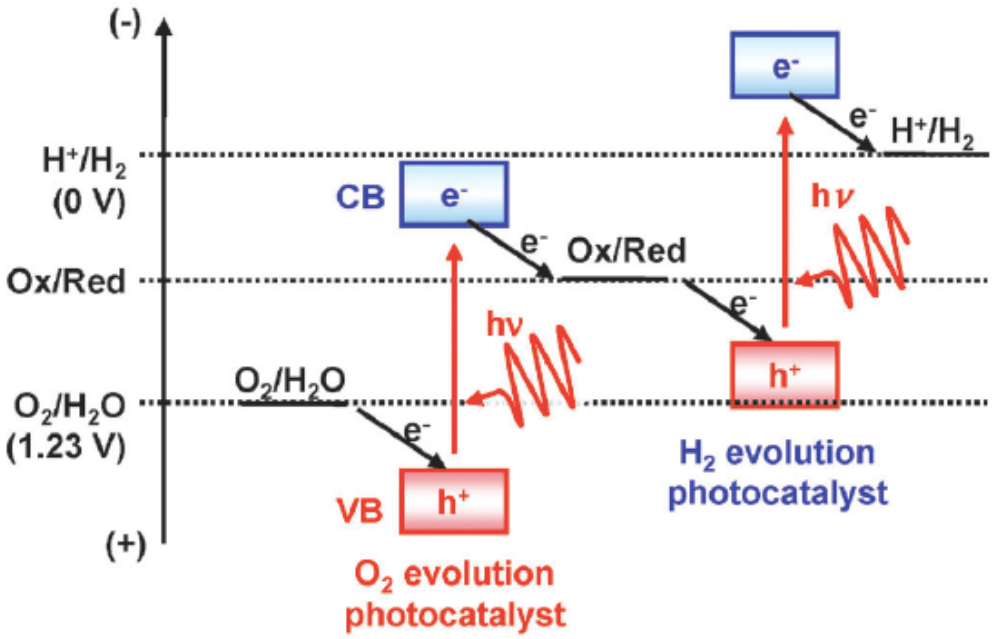

Figure 1- 7. Energy diagram of two semiconductors connected in series to split water with redox shuttle. Reprinted with permission from Ref.5. Copyright 2014 Royal Society of Chemistry

1.2.2 Photoelectrochemical water splitting

When a semiconductor electrode is immersed in an electrolyte, Fermi level of the semiconductor needs to be equilibrated with the redox potential of electrolyte solution so that electron transfer will take place between the semiconductor and the electrolyte solution. Such an electron transfer would cause band bending because electron density in a semiconductor is finite and the potentials of the band positions at the interfaces can be assumed to be pinned. The electric filed induced by the bending would play a critical

role in charge separation and photoelectrochemical reactions. For example, in n-type semiconductors, photoexcited holes will accumulate on the semiconductor surface and are consumed in oxidation reactions, while electrons are collected by back contact and transferred through the external circuit to a counter electrode and then used in reduction reactions (Figure 1-8, left). In such a case, the semiconductor only needs a valence band more positive than the oxygen evolution potential to oxygen generation. And this semiconductor is working as a photoanode in the PEC cell. [5]

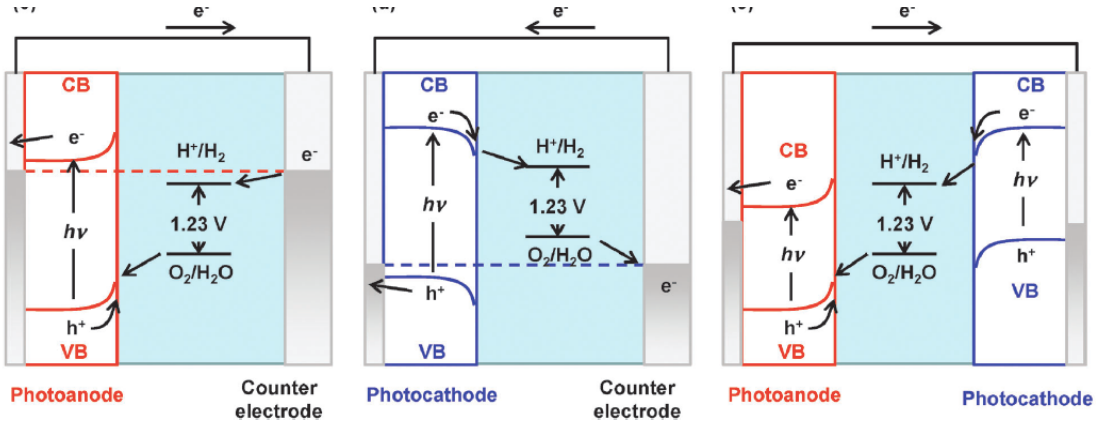

Figure 1- 8. PEC water splitting using photoanode (left), photocathode (middle) and photoanode and photocathode in tandem configuration (right). Reprinted with permission from Ref.5. Copyright 2014 Royal Society of Chemistry

On the other hand, a p-type semiconductor can work as a photocathode for hydrogen evolution if its conduction band edge is more negative than the hydrogen evolution potential (Figure 1-8, middle). Accordingly, water splitting reactions in a PEC cell are driven by photoexcited minority carriers. Even if the Fermi level of the photoelectrode is positioned at an undesirable potential, an external voltage can be applied to compensate the potential deficiency in order to drive the overall reactions. In such a case, the external

power input should be considered to compare the energy conversion efficiency. Alternatively, an n-type photoanode and a p-type photocathode can be connected in tandem (Figure 1-8, right). In this configuration, the efficiency of the PEC cell can be theoretically determined by the intersection of the steady current–potential curves of the respective photoelectrodes and highest efficiency can be obtained when two curves intersects closest to their individual maximum power points,[8] as shown in Figure 1-9.

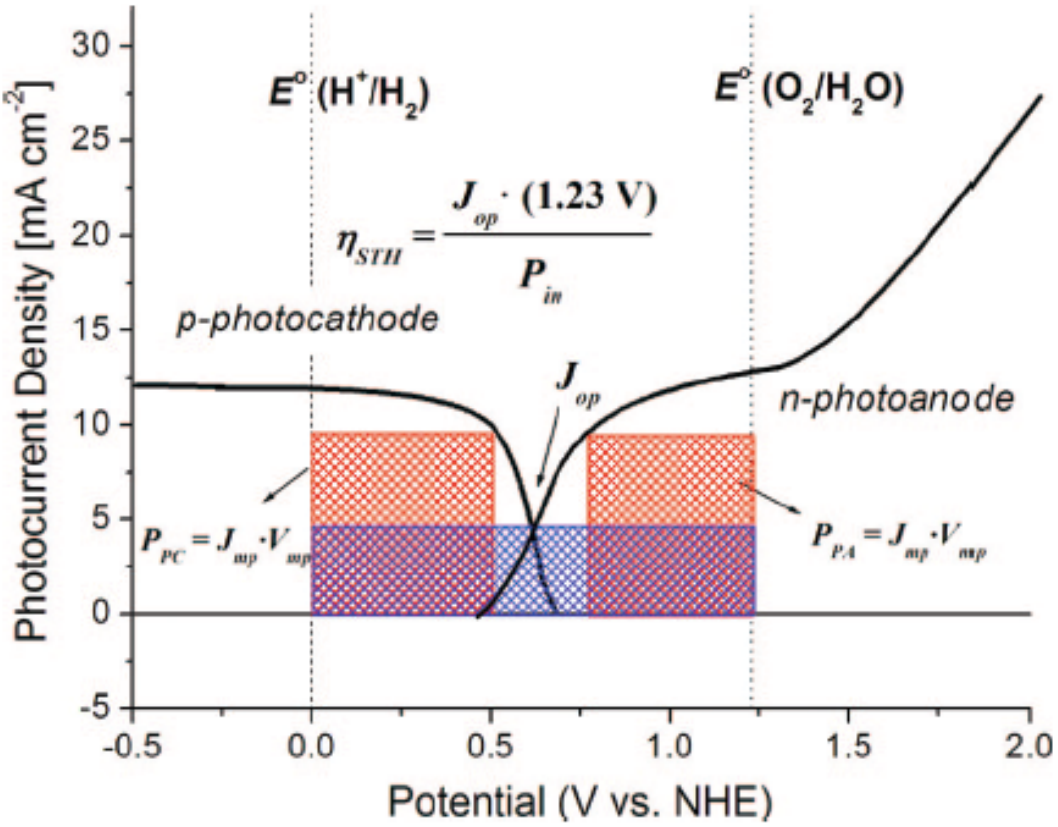

Figure 1- 9. Overlaid current density-potential behavior for a p-type photocathode and a n-type photoanode, with overall efficiency projected by the cell for water splitting. Reprinted with permission from Ref.8. Copyright 2010 American Chemical Society.

1.2.3 Factors affecting photocatalytic performance

Three major steps are critical in the photocatalytic process (Figure 1-12).[6] The first step is the absorption of photons and the formation of electron-hole pairs. Sunlight consists of three main categories of wavelengths (Figure 1-10): ultraviolet light (λ< 400nm), visible light (400 nm<λ< 800nm) and Infrared radiation (λ>800nm). They are accounting for 4, 53 and 43% of the total solar energy. The minimum band gap for water splitting is 1.23 eV, which is corresponding to the wavelength of 1100 nm.

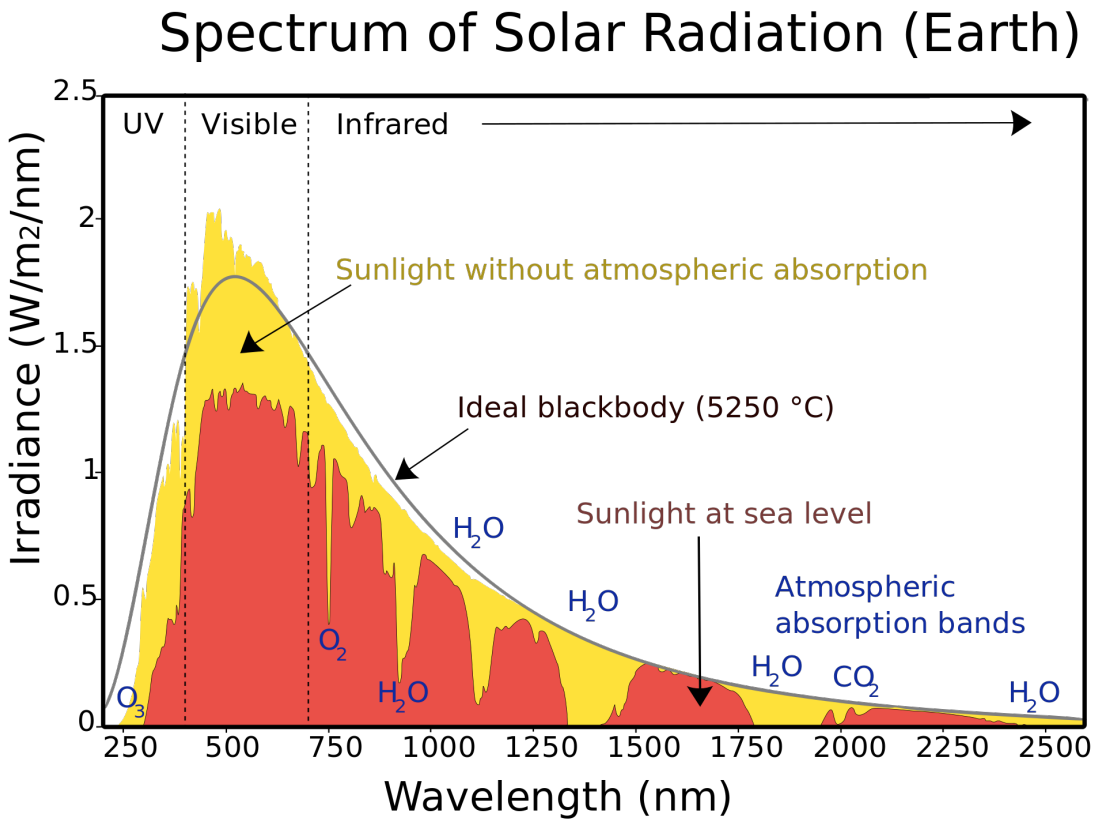

Figure 1- 10. Solar Irradiance (From Wikipedia)

Nevertheless, many photocatalytic materials are composed of metal cations at their highest oxidation states and have a band gap close to 3 eV, limiting the usage of solar light in a small portion of UV range. Therefor suitable band engineering is indispensable for the design of photocatalyst with visible light response. The relationship between the theoretical maximum efficiency of solar energy conversion for a single photocatalyst and its band gap is revealed in Schockley-Queisser[9] limit (Figure 1-11).

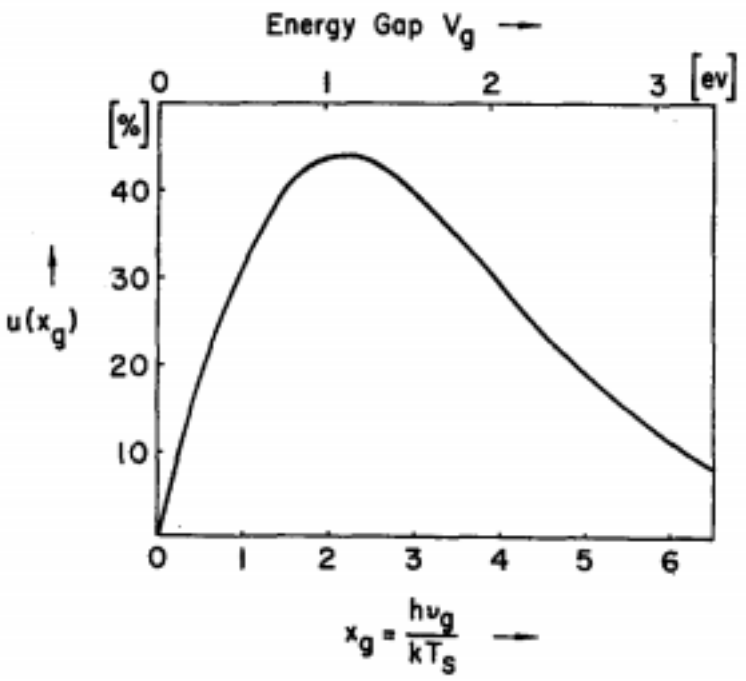

Figure 1- 11. The Shockley-Queisser limit. Reprinted with permission from Ref.9. Copyright 1952 the American Institute of Physics

The second step here is the separation of photogenerated charge carriers and the migration of them onto surface reactive sites. The recombination of photogenerated electrons and holes on defects, trapping sites or grain boundaries will result in a decreased photocatalytic activity. Suppression of the charge recombination can be

attempted in several ways: (1) the use of sacrificial agents to remove either electrons or holes so that half reaction of the water splitting can be separately studied; (2) fine control and tune of the morphology, crystallinity and size of the photocatalyst would allow to increase surface active site, shorten charge carrier diffusion pathways or reduce the recombination sites within the bulk; (3) the creation of heterojunctions or elaborate designed interfaces would create an internal force to separate electrons and holes.

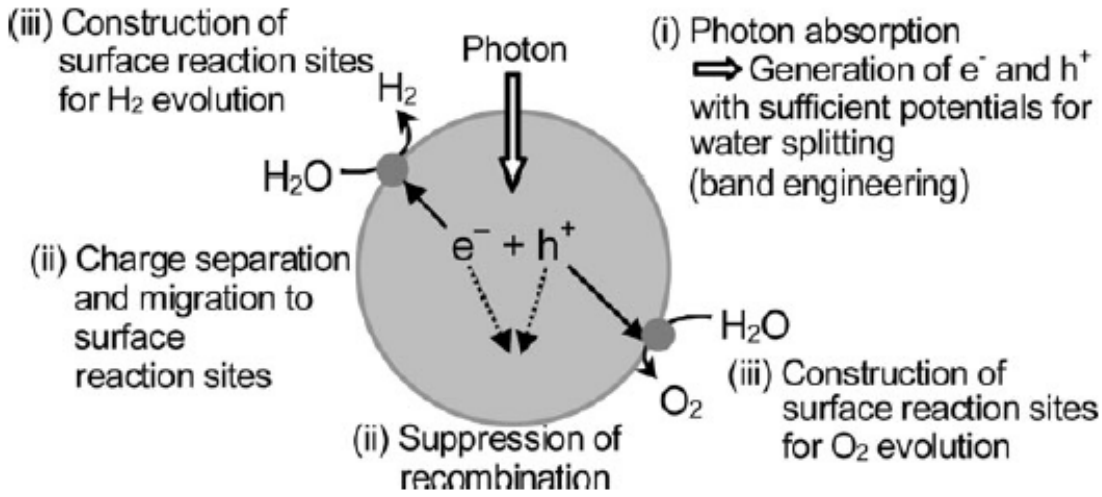

Figure 1- 12. Major process in photocatalytic water splitting. Reprinted with permission from Ref.6. Copyright 2009 Royal Society of Chemistry.

The third step involves the surface chemical reactions. Active sites and surface area are very important here since electrons and holes may still recombine with each other if active sites for redox reactions are not enough on the surface. Pt, NiO and RuO_2 are usually loaded to facilitate hydrogen evolution while IrO_2 and CoPi are effective to

catalyze oxygen evolution. However, backwards reaction between of H_2 and O_2 to form water has to be suppressed on the catalyst surface.

1.2.4 Evaluation of Photocatalytic and Photoelectrochemical Performance

A gas-closed circulation system equipped with a light-permitting reaction cell, a vacuum line and a gas carrying port which can inject the products into a Gas Chromatography (GC) for analysis is usually used to evaluate the performance of photocatalyst (Figure 1-13). Solar simulator is typically used to generate light and different light filters are applied to obtain light with specific wavelength.

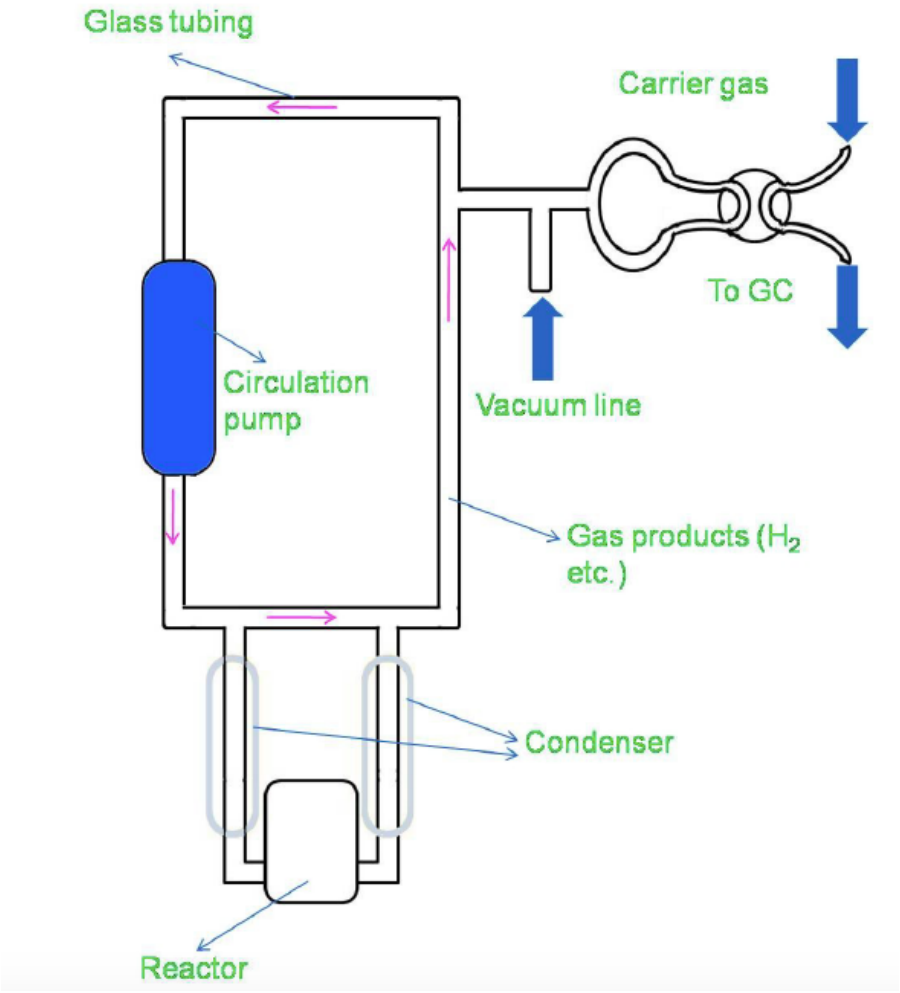

Figure 1- 13. Experimental set-up for photocatalytic activity test

A three-electrode photoelectrochemical cell is always configured to investigate the performance of photoelectrodes (Figure 1-14). The potential of a working electrode is controlled using a potentiostat with respect to a reference electrode, which commonly includes Ag/AgCl electrode and the saturated calomel electrode. The photocurrent and dark current are recorded as a function of potential against reference electrode or Normal

Hydrogen Electrode (NHE). Gases generated on each electrode can be collected and carried into GC for further analysis.

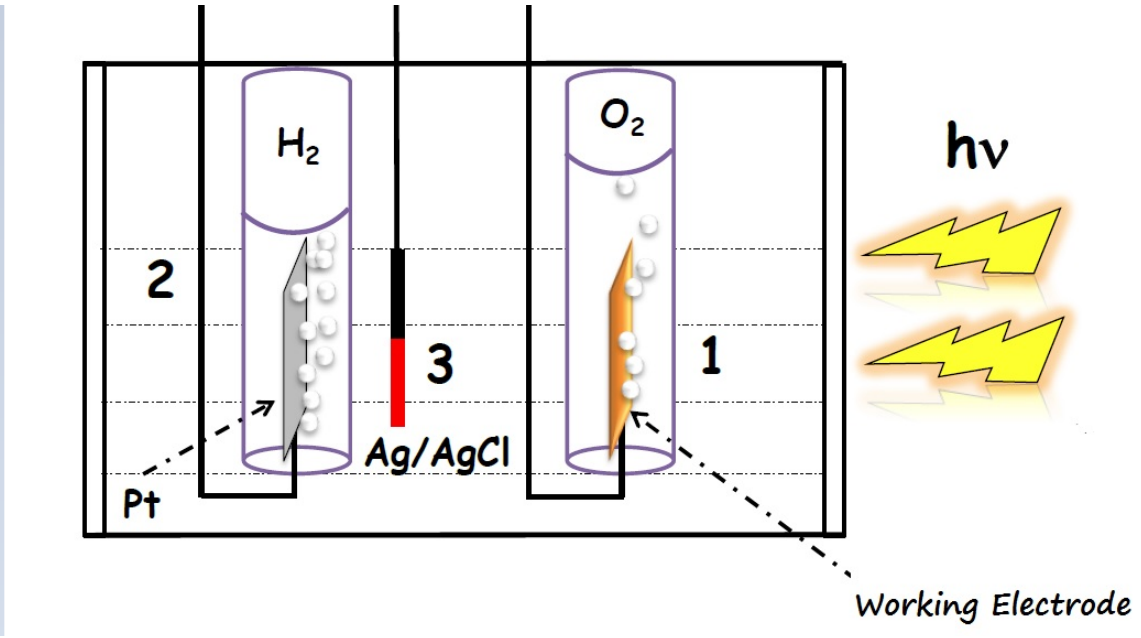

Figure 1- 14. Experimental set-up for PEC tests

Time course of H2 and O2 evolution, Solar to Hydrogen efficiency (STH), applied bias photo-to current efficiency (ABPE), incident photon-to-current efficiency (IPCE), turn over number (TON) and quantum yield (AQY) and Faraday Efficiency are usually applied to evaluate the performance of photocatalyst and photoelectrodes.

1.3 Ionic conductors in fuel cell

1.3.1 Electrolyte for fuel cells

Fuel cells are operating on a fuel component such as hydrogen, methane and methanol and an oxidant such as air or pure oxygen. Interim there is an electrolyte transferring charges between a negatively charged anode and a positively charged

cathode. Fuel cells are typically classified into several major types by the electrolyte[4] (Figure 1-15), which are alkaline fuel cell (AFC), polymer electrolyte fuel cell (PEMFC), molten salt fuel cell (MCFC) and solid oxide fuel cell (SOFC). AFC is one of the oldest fuel cell type and was used in Apollo missions. The facile hydrogen and oxygen kinetics in alkaline conditions results in a higher voltage. MCFC operating at 500°C finds its application in energy storage due to its higher efficiency and less demand on catalyst. Whilst SOFC working at 800-1000 °C depends on the O^{-2} conduction in the solid phase.

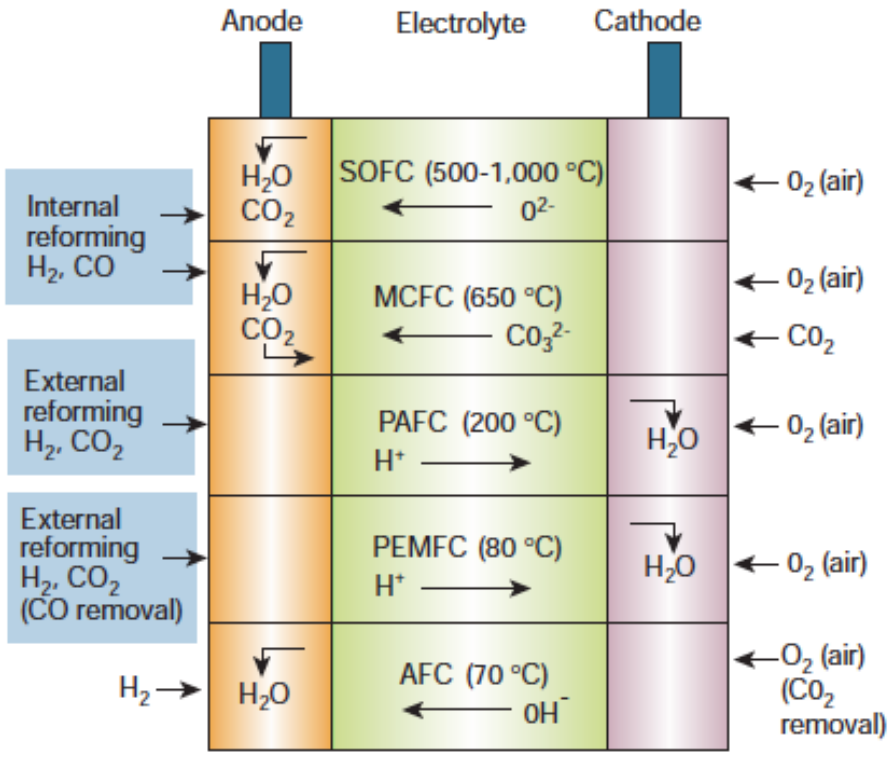

Figure 1- 15. Summary of Fuel Cell Types. Reprinted with permission from Ref.4. Copyright 2001 Nature Publishing Group.

PEMFC is the most important fuel cell systems. There are several criterions for a good electrolyte, among them are high conductivity to facilitate efficient charge transportation,

good chemical and thermal stability under fuel cell operating conditions, enough strength to act as a gas separator and compatibility with other fuel cell components. Nafion, polybenzimidazole (PBI) and ceramic oxides are demonstrated to be good electrolyte candidates in fuel cells[10] (Figure 1-16).

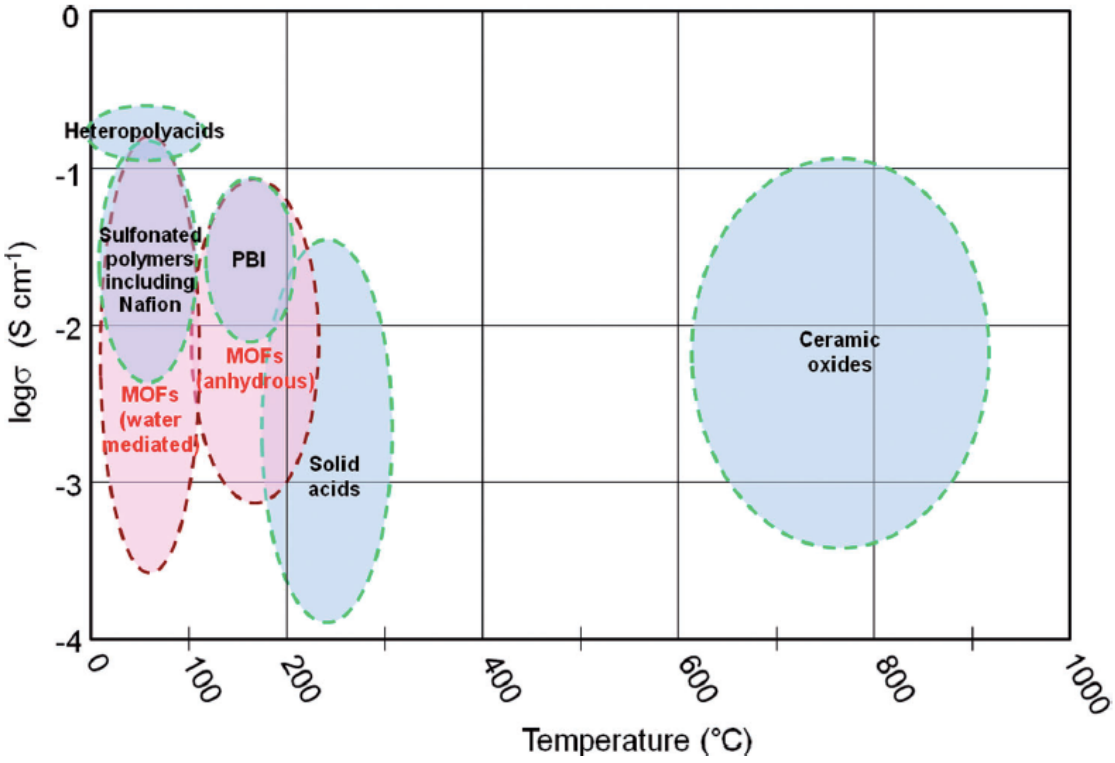

Figure 1- 16. Conductivity of various solids and their operating temperatures, Reprinted with permission from Ref.10. Copyright 2013 Wiley Online Library

1.3.2 Metal Organic Frameworks and their applications as proton conductor

Metal-organic frameworks (MOFs) are crystalline hybrid materials consisted of metal cations or metal clusters as nodes and organic ligands as linkers. The composition and topology of MOFs can be carefully designed and fully controlled by using different starting materials and synthesis parameters. These networks are often porous with high surface

areas and precise pore distribution and are widely used for gas adsorption and separation, catalysis and so on. The rapid development of MOFs with well-defined pores and channels as conduction pathways opened up new opportunities in proton conducting materials. An increase in the number of charge carriers, greater motional entropy and lower activation energy are also beneficial for ionic conductions. Two types of proton conductions are observed and investigated in MOFs, one is the water-mediated proton conduction operated at lower temperature range[11] (20-80 °C) and the other is the anhydrous form working at an intermediate temperature range[12, 13] (100- 250°C).

Compound	T(°C)	RH(%)	σ(Scm^{-1})
CPM-103a (single crystal)	22.5	98	5.8×10^{-2}
CPM-103a (pellet sample at 50 Mpa)	22.5	98	0.23×10^{-2}
CPM-103a (pellet sample at 68 Mpa)	22.5	98	0.65×10^{-2}
CPM-103b (single crystal)	22.5	98	4.7×10^{-2}
CPM-103b (pellet sample at 50 Mpa)	22.5	98	0.21×10^{-2}
CPM-103b (pellet sample at 68 Mpa)	22.5	98	0.59×10^{-2}
$\{[(Me_2NH_2)_3(SO_4)]_2[Zn_2(ox)_3]\}$	25	98	4.2×10^{-2}
$H^+@Ni_2(dobdc)(H_2O)_2$(pH = 1.8)	80	95	2.2×10^{-2}
PCMOF2$^1/_2$	85	90	2.1×10^{-2}
$H^+@Ni_2(dobdc)(H_2O)_2$ (pH = 2.4)	80	95	1.9×10^{-2}
$[In(imdcH)(ox)]\cdot(NH_4)$-$(H_2O)_{1.5}$(single crystal)	22.5	98.5	1.11×10^{-2}
$La(H_5DTMP)\cdot7H_2O$	24	98	8×10^{-3}
$(NH_4)_2(adp)[Zn_2(ox)_3]\cdot3H_2O$	25	98	8×10^{-3}
PCMOF-5	62	98	4×10^{-3}
Cu-TCPP nanosheet	25	98	3.9×10^{-3}
Cd-5TIA	28	98	3.61×10^{-3}
In-IA-2D-1	27	98	3.4×10^{-3}
$V^{II}[Cr^{III}(CN)_6]_{2/3}\cdot4.2H_2O$	50	100	3.4×10^{-3}
$[\{(Zn_{0.25})_8(O)\}Zn_6(L)_{12}(H_2O)_{29}$-$(DMF)_{69}(NO_3)_2]_n$	25	95	2.3×10^{-3}
$(NH_4)_4[MnCr_2(ox)_6]\cdot4H_2O$	40	96	1.7×10^{-3}
$Co^{II}[Cr^{III}(CN)_6]_{2/3}\cdot4.8H_2O$	35	100	1.7×10^{-3}
$MgH_6ODTMP\cdot6H_2O$	19	100	1.7×10^{-3}
β-PCMOF2	85	95	1.7×10^{-3}
$Fe(Ox)\cdot2H_2O$	25	98	1.7×10^{-3}
$[In(imdcH)(ox)]\cdot(NH_4)$-$(H_2O)_{1.5}$	23.5	98.6	0.82×10^{-3}

Figure 1- 17. A summary of the reported water-mediated highly proton conducting.[14]

The crystalline nature of MOFs also allows precise determination of their structures at atomic level, which provides a useful insight into the proton-conduction pathway and mechanism and can be useful in designing new proton-conducting materials. In addition, the fine tune of MOF structures, composition and properties provides an opportunity to control and improve the proton-conduction properties, which may be useful in further developing sensor and other devices. The above figure 1-17 summarizes the proton conductivity of various proton-conducting MOFs.[14] Our group also reported CPM-103a[14] (Figure 1-18) with the highest proton conductivity in MOF materials.

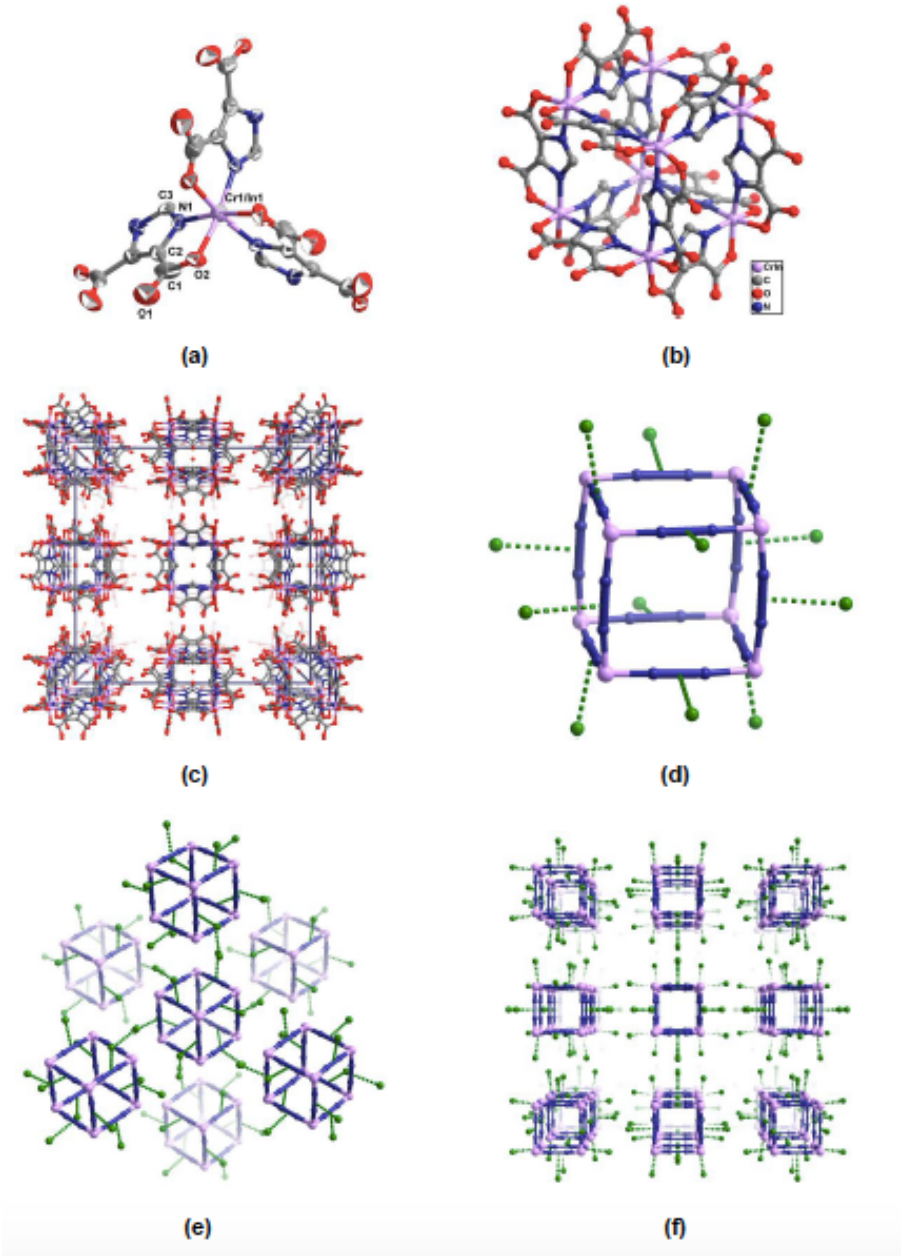

Figure 1- 18. (a) The coordination environments of metal centers in CPM-103a; (b) The structure of the In-Cr-cube; (c) 3D packing of the In-Cr-cubes; (d) The distribution of H atoms around each In-Cr-cube; (e) and (f) The schematic drawing of packing fashion in CPM-103a.[14]

1.3.3 Cationic MOFs with mobile anions

Unlike numerous reports on MOFs for ionic conductivity, anionic conductivity has not been thoroughly investigated. In general, cationic frameworks are much rarer than anionic or neutral ones. By encapsulating salts into pores of MOFs, anions can be introduced and conductivity was endowed onto MOFs.[15] We also developed an anion-stripping[16] method to strip immobile anions from the framework can create anionic conductivity. Preemptive coordination,[17] which refers to proactive blocking of metal coordination sites to preclude their occupation by neutralizing ligands is a newly developed strategy to create stable MOFs with high porosity and anion-exchange mobility (Figure 1-19).

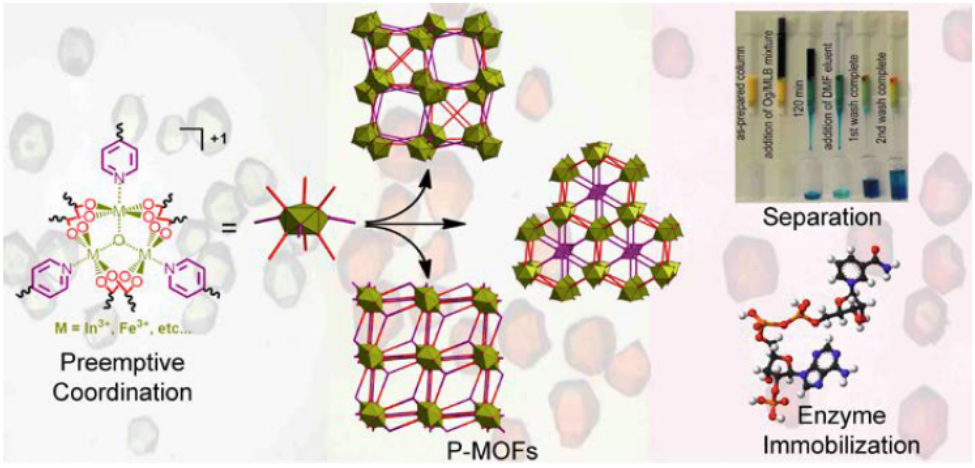

Figure 1- 19. Preemptive coordination that creates a series of highly porous cationic frameworks with anionic exchange ability.[17]

1.4 Noble-metal free electrocatalysts for oxygen reduction reactions

1.4.1 Platinum based oxygen reduction catalyst

Fuel cells can generate electricity directly by electrochemically oxidizing fuel and reducing oxygen into product. However, a four electron transfer to completely reduce oxygen into water is required, which is kinetic unfavorable and demands high activation energy. Also, there is alternatively two electron pathway to partially reduce oxygen into peroxide and energy loss would happen if this pathway is processed. As a result, efficient catalyst which can selectively catalyze full oxygen reduction into water is indispensable on the cathode. Conventionally, Pt has been considered to be the best catalyst for the oxygen reduction reactions (ORR). However, Pt is expensive and unevenly distributed on Earth. Its scarcity greatly limits its large-scale commercialization in fuel cell markets.

Numerous researches have been done to increase the activity and decrease the usage of Pt for ORR. Preparing Pt nanocrystals enclosed by high-index facets[18] with high density of atomic steps and dangling bonds can exhibit 400% higher catalytic activity (Figure 1-20).

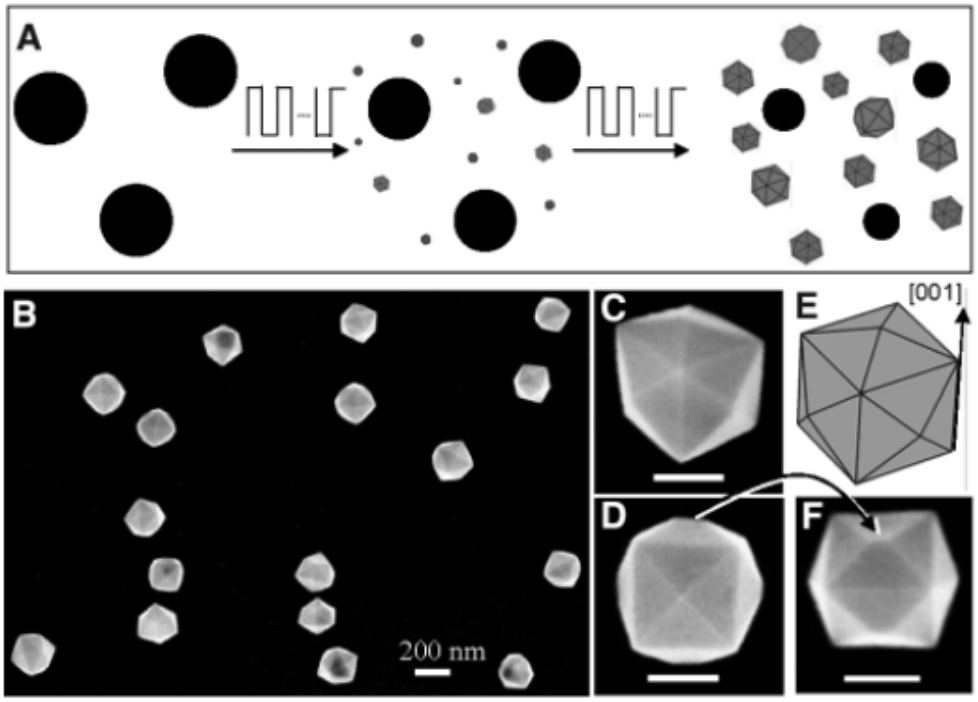

Figure 1- 20. Scheme of electrochemical preparation of Pt nanocrystals (A) and its SEM images (B, C, D, F). The geometrical model of an ideal nanocrystal. Reprinted with permission from Ref. 18. Copyright 2007 American Association for the Advancement of Science

Alloying Pt with non-noble metals like Ni and the formation of nanosegregated Pt skin structure over a bulky nanocrystal[19] can not only increase the ORR activity by orders of magnitude but also greatly reduce the usage of Pt metal (Figure 1-21). However, Pt cathode still suffer from its intrinsic problems including its susceptibility to time-dependent drift and CO deactivation. As a result, more efforts are needed to develop alternative Pt-free ORR catalyst which can have comparable or even better catalytic performance than Pt catalyst.

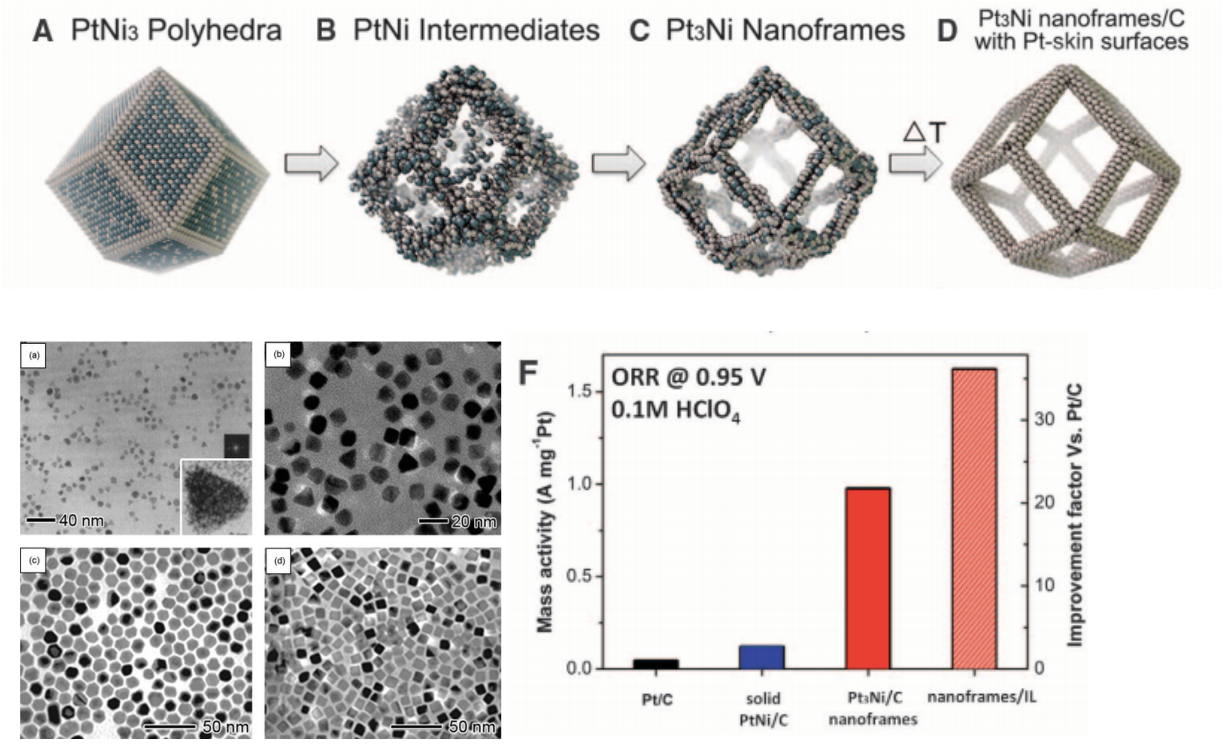

Figure 1- 21. Model Structure (top) and TEM images (bottom right) of Pt_3Ni nanoframe covered with Pt skin. Mass activities of different catalysts measured at 0.95V vs. RHE in acidic electrolyte (bottom right). Reprinted with permission from Ref. 19. Copyright 2014 American Association for the Advancement of Science

1.4.2 Progress in Noble-metal free catalysts

One of the most promising noble-metal free electrocatalysts[20] is carbon-supported metal/nitrogen ($M\text{-}N_X/C$) materials (M= Co, Fe, Ni, Mn, etc.). These materials are usually formed by the pyrolysis of a variety of metal, carbon and nitrogen precursors, which are abundant and inexpensive. $M\text{-}N_x$ active center is identified to be critical in such materials. The formation and mechanism of those active center by annealing or non-annealing methods are thoroughly investigated by numerous reports.

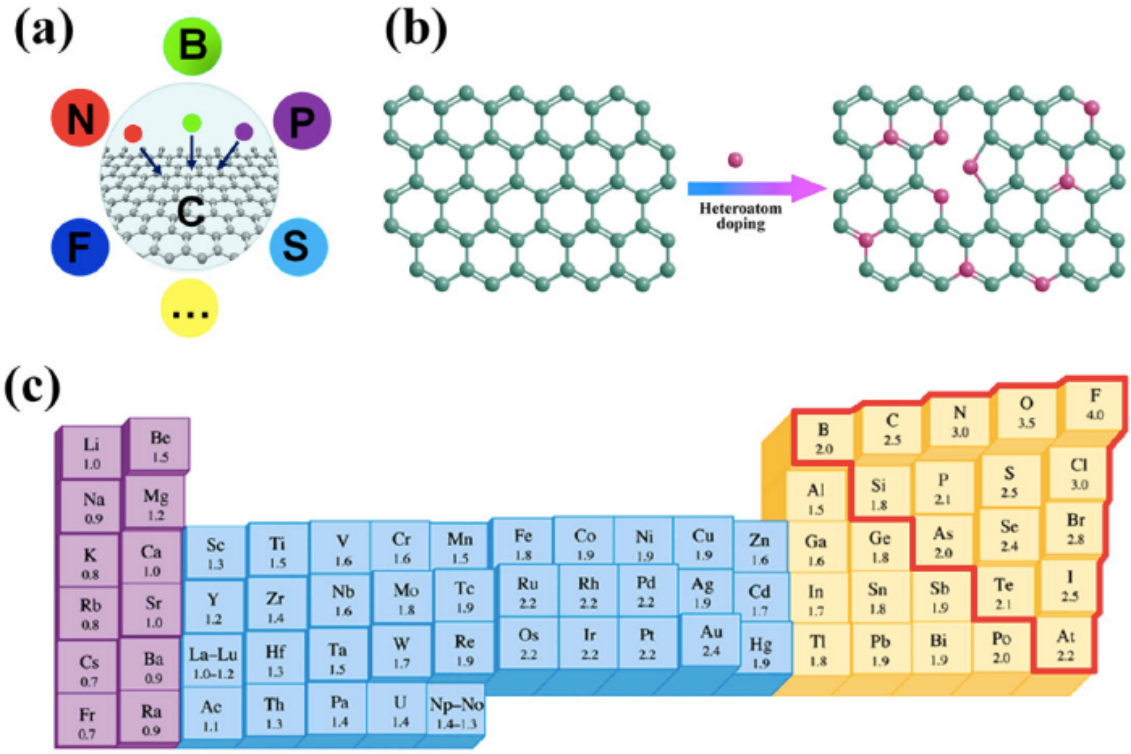

Figure 1- 22. Doping of carbon structures with heteroatoms (a, b) and periodic table with corresponding electronegativity of elements. Reprinted with permission from Ref.2. Copyright 2015 American chemical Society

Along with the progress in non-precious metal catalysts, metal-free electrocatalysts[2] based on carbon materials have been discovered and developed, which could dramatically reduce the costs and increase the efficiency of fuel cells. In particular, they have better long-term operational stability and are free from the CO poisoning and methanol crossover effect. Simulations and experimental observations reveal that heteroatom doping is beneficial for carbon materials. For example, N doping is believed to create net positive charge on its adjacent carbon atoms, which can change the O_2 chemisorption mode attract electrons from anode to facilitate the reduction reactions.

Recent researches further proved doping-induced charge transfer and its important role in catalytic activities (Figure 1-22). More significantly, spin distribution induced by heteroatom doping into carbon can not only impart high ORR activities but also create multifunctional catalysis such as oxygen evolution reactions (OER) or/and hydrogen evolution reactions (HER). With abundant carbon resources, a new class of carbon materials (Figure 1-23) including carbon nanotubes (CNT), graphite, graphene, carbon nitride and 3D carbon architectures is emerging as a rapidly developing field.

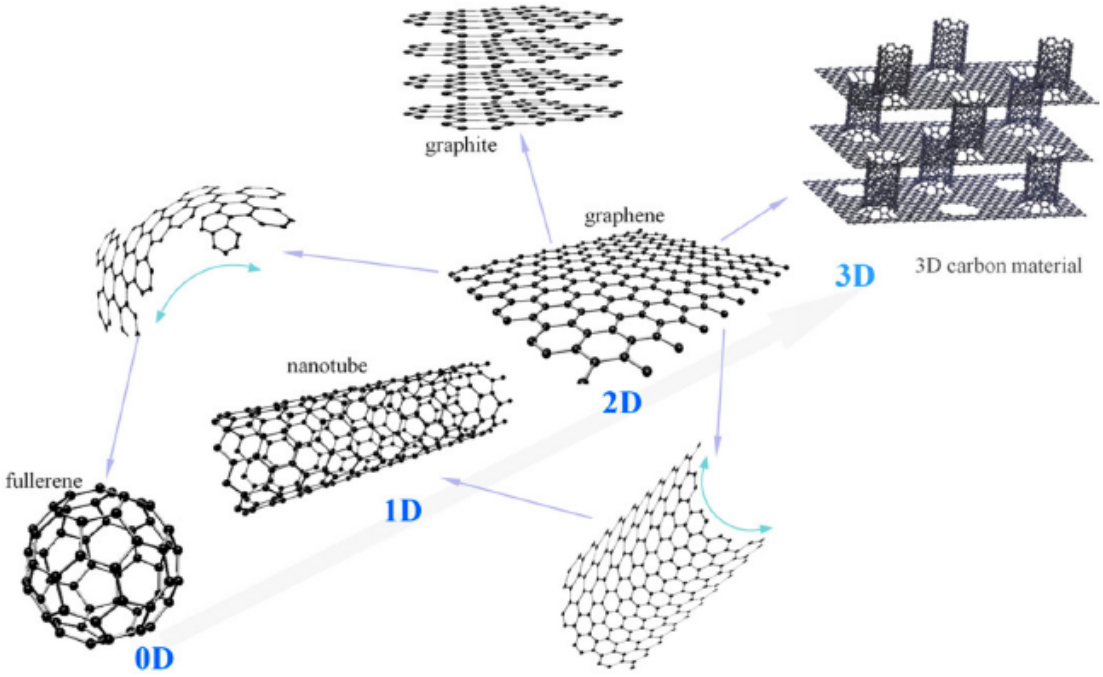

Figure 1- 23. Structures of carbon materials in different dimensions. Reprinted with permission from Ref.2. Copyright 2015 American chemical Society

1.4.3 Carbon materials made from metal organic frameworks

Efforts to construct nanoporous carbons with ordered pore structure and narrow pore size distributions have been employed due to their thermal and chemical stability. Given

their designable framework structures built by various metal nodes and organic ligands, Metal-organic frameworks (MOFs) have been considered as an alternative platform to construct nanoporous carbons, which may broad the library of nanoporous carbons with novel properties.[21] MOF-5, ZIF-8, CPMs (Figure 1-24) and various MOFs[21] have been demonstrated as promising precursors to yield porous carbon with high surface area, stable pore structure and exceptional properties. Template method, functionalization and direct carbonization are common strategies to make carbon materials from MOFs.

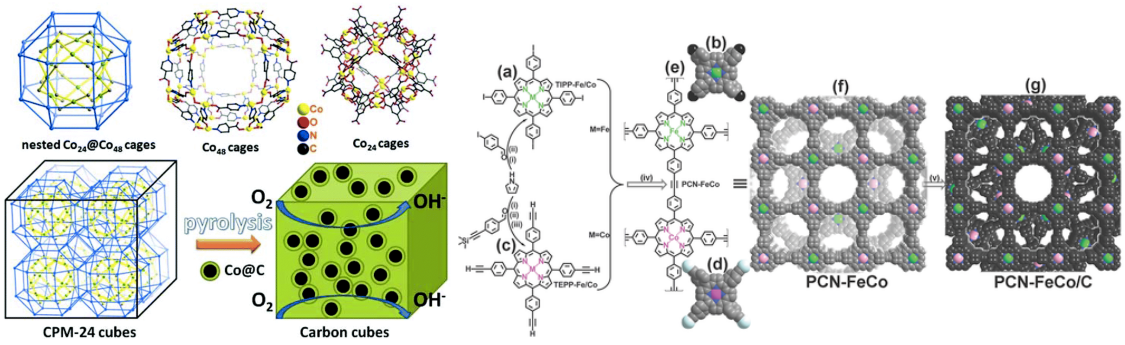

Figure 1- 24. Carbon Materials made from CPM-24 (left) and CPM-99 (Right) for Oxygen Reduction Reactions[22, 23]

1.5 Reference

1. Winter, M.; Brodd, R. J., Chem. Rev., 2004, 104 (10), 4245-4270.

2. Dai, L.; Xue, Y.; Qu, L.; Choi. H.-J.; Baek, J.-B., Chem. Rev., 2015, 115 (11), 4823-4892.

3. Ramaswamy, P.; Wong, N.E.; Shimizu, G.K.H.; Chem. Soc. Rev., 2014, 43, 5913.

4. Steele, B. C. H.; Heinzel, A., Nature, 2001, 414 (6861), 345-352.

5. Hisatomi, T.; Kubota, J.; Domen, K., Chem. Soc. Rev., 2014, 43 (22), 7520-35.

6. Kudo, A.; Miseki, Y., Chem. Soc. Rev., 2009, 38, 253-278.

7. Fujishima A., Honda K., Nature 1972, 238, 37-38.

8. Walter, M. G.; Warren, E. L.; McKone, J. R.; Boettcher, S. W.; Mi, Q.; Santori, E. A.; Lewis, N. S., Chem. Rev., 2010, 110 (11), 6446-6473.

9. Shockley, W.; Queisser, H. J., J. App. Phys., 1961, 32, 1961.

10. Yoon, M.; Suh, K.; Natarajan, S.; Kim, K., Angew. Chem. Int. Ed., 2013, 52 (10), 2688-700.

11. Morozan, A.; Jaouen, F., Energy & Environmental Science, 2012, 5 (11), 9269.

12. Hurd, J. A.; Vaidhyanathan, R.; Thangadurai, V.; Ratcliffe, C. I.; Moudrakovski, I. L.; Shimizu, G. K. H., Nat. Chem., 2009, 1 (9), 705-710.

13. Bureekaew, S.; Horike, S.; Higuchi, M.; Mizuno, M.; Kawamura, T.; Tanaka, D.; Yanai, N.; Kitagawa, S., Nat. Mater., 2009, 8 (10), 831-836.

14. Zhai, Q.-G.; Mao, C.; Zhao, X.; Lin, Q.; Bu, F.; Chen, X.; Bu, X.; Feng, P., Angew. Chem. Int. Ed. 2015, 54 (27), 7886-7890.

15. Sadakiyo, M.; Kasai, H.; Kato, K.; Takata, M.; Yamauchi, M., J. Am. Chem. Soc., 2014, 136 (5), 1702-5.

16. Mao, C.; Kudla, R. A.; Zuo, F.; Zhao, X.; Mueller, L. J.; Bu, X.; Feng, P., J. Am. Chem. Soc., 2014, 136 (21), 7579-82.

17. Zhao, X.; Mao, C.; Luong, K. T.; Lin, Q.; Zhai, Q.-G.; Feng, P.; Bu, X., Angew. Chem. Int. Ed., 2016, 55 (8), 2768-2772.

18. Tian, N.; Zhou, Z.-Y.; Sun, S.-G.; Ding, Y.; Wang, Z. L., Science, 2007, 316 (5825), 732-735.

19. Chen, C.; Kang, Y.; Huo, Z.; Zhu, Z.; Huang, W.; Xin, H. L.; Snyder, J. D.; Li, D.; Herron, J. A.; Mavrikakis, M.; Chi, M.; More, K. L.; Li, Y.; Markovic, N. M.; Somorjai, G. A.; Yang, P.; Stamenkovic, V. R., *Science,* **2014,** *343* (6177), 1339-1343.

20. Chen, Z.; Higgins, D.; Yu, A.; Zhang, L.; Zhang, J., Energy & Environmental Science 2011, 4 (9), 3167-3192.

21. Chaikittisilp, W.; Ariga, K.; Yamauchi, Y., J. Mater. Chem. A., 2013, 1 (1), 14-19

22. Lin, Q.; Bu, X.; Kong, A.; Mao, C.; Bu, F.; Feng, P., Adv. Mater., 2015, 27, 3431-3436.

23. Kong, A.; Mao, C.; Lin, Q.; Wei, X.; Bu, X.; Feng, P., Dalton Trans., 2015, 44, 6748-6754.

Chapter 2
Ti^{3+} Self-Doped TiO_2 Film with Enhanced Activity as Photoanode by N_2H_4 Reduction for photoelectrochemical water splitting

2.1 Introduction

Harvesting solar energy efficiently is critical for sustainable energy supply and environmental conservation.[1] Artificial photosynthesis, which can convert solar energy directly into chemical energy, has been extensively investigated.[2] Since its first report in 1972,[3] TiO_2 has been considered as a promising photoanode[4] for water oxidation because of its photostability, non-toxicity, and abundance. However, its large band gap limits its activity to only UV radiation, a small portion of sunlight. Furthermore, short electron-hole recombination lifetime and the resulting carrier loss during charge transport greatly diminish its photo-to-current conversion efficiency. These drawbacks impede the performance of TiO_2 and its application as an efficient photoelectrocatalytic material

Recent studies aimed at improving the performance of catalytic materials have been focused on the architecture of nanostructured materials[6] and elemental doping.[7] One-dimensional nanostructured TiO_2 such as nanowires,[8] nanotubes[9] and branched nanorods[10] can exhibit significant light absorption depth and short diffusion distance for charge carriers, facilitating light absorption and electron-hole separation simultaneously. Yun et al. found that the performance of PEC depends on the nanowire length and surfacing coating.[11] Shi et al. and Liu et al. reported the benefits of 3-D nanowires and cross-linked nanowires on PEC performance.[12] Core-shell nanowires[13] were also reported

as beneficial to water oxidation. In addition, foreign dopants such as C,[14] N,[15] F,[16] W,[17] and Sn[18] or Ti^{3+} self-doping[19] by hydrogenation,[20] electrochemical reactions[21] and chemical reductions[22] have been employed to extend the light absorption spectrum into visible range, and to enhance electronic conductivity as well as electron-hole separation efficiency. In some cases, the morphology and composition control can be achieved simultaneously, leading to enhanced water oxidation performance under sunlight illumination. Hoang et al. developed N-modified TiO_2 nanowires through nitridation in NH_3 flow.[25a] Wang et. al.[23] and Cho et al.[24]synthesized TiO_2 nanowires on FTO with oxygen vacancy through hydrogenation and CO flame reduction, respectively. Hoang et al. also made TiO_2 nanowires with synergistic Ti^{3+} and N doping.[25b]

Photoanodes mentioned above are generally prepared on fragile FTO and separate steps are often needed to obtain the desired morphology and doping level. Here, we demonstrate a facile synthetic method for generating one-dimensional crystalline rutile photoanode with simultaneous Ti^{3+} self-doping inside the sample. A subsequent hydrothermal treatment in N_2H_4 can further enhance its performance in water oxidation via improving Ti^{3+} concentration. We also show that this method can be applied to other well-developed TiO_2 materials, which makes our strategy versatile for improving the catalytic performance of TiO_2 based materials.

2.2 Experimental

2.2.1 Synthesis of Ti^{3+} doped TiO_2 nanorod and its reduced form on Ti film

A titanium foil (0.25mm thickness, 99.7% trace metal, Sigma-Aldrich) was first polished with alumina suspension (Allied, # 90-187505) and then cleaned by sonication in deionized water, ethanol and acetone, sequentially. The foil was dried in an Ar stream. The clean Ti foil was then cut into small pieces with a mass of 100 mg each. The small chip was placed in an autoclave containing 10 mL aqueous HCl solution (0.5M). The autoclave was placed in a pre-heated 220 °C oven for 18 h. After cooling down in air, the product was collected and washed with deionized water and ethanol several times, followed by drying in an Ar stream. A blue film was grown on the surface of substrate. The sample was annealed at 550 °C for 150 min in Ar stream. The obtained sample was labeled as R-TiO_2-F.

R- TiO_2-F obtained from the above procedures was placed in an autoclave containing 10mL aqueous N_2H_4 solution (20% by weight). The autoclave was placed in a pre-heated 220 °C oven for 20 h. After cooling down in air, the product was collected and washed with deionized water and ethanol several times to remove possible residual N_2H_4. The obtained sample was labeled as RR- TiO_2-F.

Powder samples for EPR measurement were prepared by the same reactants and heating parameters as the preparation of R- TiO_2-F except that 100 mg of Ti powder was used instead of 100 mg Ti foil. The as-prepared powder was recovered by filtration and

washed with deionized water and ethanol several times. The obtained sample is labeled as R- TiO_2-P.

20mg R- TiO_2-P obtained from the above procedure was placed in an autoclave with 10mL aqueous N_2H_4 solution (20% by weight). The autoclave was placed in a pre-heated 220 °C oven for 20 h. After cooling down in air, the product was collected and washed with deionized water and ethanol several times to remove possible residue N_2H_4. The obtained sample is labeled as RR- TiO_2-P.

RR- TiO_2-F or RR- TiO_2-P (film form or powder form) was placed in a 400 °C pre-heated oven for 1h. The sample was then taken out of the oven and cooled down in air. The obtained sample is labeled as RR- TiO_2-F-Air or RR- TiO_2-P-Air.

2.2.2 Synthesis of TiO_2 nanowire and its reduced form on FTO

TiO_2 nanowire was grown on FTO following previous reported procedure.[8a] 5 mL concentrated HCl (37% by volume) was mixed with 5 mL of deionized water in a beaker first. After stirring for 5 min, 167 μL Ti(Ⅳ) iso-propoxide was added into the beaker. The mixture was stirred for another 3h before being moved into an autoclave. A clean FTO substrate was immersed into the autoclave with the conducting side facing down. The autoclave was put in a pre-heated 200 °C oven for 90 min. After the autoclave was taken out and cooled down to room temperature, FTO substrate was recovered and washed with deionized water and ethanol. The FTO substrate was then dried in an 80 °C oven first,

followed by annealing in air at 400 °C for 1 h. The as-prepared sample was labeled as TiO_2-FTO.

TiO_2-FTO obtained from the above procedure was placed in an autoclave with 10mL aqueous N_2H_4 solution (20% by weight). The autoclave was placed in a pre-heated 220 °C oven for 20 h. After cooling down in air, the product was collected and washed with deionized water and ethanol several times to remove possible residual N_2H_4.The obtained sample was labeled as R- TiO_2-FTO.

2.2.3 Materials Characterization

The morphology of each product was characterized using a Philips FEI NNS450 field emission scanning electron microscope (FESEM). Powder X-ray diffraction data was collected using a Bruker D8 Advance powder diffractometer operating at 40 kV, 40 mA for Cu Kα radiation (λ=1.5418 Å). The UV-Visible absorption spectra were recorded on a Shimadzu UV-3101PC UV-Vis-NIR Spectrophotometer operating in the reflectance mode with application of the Kubelka-Munk equation. The electron paramagnetic resonance (EPR) spectra were recorded on a Bruker EMX EPR spectrometer at an X-band frequency of 9.3145 GHz, sweep width of 700.00 Gauss, and center field of 3380.00 Gauss. X-ray photoelectron spectroscopy (XPS) characterization was carried out by using a Kratos AXIS ULTRADLD XPS system equipped with an Al Kα monochromatic X-ray source, a 165-mm

mean radius electron energy hemispherical analyzer and the C1s peak at 284.6 eV as internal standard.

2.2.4 Photoelectrochemical Measurements

Photoelectrochemical measurements were carried out using a Solartron 1287 electrochemical interface analysis instrument operated with the CorrWare program in a standard three-electrode configuration with the samples used as photoanode, a Pt foil as counter electrode, and an Ag/AgCl electrode as the reference electrode. 1 M KOH (pH = 13.6) purged with Ar was used as the electrolyte. The measured potentials vs. Ag/AgCl were converted to reversible hydrogen electrode (RHE) scale via the Nernst equation $E_{RHE} = E_{Ag/AgCl} + 0.197 + 0.059pH$. A 150 W Xenon lamp (Newport, 69907) coupled with an AM 1.5G filter (Newport, 81094) was applied as the simulated sunlight source. Light intensity was adjusted to 100mW/cm^2 with a radiant power meter (Newport, 70260) combined with a probe (Newport, 70268). In addition, a filter (Newport, FR-GG400) designed to remove light below the wavelength of 400 nm was used on the Xenon lamp to produce a visible light source. The incident photon to current efficiency (IPCE) was measured under the same xenon lamp equipped with a monochromator (Newport, 74404). IPCE under each wavelength is determined by the equation

$$IPCE(\lambda) = \frac{1240I}{\lambda J_{light}(\lambda)}$$

where λ is the wavelength of incident beam, I is the photocurrent density at each specific wavelength and J_{light} is the irradiance at each specific wavelength.

Simulated photocurrent obtained by integrating the calculated IPCE multiplied by the AM 1.5G (ASTM G-173-03) solar energy flux was conducted by the following formula

$$I = \int_{300}^{500} \frac{1}{1240} \lambda IPCE(\lambda)E(\lambda)d\lambda$$

where $E(\lambda)$ is the solar irradiance at a specific wavelength.

The electrochemical impedance spectroscopy (EIS) was carried out using Solartron 1260 impedance analyzer in the frequency range of 10-2 to 105 Hz with an AC voltage amplitude of 50 mV. A DC bias of open circuit potential was applied to each sample in dark or under illumination, respectively. Mott-Schottky measurements were performed with a voltage of 50 mV at a frequency of 5 kHz under dark condition.

2.3 Results and Discussion

2.3.1 Analysis on reaction process

Rutile TiO_2 with Ti^{3+} self-doping was grown on a Ti foil substrate hydrothermally. In contrast to many previous reports requiring Ti(IV) sources such as Ti(IV) alkoxide and $TiCl_4$, Ti foil here plays a dual role as both substrate and Ti(III)/Ti(IV) source during the synthesis.[26] Unlike anodization and other synthesis strategies which involve electrochemical process or F-containing agents and would ultimately leads to anatase phase, Ti metal here was dissolved in dilute HCl aqueous solution and Ti(III)/Ti(IV) were formed spontaneously on the surface of Ti substrate and subsequently formed oxide

films, which then act as a protective layer to prohibit further dissolution of the Ti substrate.

The concentration of anions (Cl^-) plays a critical role in the synthesis. The doubling of [Cl^-] by adding NaCl without pH change can completely dissolve the substrate to give white powders while acids such as HNO_3 and H_2SO_4 with the same [H^+] produced no product. The as-formed Ti (IV) was partially reduced to give Ti^{3+} self-doped TiO_2 film on the Ti substrate. Unlike FTO glass that is easy to break or lose conductivity under the harsh conditions, Ti metal substrate is more stable and flexible for further treatment or device fabrication and maintains a good conductivity throughout these processes. Here, the as-prepared sample was annealed in Ar to further increase the contact with Ti substrate and to prevent possible loss of Ti^{3+} by oxidation in air and the resulting sample is denoted as R-TiO_2-F. Subsequent treatment via a strong reducing agent, N_2H_4, was conducted to generate TiO_2 (denoted as RR-TiO_2-F) films with higher Ti^{3+} doping level.

2.3.2 Structural analysis by X-ray Diffraction and Electron Microscopy

Ti foil turned from silvery to blue after the hydrothermal reaction due to the formation of Ti^{3+}/TiO_2 layer on the surface. PXRD confirms the formation of rutile TiO_2 (Figure 2-1). The strong Ti peak shows that the majority of the Ti substrate is preserved after the hydrothermal reaction.

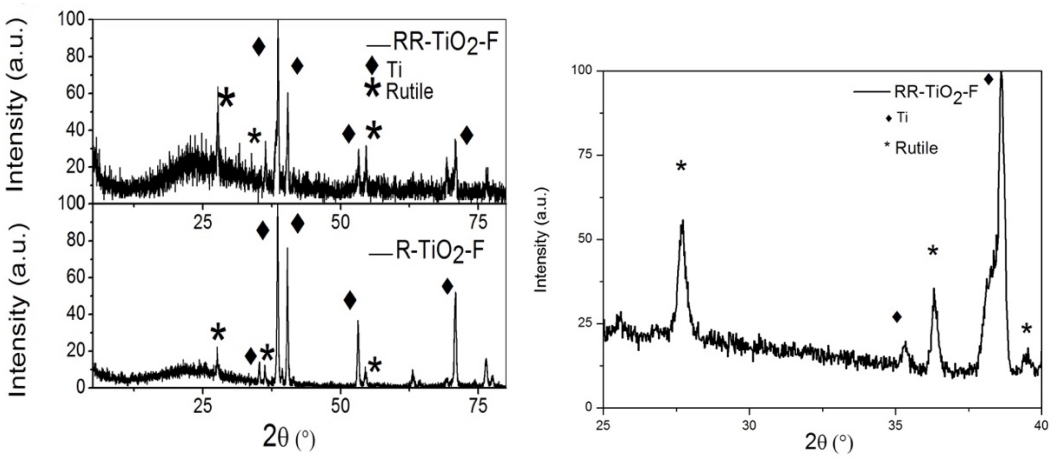

Figure 2- 1. Powder X-ray Diffraction (PXRD) of R-TiO_2-F and RR-TiO_2-F (Left) and enlarged RR- TiO_2-F (Right).

High-magnification SEM images (Figure 2-2a) reveal that the rutile film grown on the substrate has in fact a one-dimensional architecture with a pyramid-like end. The shape of the crystals grown on the substrate is similar to the previously synthesized bulk Ti^{3+}-doped TiO_2 with active facets.[27] Compared to most one-dimensional photoanode TiO_2 materials, the photoanode films synthesized here with clean surface and clear facets are unique and rare. The cross sectional image (Figure 2-2c) shows the interface between the surface structure and substrate, confirming our proposed layout. It is expected that such architecture could facilitate charge separation and efficient light adsorption compared to that of the bulk films and nanoparticles. From PXRD, no significant loss of crystallinity was observed for N_2H_4 treated samples RR-TiO_2-F (Figure 2-1), indicating the high chemical stability of the as-prepared sample. Furthermore, no shape and morphology change upon treatment was observed according to SEM image (Figure 2-2b).

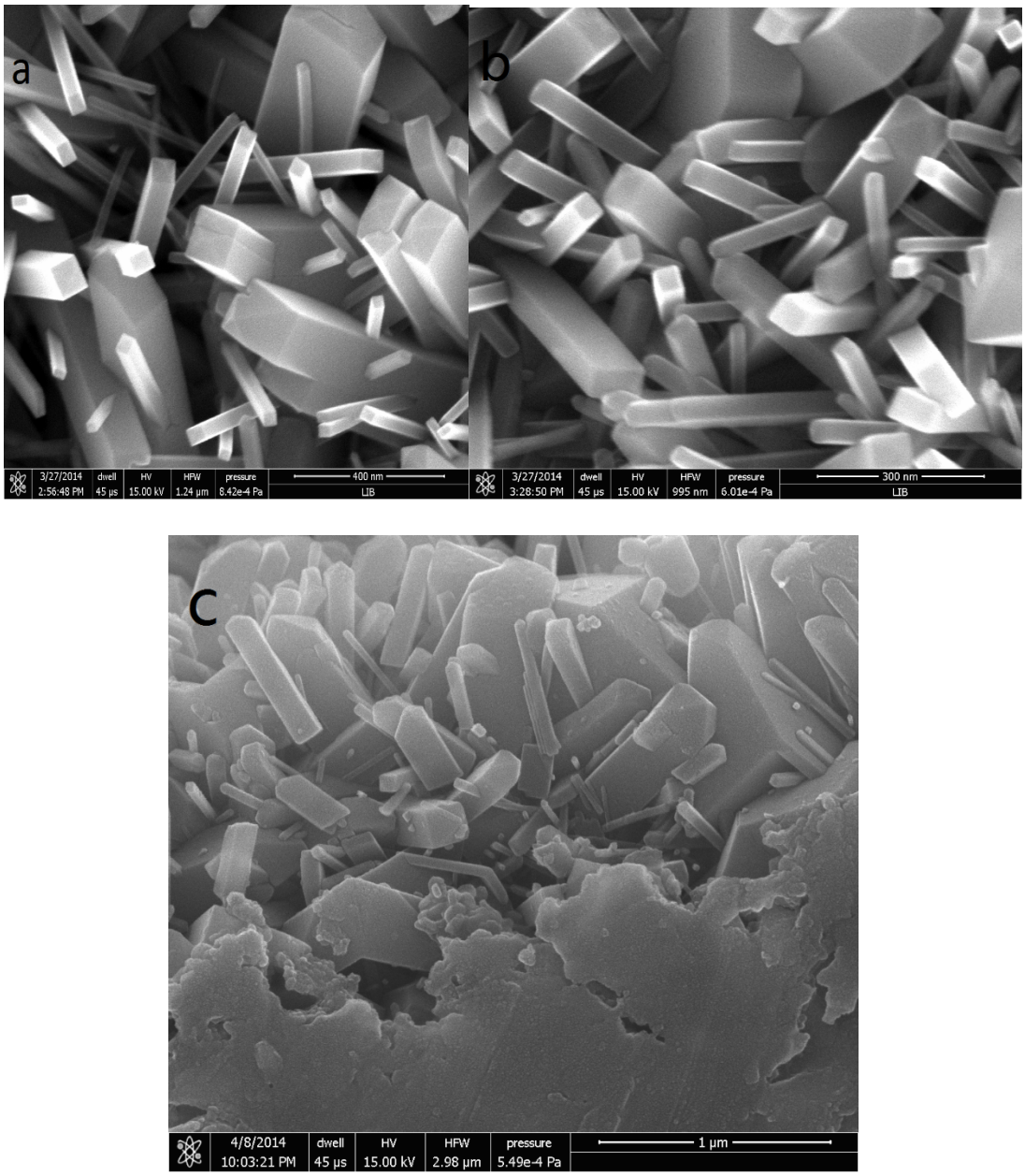

Figure 2- 2. Representative SEM images of R-TiO_2-F (a) and RR-TiO_2-F (b), cross-section SEM image of RR-TiO_2-F (c)

The pristine nanowire on FTO was prepared by a reported method, as described in the experimental section above.[11] Both XRD and SEM characterizations (Figure 2-3 & 2-4) confirmed the formation of nanowires on FTO.

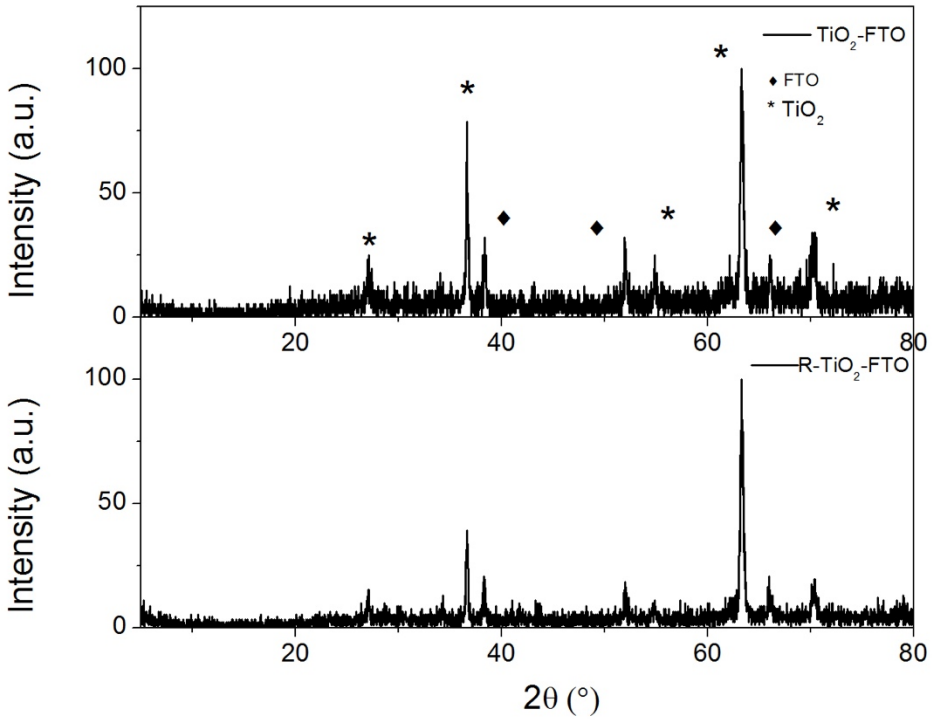

Figure 2- 3. PXRD patterns of TiO_2 nanowires grown on FTO

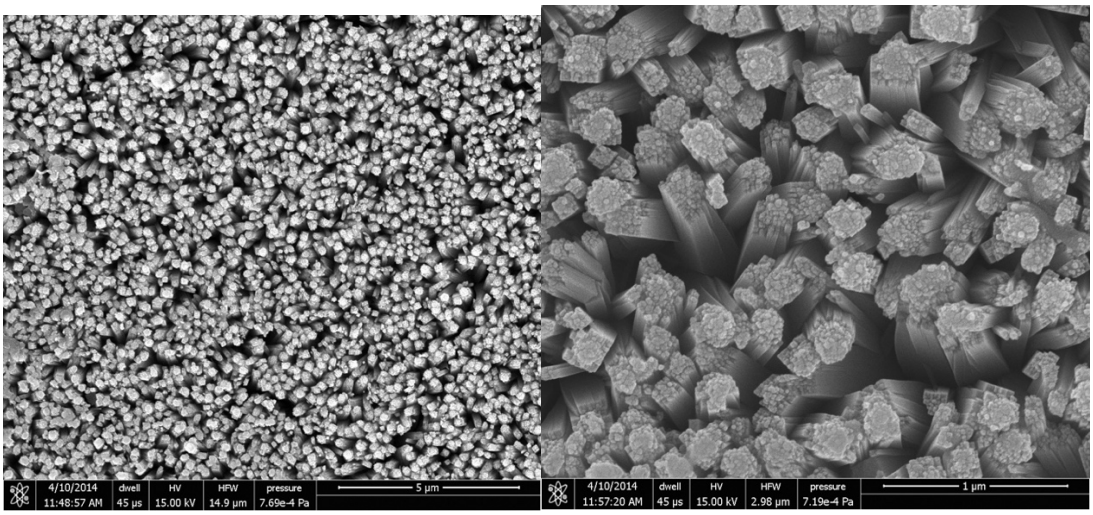

Figure 2- 4. SEM images of TiO_2 nanowires grown on FTO

2.3.3 XPS and EPR study

X-ray Photoemission Spectroscopy (XPS) was used to study the surface composition of the TiO_2 film grown on the Ti substrate. Ti $2p_{3/2}$ and O 1s XPS peaks (Figure 2-5) confirmed the formation of TiO_2. However, there is no XPS evidence for Ti^{3+}. This is because Ti^{3+} in the sample was embedded within the bulk and XPS only probes the surface. In addition, Ti^{3+} is susceptible to oxidation by O_2 in air and can't survive long on the surface.

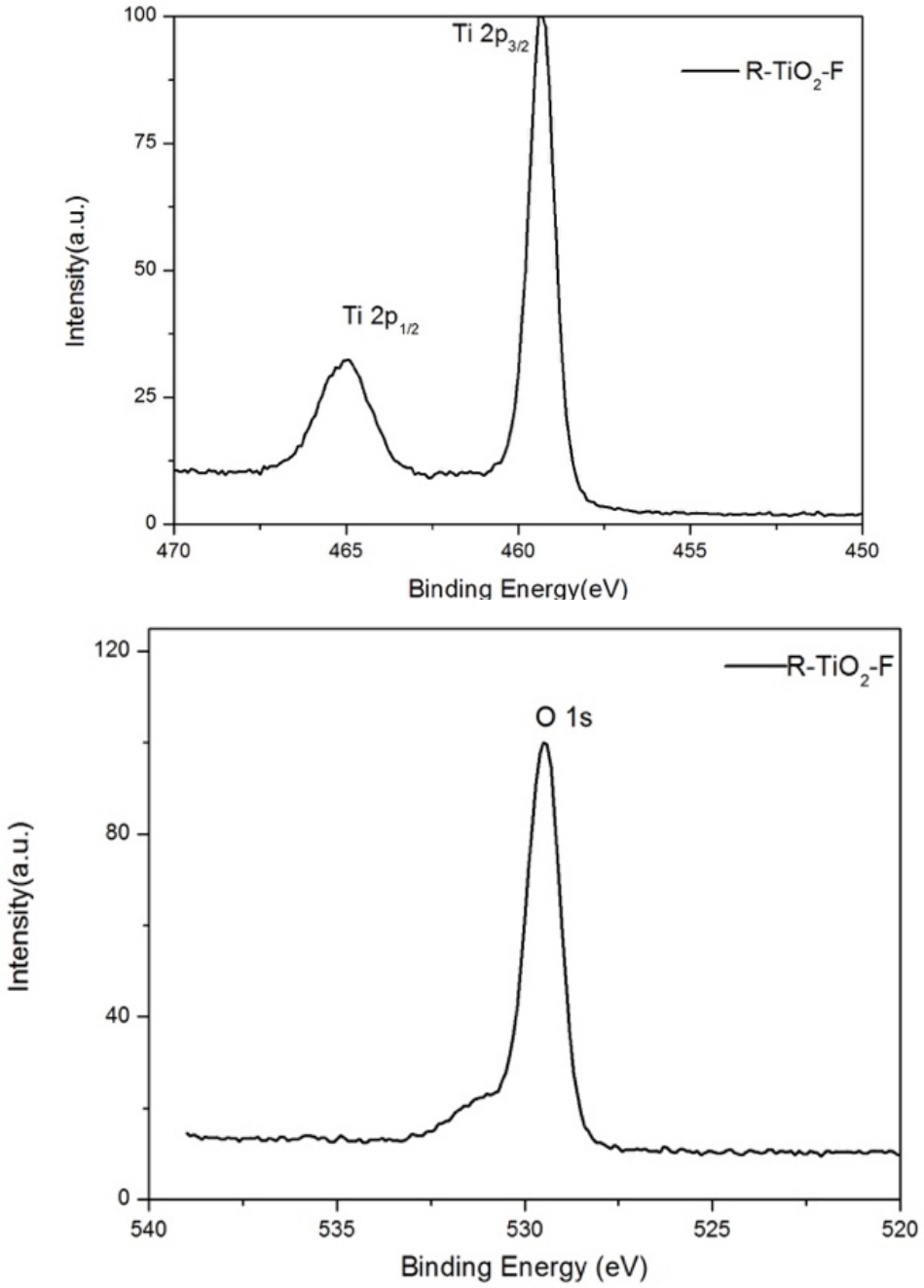

Figure 2- 5. XPS spectra of R-TiO_2-F, Ti 2p (top) and O 1s (bottom)

Here, electron paramagnetic resonance spectra (EPR) recorded at 100 K were used to verify the presence of Ti^{3+} in our sample. It is difficult to collect strong enough EPR signal from the film sample because only a thin layer was grown on the surface. Thus, powder samples were synthesized under exactly the same reaction conditions as those for the film except that the Ti foil was replaced by Ti powder in order to make enough samples for EPR data collection (details in SI). PXRD and SEM images (Figure 2-6) showed that the prepared powder samples have the same crystallinity and morphology as the sample on the Ti foil substrate.

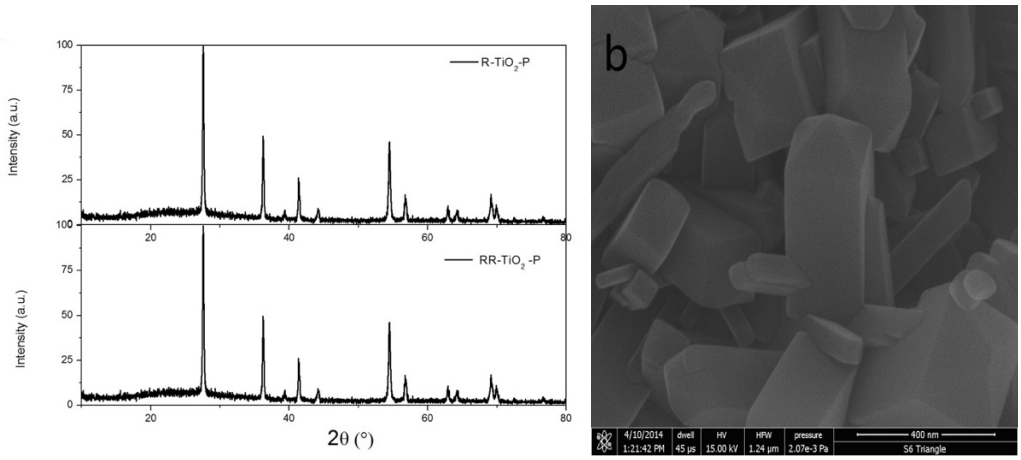

Figure 2- 6. PXRD patterns for R-TiO_2-P and RR-TiO_2-P (Left), SEM images for R-TiO_2-P

As shown in Figure 2-7, a prominent signal at g= 1.97 unambiguously proves the presence of Ti^{3+} in the bulk. A weak signal at g=2.007 may come from surface resonances[28] of the oxygen-centered surface hole trapping sites generated during the annealing process. An order of magnitude intensity improvement at g=1.97 for RR-TiO_2-P

demonstrates a much higher Ti^{3+} concentration after N_2H_4 treatment. The absence of signal at g=2.02 further excludes the existence of surface Ti^{3+}.

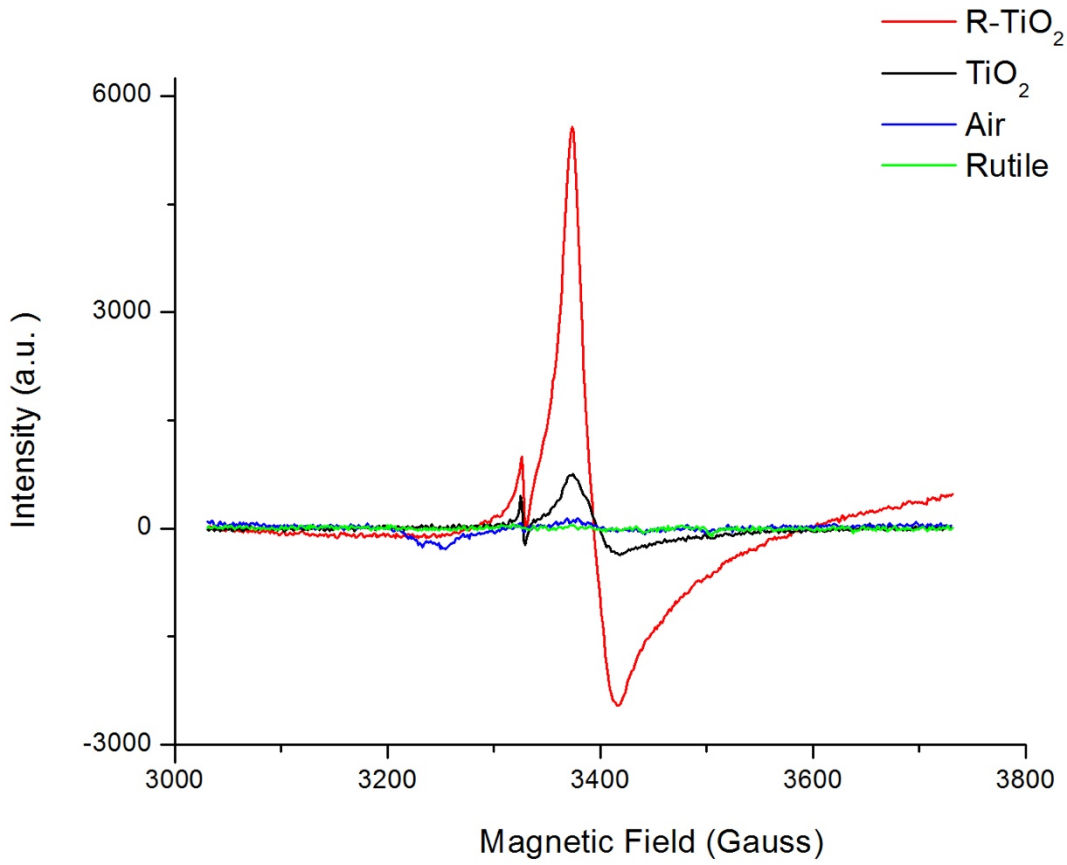

Figure 2- 7. EPR spectra (100 K) for R-TiO_2-P, RR-TiO_2-P, RR-TiO_2-P-Air and pristine rutile

2.3.4 Photoelectrochemical performance

To evaluate their water oxidation performance as a photoanode, PEC measurements were conducted in a three-electrode electrochemical system, using 1M KOH aqueous

solution as electrolyte and 100mW/cm^2 simulated sunlight illumination from a 150W xenon lamp coupled with an AM 1.5G filter (details in Experimental section).

Linear sweep voltammetry data from R-TiO_2-F and RR- TiO_2-F are shown in Figure 2-8a. The onset potentials are almost the same (0.26V and 0.23V vs. RHE, respectively), indicating a comparable surface kinetics. However, the photocurrent density almost doubled from 0.36 mA/cm^2 to 0.69 mA/cm^2 at 1.23V vs. reversible hydrogen electrode (V_{RHE}). Figure 2-8b shows the corresponding photoconversion efficiency η calculated by the equation: $\eta=J_{ph}(1.23-V_{RHE})/P$, where P is the power density of illumination light and J_{ph} is the current density. The optimum efficiency comes where enough photocurrent is generated while the applied bias doesn't negate the advantage of shining light. RR- TiO_2-F exhibits a peak value of 0.36% (0.49V vs. RHE), nearly tripling that of R- TiO_2-F, which is only 0.14% (0.53 V vs. RHE). Prompt and reproducible photoresponse upon illumination of both samples were revealed from the transient photocurrents measured at a fixed bias potential of 1.0V vs. RHE. As shown in Figure 2-8c, the rise and fall of the photocurrent corresponded well to the switching on and off of irradiation. The current densities for R-TiO_2-F and RR- TiO_2-F are 0.35 mA/cm^2 and 0.64 mA/cm^2, matching well with the results from linear sweep voltammetry.

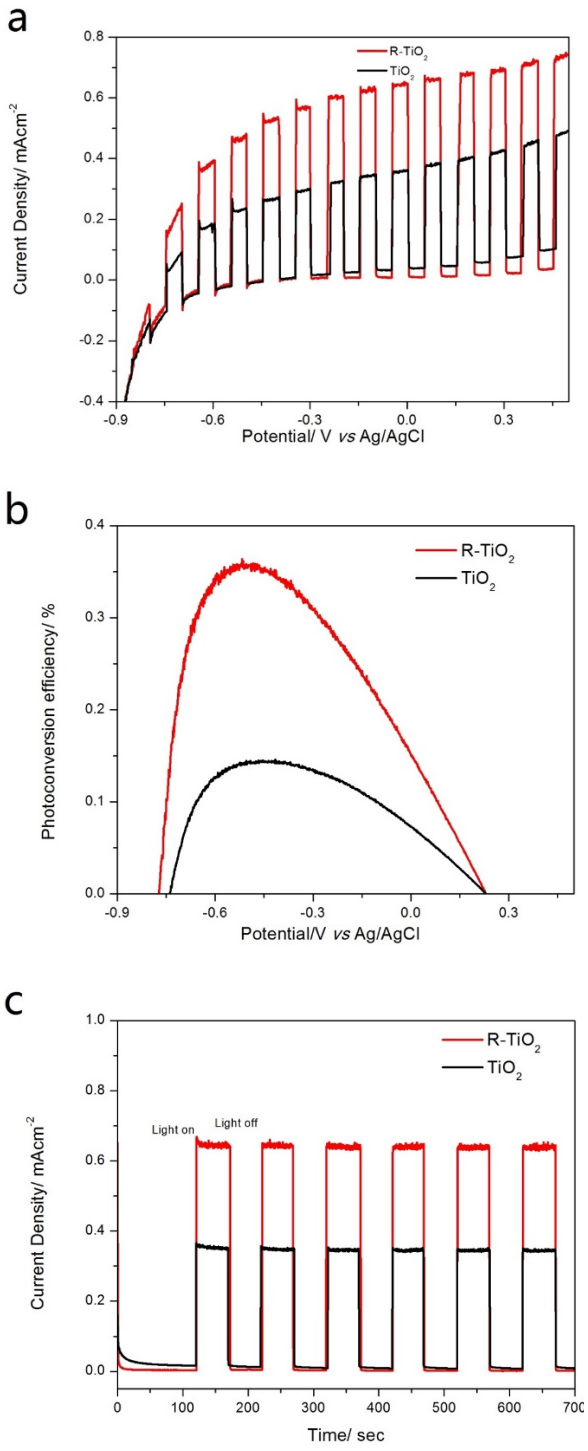

Figure 2- 8. Linear sweep voltammetry (scan rate of 10 mV/s) with chopped light (a); Photoconversion efficiency (b); Transient photocurrent density over time (c) for R-TiO_2-F and RR-TiO_2-F

Photocurrent under visible light irradiation (>400nm, Figures 2-9) was also measured for both samples. RR- TiO_2-F shows a better photoresponse than that of R- TiO_2-F, though the photocurrent itself only experienced a 46% increase, from 36 μA/cm^2 to 53 μA/cm^2.

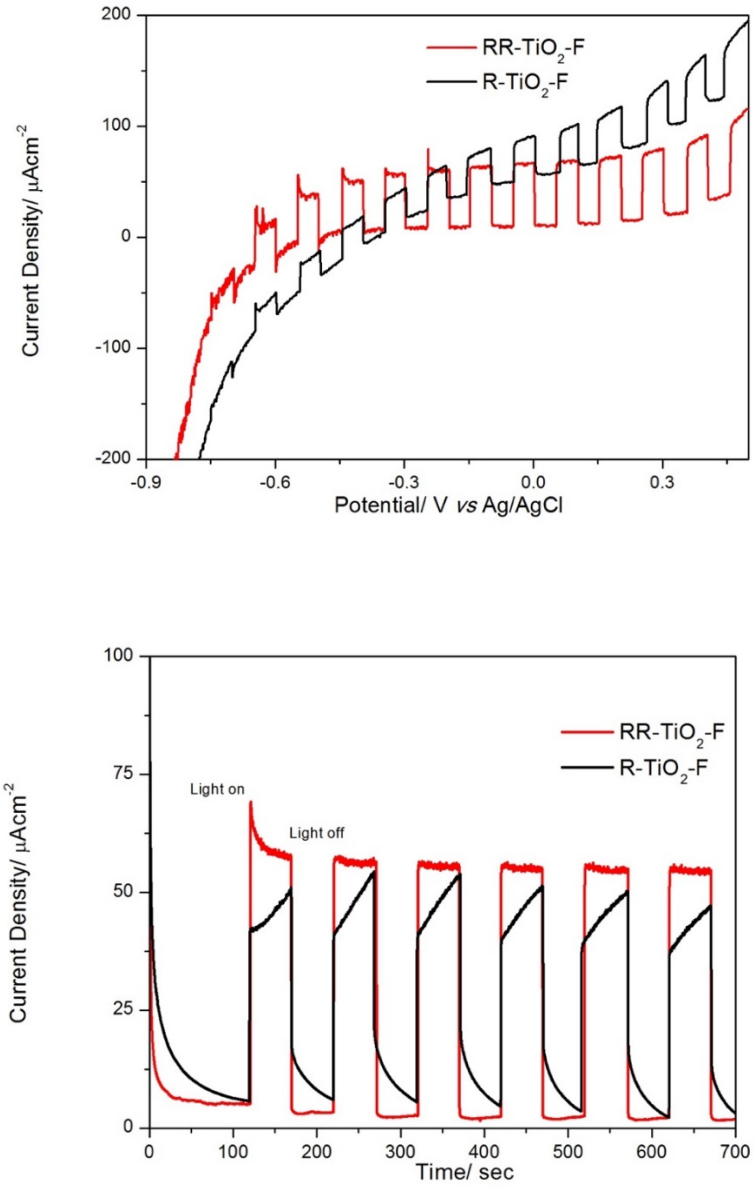

Figure 2- 9. Linear sweep voltammetry of R-TiO_2-F and RR-TiO_2-F with chopped light and 400nm filter (top) transient photocurrent density over time for R-TiO_2-F and RR-TiO_2-F under visible light (bottom)

To verify that this facile N_2H_4 reduction is a general strategy for enhancing the water oxidation performance of TiO_2 photoanode, we also conducted similar experiments for TiO_2 nanowires grown on FTO (denoted as TiO_2-FTO). The photocurrent density obtained from PEC measurement (0.71 mA/cm^2 at 1.0V *vs* RHE) was also comparable with previous reports. While no morphology or phase change was observed after the reduction, photocurrent density underwent a nearly 1-fold increase to 1.32 mA/cm^2 at the same bias (Figure 2-10a). Given the fact that 1.8 mA/cm^2 is thermodynamically maximum achievable photocurrent of rutile under AM 1.5 G illumination by adsorbing all incoming photons with energies above its band gap, N_2H_4 reduced TiO_2-FTO (denoted as R-TiO_2-FTO) utilized 73% available photons and is among the best of TiO_2 photoanode under AM 1.5 G illumination. Even under visible light illumination (>400nm), R-TiO_2-FTO can still keep 18% (0.24 mA/cm^2) of its total current, tripling that of the pristine one (Figure 2-10b).

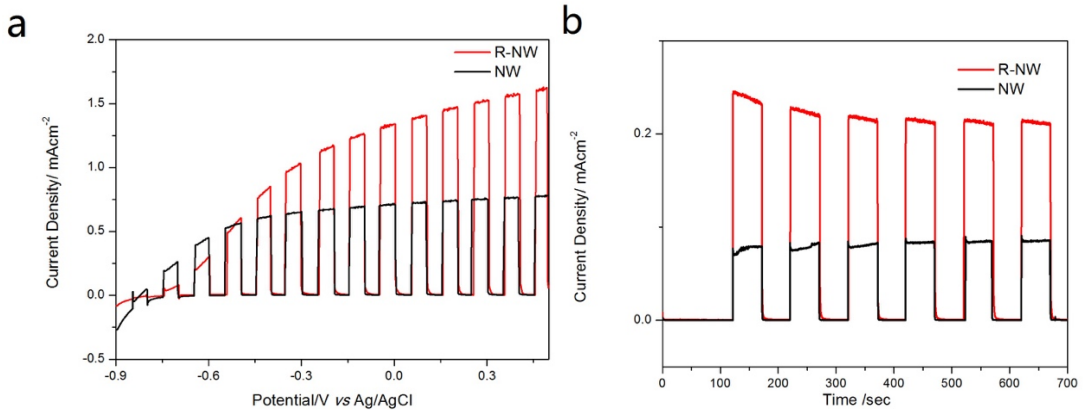

Figure 2- 10. Linear sweep voltammetry with chopped light (a) and transient photocurrent density over time under visible light (b) for TiO_2 nanowires grown on FTO and its reduced form.

2.3.5 Incident Photon-to-Current Efficiency

To better understand their performance, the incident photon-to-current conversion efficiencies (IPCE)[29] were measured at 0.7V versus RHE (Details in SI). IPCE allows the study of materials' PEC performance as a function of incident beam wavelength and excludes the effects of different light sources and filters. For example, the photocurrent for RR-TiO2-F obtained by integrating IPCE multiplied by AM 1.5 G energy flux over the range of 300 – 500 nm is 0.61mA/cm2. The discrepancy between the measurements under AM 1.5G irradiation at the same bias (0.58 mA/cm2) and the integration method might come from the difference between the simulated light and standard AM 1.5G. IPCE is determined by three key factors involved in PEC, as shown in the equation below,

$$\mathrm{IPCE}(\lambda) = \eta_{e^-/h^+}(\lambda) \times \eta_{\mathrm{transport}}(\lambda) \times \eta_{\mathrm{transfer}}(\lambda)$$

where $\boldsymbol{\eta_{e^-/h^+}(\lambda)}$, $\boldsymbol{\eta_{transport}(\lambda)}$ and $\boldsymbol{\eta_{\mathbf{transfer}}(\lambda)}$ represent the efficiencies for photon absorbance, charge transport within the electrode and charge transfer at the electrode/ electrolyte interface, respectively.[30] As shown in the UV-Vis spectrum obtained by their corresponding reflectance spectra (Figure 2-11), R-TiO_2-F and RR- TiO_2-F have comparable light adsorption. The minor difference here can't account for a big difference in the activity.

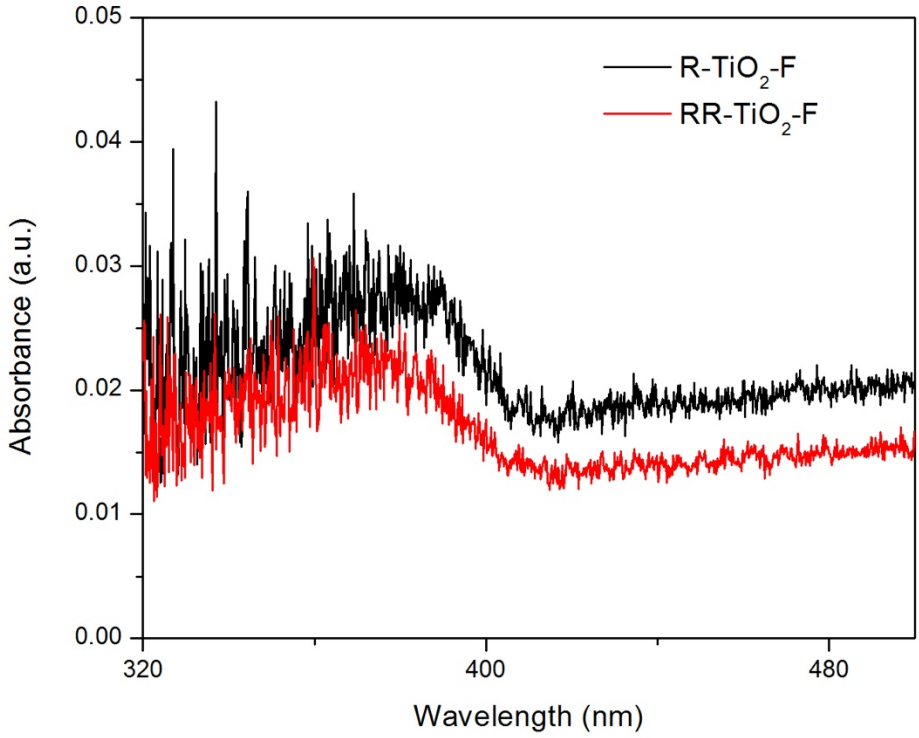

Figure 2- 11. UV-VIS spectra for R-TiO_2-F and RR-TiO_2-F

From Figure 2-12 we note both samples have an adsorption edge around 420nm. RR-TiO_2-F begins to triumph when the wavelength is shorter than 370nm, allowing this portion of light to make a major contribution to the photocurrent enhancement. Given that higher energy photons are mainly adsorbed near the tip of one-dimensional TiO_2 and electrons generated there need to travel a longer distance to reach the current collector, an enhanced electron mobility should be achieved in RR- TiO_2-F to facilitate this charge transport, namely a more efficient $\boldsymbol{\eta_{transport}(\lambda)}$. IPCE measurement of TiO_2 nanowires grown on FTO again confirmed the enhanced photocurrent is due to an elevated utilization of UV portion, especially those with a wavelength shorter than 380 nm.

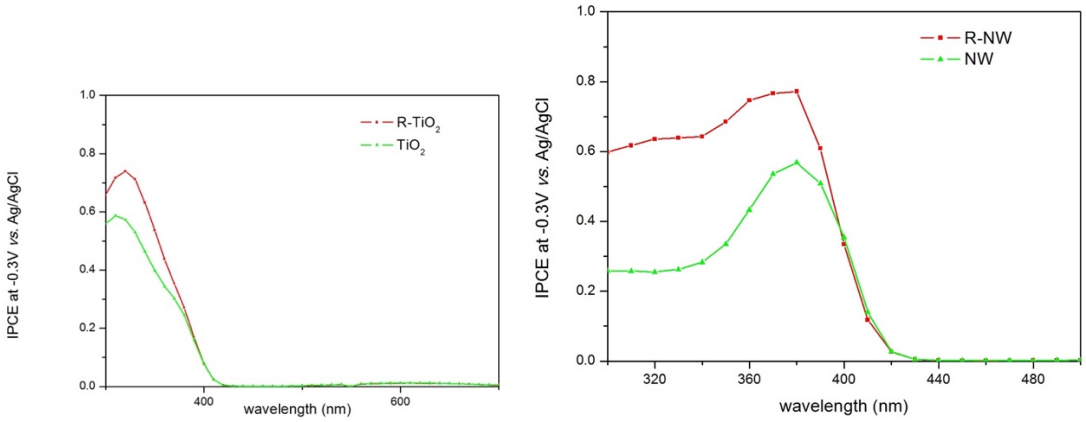

Figure 2- 12. IPCE for TiO_2 grown on Ti film and its reduced product (Left); IPCE for TiO_2 grown on FTO and its reduced product

2.3.6 Impedance Study and Mott-Schottky plot

To validate our postulate that improved electron conductivity contributes to a better performance, we compared electrochemical impedance spectra (EIS) of R- TiO_2-F and RR- TiO_2-F in dark and illumination conditions. The radius of the arcs of Nyquist plots shown in Figure 2-13 is associated directly with the charge-transfer process and a smaller radius is correlated with a more efficient charge transfer. For both samples, a much smaller arc was obtained under illumination, suggesting less charge transfer resistance. Significantly, RR- TiO_2-F showed an arc more compressed than that of R- TiO_2-F both in dark and under irradiation, suggesting a better charge transfer process and thus a more effective separation of photo-generated electron-hole pairs.

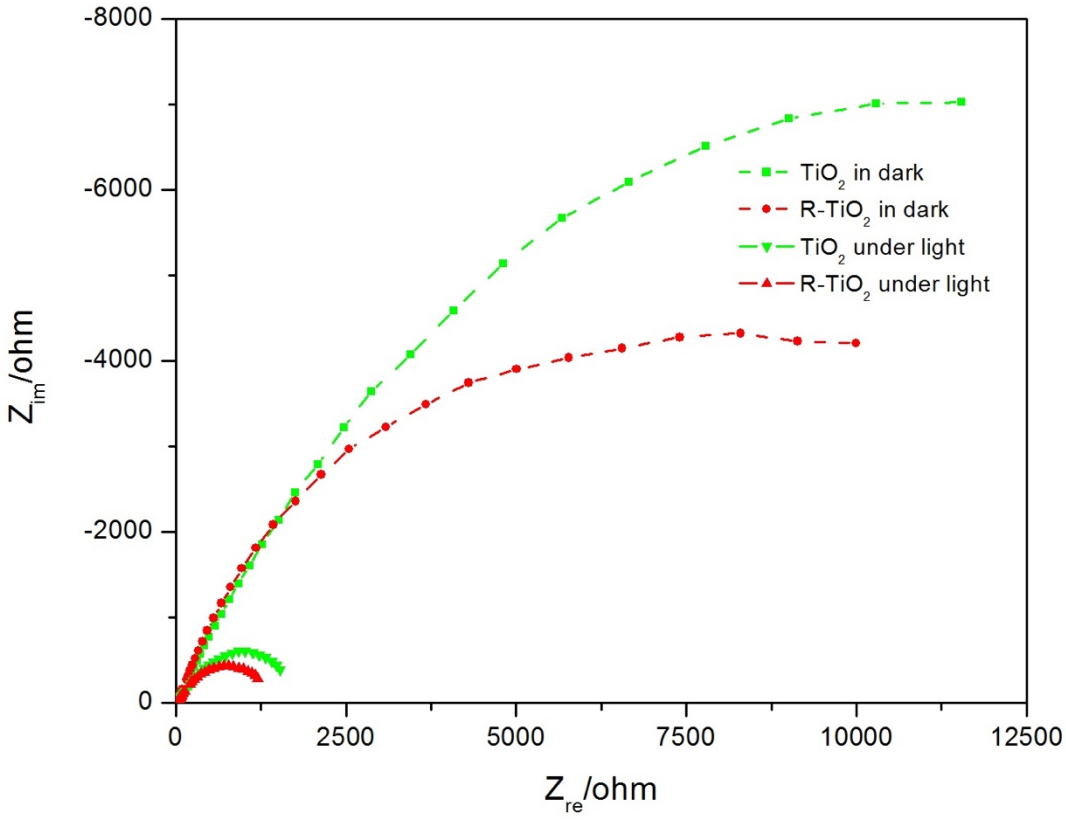

Figure 2- 13. Nyquist plots for R-TiO_2-F and RR-TiO_2-F in dark and under illumination

To gain further insight into the charge transfer process and the impact of N_2H_4 reduction on electronic structures, Mott-Schottky plots were collected at 5kHz in the dark (Figure 2-14). A positive slope in the plot is a direct evidence of n-type semiconductor, as expected from TiO_2 photoanode. Moreover, a substantially smaller slope for RR-TiO_2-F with higher Ti^{3+} concentration was obtained compared to R-TiO_2-F, suggesting an increase of donor density after N_2H_4 reduction. Carrier density of each sample can be calculated from the corresponding slope using following equation

$$N_d = \frac{2/e_0 \epsilon \varepsilon_0}{d(1/C^2)/dV}$$

Here we take ε=170 for rutile TiO_2[31] and the calculated electron densities of R- TiO_2-F and RR- TiO_2-F were 6.9×10^{18} cm-3 and 8.54×10^{19} cm^{-3}, respectively. Though absolute value of donor density calculated from a flat electrode model may not be accurate, a dramatic enhancement of donor density is unambiguously supported via a qualitative comparison of slopes, considering the intact morphology and phase upon reduction. This increase in charge carrier density gives rise to improved electronic conductivity and thus a better electron-hole pair separation and transport ($\eta_{transport}(\lambda)$) within the electrode. Moreover, the upward shift of Fermi level[32] caused by higher donor density could further facilitate the charge transfer kinetics at electrode/electrolyte interface, which is another fundamental factor affecting IPCE besides charge transport within the bulk materials. On the contrary, a depressed donor density would impair the charge separation and thus lower the PEC performance. Upon being heated in air for only 1 hour, R- TiO_2-F lost most of its activity and the photocurrent became lower than 0.1 mA/cm^2. The donor density decreased to 5.7×10^{16} cm^{-3} and an enlarged arc appeared in Nyquist plot, as shown in Figure 2-15. A lack of Ti^{3+} signal in its corresponding powder sample's EPR spectrum is also consistent with its lowered Ti^{3+} level here.

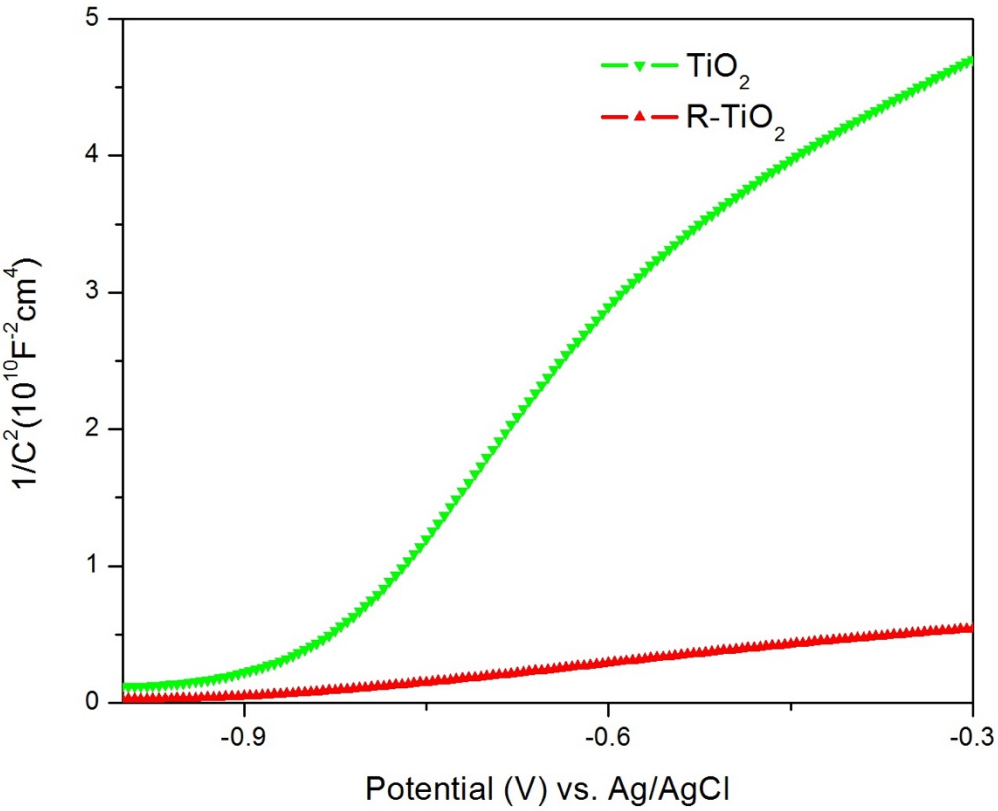

Figure 2- 14. Mott-Schottky plots for R-TiO_2-F and RR-TiO_2-F in dark.

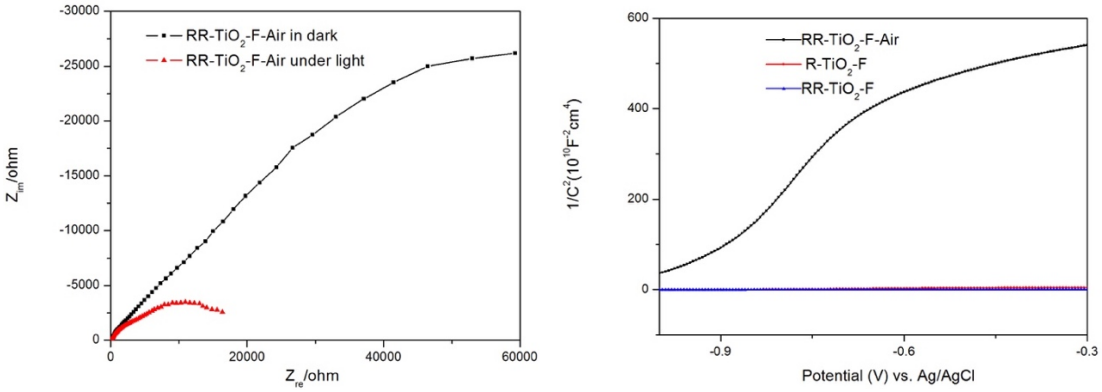

Figure 2- 15. Nyquist plots for RR-TiO_2-F-Air in dark and under illumination (a), Mott-Schottky plots for RR-TiO_2-F-Air, R-TiO_2-F and RR-TiO_2-F in dark (b).

2.4 Conclusion

In summary, we have developed a novel method to grow one-dimensional crystalline rutile TiO_2 directly on flexible Ti metal substrate for the first time. Self-doping by Ti^{3+} is also realized in the same step. We also demonstrate the N_2H_4 reduction as a facile and general method that provides a higher Ti^{3+} self-doping level and greatly improves water oxidation performance for TiO_2 materials.

The boost in photocurrent shown here should result from an enhanced donor density and thus higher electronic conductivity brought by the reduction process, as confirmed by EPR spectra and impedance analysis. The newly developed Ti metal / TiO_2 layout creates new opportunities for device fabrication in various related fields and allows for treatment of TiO_2 even under harsh conditions without damaging the substrate. This simple but effective reduction method also provides a general and promising route for enhancing the properties of a large number of existing semiconductors.

2.5 References

1. N. S. Lewis, Science, 2007, 315, 798-801.

2. a) S. Fu, Y. Liu, Y. Ding, X. Du, F. Song, R. Xiang, B. Ma, Chem. Commun., 2014, 50, 2167-2169; b) J. Gao, J. Miao, P.-Z. Li, W. Y. Teng, L. Yang, Y. Zhao, B. Liu, Q. Zhang, Chem. Commun., 2014, 50, 3786-3788.

3. A. Fujishima, K. Honda, Nature, 1972, 238, 37-38.

4. S. U. M. Khan, M. Al-Shahry, W. B. Ingler, Science, 2002, 297, 2243-2245.

5. X. Chen, S. Shen, L. Guo, S. S. Mao, Chem. Rev., 2010, 110, 6503-6570.

6. a) Y.-C. Pu, G. Wang, K.-D. Chang, Y. Ling, Y.-K. Lin, B. C. Fitzmorris, C.-M. Liu, X. Lu, Y. Tong, J. Z. Zhang, Y.-J. Hsu, Y. Li, Nano. Lett., 2013, 13, 3817-3823; b) L. Fuoco, U. A. Joshi, P. A. Maggard, J. Phys. Chem. C., 2012, 116, 10490-10497; c) Y. Xu, R. Xu, J. Cui, Y. Liu, B. Zhang, Chem. Commun., 2012, 48, 3881-3883.

7. a) Y. Tan, C. Xu, G. Chen, X. Fang, N. Zheng, Q. Xie, Advanced Functional Materials, 2012, 22, 4584-4591; b) Y. Ling, G. Wang, D. A. Wheeler, J. Z. Zhang, Y. Li, Nano. Lett., 2011, 11, 2119-2125; c) H. Tantang, J. Xiao, J. Wei, M. B. E. Chan-Park, L.-J. Li, Q. Zhang, European Journal of Inorganic Chemistry, 2011, 2011, 4182-4186.

8. a) B. Liu, E. S. Aydil, J. Am. Chem. Soc., 2009, 131, 3985-3990; b) X. Feng, K. Shankar, O. K. Varghese, M. Paulose, T. J. Latempa, C. A. Grimes, Nano. Lett. 2008, 8, 3781-3786; c) B. Tan, Y. Wu, J. Phys. Chem. B., 2006, 110, 15932-15938.

9. a) P. Roy, S. Berger, P. Schmuki, Angew. Chem. Int. Ed., 2011, 50, 2904-2939; b) A. Wolcott, W. A. Smith, T. R. Kuykendall, Y. Zhao, J. Z. Zhang, Small, 2009, 5, 104-111; c) Z. Zhang, P. Wang, Energy Environ. Sci., 2012, 5, 6506-6512.

10. I. S. Cho, Z. Chen, A. J. Forman, D. R. Kim, P. M. Rao, T. F. Jaramillo, X. Zheng, Nano. Lett., 2011, 11, 4978-4984.

11. Y. J. Hwang, C. Hahn, B. Liu, P. Yang, ACS Nano, 2012, 6, 5060-5069.

12. a) M. Liu, N. de Leon Snapp, H. Park, Chemical Science, 2011, 2, 80-87; b) J. Shi, Y. Hara, C. Sun, M. A. Anderson, X. Wang, Nano. Lett., 2011, 11, 3413-3419.

13. Y. J. Hwang, A. Boukai, P. Yang, Nano. Lett., 2008, 9, 410-415.

14. J. H. Park, S. Kim, A. J. Bard, Nano. Lett., 2005, 6, 24-28.

15. R. Asahi, T. Morikawa, T. Ohwaki, K. Aoki, Y. Taga, Science, 2001, 293, 269-271.

16. G. Wu, J. Wang, D. F. Thomas, A. Chen, Langmuir, 2008, 24, 3503-3509.

17. I. S. Cho, C. H. Lee, Y. Feng, M. Logar, P. M. Rao, L. Cai, D. R. Kim, R. Sinclair, X. Zheng, Nat. Commun., 2013, 4, 1723.

18. M. Xu, P. Da, H. Wu, D. Zhao, G. Zheng, Nano. Lett., 2012, 12, 1503-1508.

19. F. Zuo, L. Wang, T. Wu, Z. Zhang, D. Borchardt, P. Feng, J. Am. Chem. Soc., 2010, 132, 11856-11857.

20. X. Chen, L. Liu, P. Y. Yu, S. S. Mao, Science, 2011, 331, 746-750.

21. Z. Zhang, M. N. Hedhili, H. Zhu, P. Wang, Phys. Chem. Chem. Phys., 2013, 15, 15637-15644.

22. a) Q. Kang, J. Cao, Y. Zhang, L. Liu, H. Xu, J. Ye, J. Mater. Chem. A., 2013, 1, 5766-5774; b) B. H. Meekins, P. V. Kamat, ACS Nano, 2009, 3, 3437-3446; c) Z. Zheng, B. Huang, X. Meng, J. Wang, S. Wang, Z. Lou, Z. Wang, X. Qin, X. Zhang, Y. Dai, Chem. Commun., 2013, 49, 868-870.

23. G. Wang, H. Wang, Y. Ling, Y. Tang, X. Yang, R. C. Fitzmorris, C. Wang, J. Z. Zhang, Y. Li, Nano. Lett., 2011, 11, 3026-3033.

24. I. S. Cho, M. Logar, C. H. Lee, L. Cai, F. B. Prinz, X. Zheng, Nano. Lett., 2013, 14, 24-31.

25. a) S. Hoang, S. Guo, N. T. Hahn, A. J. Bard, C. B. Mullins, Nano Lett., 2012, 12, 26–32; b) S. Hoang, S. P. Berglund, N. T. Hahn, A. J. Bard, C. B. Mullins, J. Am. Chem. Soc., 2012, 134, 3659-3662.

26. H. Zhang, Y. Wang, P. Liu, Y. Han, X. Yao, J. Zou, H. Cheng, H. Zhao, ACS Appl. Mater. Interfaces, 2011, 3, 2472-2478.

27. F. Zuo, K. Bozhilov, R. J. Dillon, L. Wang, P. Smith, X. Zhao, C. Bardeen, P. Feng, Angew. Chem. Int. Ed., 2012, 51, 6223-6226.

28. D. C. Hurum, A. G. Agrios, K. A. Gray, T. Rajh, M. C. Thurnauer, J. Phys. Chem. B., 2003, 107, 4545-4549.

29. T. Bak, J. Nowotny, M. Rekas, C. C. Sorrell, Int. J. Hydrogen Energy, 2002, 27, 991-1022.

30. Z. Chen, T. F. Jaramillo, T. G. Deutsch, A. Kleiman-Shwarsctein, A. J. Forman, N. Gaillard, R. Garland, K. Takanabe, C. Heske, M. Sunkara, E. W. McFarland, K. Domen, E. L. Miller, J. A. Turner, H. N. Dinh, J. Mater. Res., 2010, 25, 3-16.

31. R. A. Parker, Phys. Rev., 1961, 124, 1719-1722.

32. D. C. Cronemeyer, Phys. Rev., 1959, 113, 1222-1226.

Chapter 3
Anion stripping as a general method to create cationic metal organic frameworks with mobile anions

3.1 Introduction

Metal organic frameworks (MOFs) are porous materials assembled from metal ions or clusters and organic ligands and have shown potential applications in fields such as gas storage and adsorption,[1] catalysis,[2] drug delivery[3] , electrochemistry and photoelectrochemistry.[4] Recent reports have also demonstrated high proton conductivities in MOFs.[5] Water-mediated proton-conducting MOFs operating at a low temperature and anhydrous proton-conducting MOFs working at an intermediate temperature[6] have been well investigated. The design flexibility and framework stability have made MOFs a versatile platform for different types of ion conducting materials. The crystalline nature of MOF materials further allows precise determination of their structures,[7] providing an opportunity to probe the conduction mechanism, which is vital to the rational design and development of new generations of ion conducting materials.

Fuel cells are among a number of viable options to address today's energy and environmental concerns.[8] Ion exchange membranes are a crucial component of fuel cells, acting as a barrier between the fuel and the oxidizing agent while transporting charges from one electrode to another within the cell. Although current state-of-art fuel cells employ Nafion-family proton conductors,[9] anion exchange membrane fuel cells are now attracting growing interest due to their potential advantages,[10] especially their favorable

oxygen reduction kinetics, which would allow for less platinum loading on the electrodes or even non-precious metal catalysts during the electrochemistry process. While significant efforts have been put into developing metal organic frameworks for proton exchange membrane fuel cells, few studies have been reported on anion-conducting MOFs that could be utilized in anion exchange membrane fuel cells.[11]

Anion conductivity can be potentially achieved with the same strategy employed in the synthesis of cationic frameworks.[12] However, unless there are special factors at play, the direct synthesis of stable and porous MOFs predominantly favors neutral frameworks. Given the fact that a large pool of neutral frameworks is available, post-synthetic methods[13] that allow the conversion of neutral frameworks into cationic ones with mobile anions are highly desirable.

Here, we demonstrate a method (termed anion stripping, Figure 4-2) that can be employed to effectively convert neutral frameworks into cationic ones. By taking advantage of the stronger affinity of F^- to Al^{3+} than to Cr^{3+} or Fe^{3+}, this method uses Al^{3+} to strip Cr^{3+}-bonded F^- ions away from Cr^{3+} sites and replaces charge-balancing framework-attached F^- anions with mobile Cl^- and OH^- anions.

3.2 Experimental Section

3.2.1 Reactants and General Methods

All reagents and solvents employed in these studies were commercially available and used as supplied without further purification. UV-VIS adsorption spectra were recorded on a SHIMADZU UV-3150 UV-VIS Scanning Spectrophotometer. Powder X-ray diffraction data were collected using a Bruker D8 Advance powder diffractometer operating at 40 kV, 40mA with Cu Kα (λ =1.5418 Å) radiation (2θ range, 2.5-20°; step, 0.02°; scan speed, 10 s/step). The morphology and semi-quantitative elemental analyses of different samples were characterized by using a Philips FEI XL30 field emission scanning electron microscope (FESEM) equipped with PGT-IMIX PTS energy dispersive spectroscopy (EDS) detector. Data acquisition was performed with an accelerating voltage of 20 kV and 60 s accumulation time.

3.2.2 Synthesis of MIL-100 and MIL-101

MIL-100-Cr-F was prepared by hydrothermal reactions following the procedures reported by Ferey et al.[19] To 100 mg of chromium (VI) oxide CrO_3 were added 210mg of trimesic acid, 0.2 mL of a 5M HF aqueous solution, and 4.8 mL of deionized water (denoted as DI water), and the mixture was stirred for a few minutes in a 20-mL Teflon-lined stainless steel autoclave at room temperature. This vessel was then sealed and heated at 493K for 4 days. The resulting green solid was washed with deionized water and

acetone and dried at room temperature under ambient atmosphere. The as-prepared material was degassed under vacuum at 150^{o}C overnight before further treatment.

MIL-100-Fe-F was prepared by hydrothermal reactions following the procedures reported by Ferey et al.[20] A reaction mixture of molar composition 1.0 Fe: 0.66 trimesic acid: 2.0 HF: 1.2 HNO_3: 280 H_2O was held at 150^{o}C in a Teflon-lined autoclave for 12h. The light-orange solid product was recovered by filtration and washed with deionized water, followed by treatment in hot DI water (80^{o}C) and hot ethanol (60^{o}C) sequentially to remove residual trimesic acid. The as-prepared material was degassed under vacuum at 150^{o}C overnight before further treatment. MIL-101-Cr-F was prepared by hydrothermal reactions following the procedures reported by Ferey et al.[3] A typical synthesis involves a solution containing 400 mg chromium(III) nitrate $Cr(NO_3)_3 .9H_2O$, 1 mmol of HF acid, 164 mg terephthalic acid H_2BDC in 4.8 ml H_2O; the mixture is introduced in an autoclave which is held at 220°C for 8h. After natural cooling, the mixture was filtered first. Then, hot ethanol and NH_4F solution were used sequentially to remove the excess terephthalic acid. The as-prepared solids were degassed under vacuum at 200^{o}C overnight before further treatment.

3.2.3 Anion sripping of synthesized MIL-100 and MIL-101

To 30 mg MIL-100-Cr in the 20mL vial were added 0mL, 1mL, 3mL, 5mL 0.1M $AlCl_3$ solution respectively. Additional DI H_2O was added into the vial to maintain 15mL liquid in the vial. The vials were moved into the 90^{o}C oven and kept for 18h before taken out.

The solids were recovered by filtration and washed with deionized H_2O several times. The isolated solids were labeled as MIL-100-Cr-Cl-0, MIL-100-Cr-Cl-1, MIL-100-Cr-Cl-3, and MIL-100-Cr-Cl-5, respectively. Unless stated otherwise, MIL-100-Cr-Cl refers to MIL-100-Cr-Cl-5 in other parts of this article.

The same procedure used for modifying MIL-100-Cr-Cl was employed for MIL-100-Fe-Cl. The isolated solids were labeled as MIL-100-Fe-Cl-0, MIL-100-Fe-Cl-1, MIL-100-Fe-Cl-3, and MIL-100-Fe-Cl-5, respectively. Unless stated otherwise, MIL-100-Fe-Cl refers to MIL-100-Fe-Cl-5 in other parts of this article.

To 15 mg MIL-101-Cr in the 20mL vial were added 15 mL 0.03 M $AlCl_3$ solution. The vial was moved into the 90^{o}C oven and kept for 18h before taken out. The solids are recovered by filtration and washed with deionized H_2O several times. The isolated solids were labeled as MIL-101- Cr-Cl

3.2.4 Ion Exchange and Precipitation Experiment

A 100 mL sodium hydroxide solution with pH about 12 was prepared first. 100mg MIL-100-Cr-Cl was added into the solution and soaked in the solution under room temperature for one day before being recovered by filtration and washed with deionized H_2O. The as-obtained sample was labeled as MIL-100-Cr-OH.

MIL-100-Cr-Cl powders were soaked in about 10 mL DI water for 12 hours, some upper clear liquid was taken out followed by the addition of 5mM $AgNO_3$ solution, and no apparent change happened in the solution. About 800 mg KNO_3 was added to the

remaining solution and MIL-100-Cr-Cl was kept in the solution for 12 hours. Some amount of upper clear liquid was taken out followed by the addition of 5mM $AgNO_3$ solution, and white participate was formed immediately with the addition of $AgNO_3$ solution.

3.2.5 ^{1}H Solid-state nuclear magnetic resonance (ssNMR) measurements

Magic-angle-spinning (MAS) ssNMR experiments were performed at 14.1 T (^{1}H frequency 600.01 MHz) on a Bruker AVANCE spectrometer equipped with a triple-resonance 1.3 mm Biosolids (^{1}H/^{13}C/^{15}N) MAS probe, spinning at a MAS rate of 50 kHz. 1D spectra were generated by Fourier transformation of a time-domain FID in response to a 3 μs excitation pulse, with 512 complex time-domain data points digitized with a dwell of 10 μs (spectral width 100 kHz, total acquisition time 5.12 ms). 32 transients were averaged with a recycle delay of 0.1 s. Longer recycle delays were found to increase the intensity of the broad baseline component, but did not lead to increased intensity of the major components. Dehydrated solids are obtained by dry in the vacuum oven overnight.

2D spectra (Figure S9) were acquired using a standard NOESY/Exchange Spectroscopy (EXSY) pulse sequence.[21] In the indirect dimension, 256 complex points with a dwell of 20 μs (spectral width 50 kHz, total acquisition time 5.12 ms) were acquired, while in the direct dimension, 512 complex points with a dwell of 10 μs were acquired (spectral width 100 kHz, total acquisition time 5.12 ms). Three 2D EXSY spectra were acquired with the

following timings: A. recycle delay set to 0.03 s, mixing time to 0 s; B. recycle delay set to 1 s, mixing time to 0 s; and C. recycle delay set to 1 s, mixing time to 0.5 s. The first experiment selects for fast relaxing components, the second for all components, and the third for long relaxing components. The corresponding spectra are shown in Figure 4-11. Note that in the first (A), only the very quickly relaxing Cr-bound peaks are observed. In the second (B), there is a sharp ridge that is both narrower (longer T_2) and more slowly relaxing (longer T_1). This component can be selected by increasing the mixing time in the EXSY sequence to 0.5 s (C), during which the paramagnetically-bound species relax. We tentatively assign this 'ridge' of more slowly relaxing hydrogens to non-specifically adsorbed water within the porous framework. These water molecules experience a significant distribution of paramagnetic shifts (from -15 to +15 ppm), but reduced relaxation enhancement.

3.2.6 Ion Exchange Experiment with Organic Dyes

Ion-exchange experiment was performed by soaking 10 mg powders into 15 mL aqueous solution of different dyes. The solution and powders were kept still in the vial overnight under room temperature. UV-Vis absorbance measurements were performed for the upper clear solution. The absorbance maximum of original dye solution before exchange was normalized and the remaining amount of dyes in the solution was calculated by the ratio of the absorbance maximum after exchange to that of the original one.

In a typical experiment, 12 mg as-prepared MIL-100-Cr-Cl-5 was weighted out to a 20 mL vial, and 10 mL dye aqueous solution containing 1 mg orange G was added to the vial. After an overnight exchange, the upper clear solution was taken out for UV-Vis absorbance measurement (solution would be diluted with deionized water if the peak signal exceeded the detection limit of the instrument).

For cation exchange experiment, methylene blue was used instead of orange G.

3.2.7 Conductivity Measurement

The compacted powder samples for conductivity measurements (pellets with 13 mm in diameter, around 0.5 mm in thickness) were prepared by pressing the powder in a 13 mm die at 45 MPa for 2 minutes. The pellet was sandwiched between two blocking stainless-steel electrodes and fixed with a clamp for measurements. AC impedance spectroscopy measurements were performed using a Solartron 1260 impedance/gain-phase analyzer connected to a Solartron 1287 electrochemistry interface. ZPlot 2.6b was used as the control software and ZView 2.6b was used as the analysis software. A typical measurement was made over a frequency range between 1 MHz to 1 Hz and a 50 mV (peak voltage) was applied as AC signals. Ten measurements were made in every frequency decade with 2s integration time at each frequency. Variable impedance spectra were collected over different humidity and temperature obtained by saturated salt solutions and the water bath. Ionic conductivity σ(S/cm) was calculated using the formula below:

$$\sigma = L/AR$$

where *L* is the pellet thickness while *A* is the pellet area in contact with the stainless- steel electrodes. *R* is the complex impedance obtained from Nyquist plot.

3.3 Results and Discussion

3.3.1 Reaction Mechanism

The post-synthetic modification of the original MIL-100[14] (denoted as MIL-100-Cr-F and MIL-100-Fe-F, Figure 4-1) was performed in two steps, through exchange of F^- with Cl^- and OH^- sequentially.

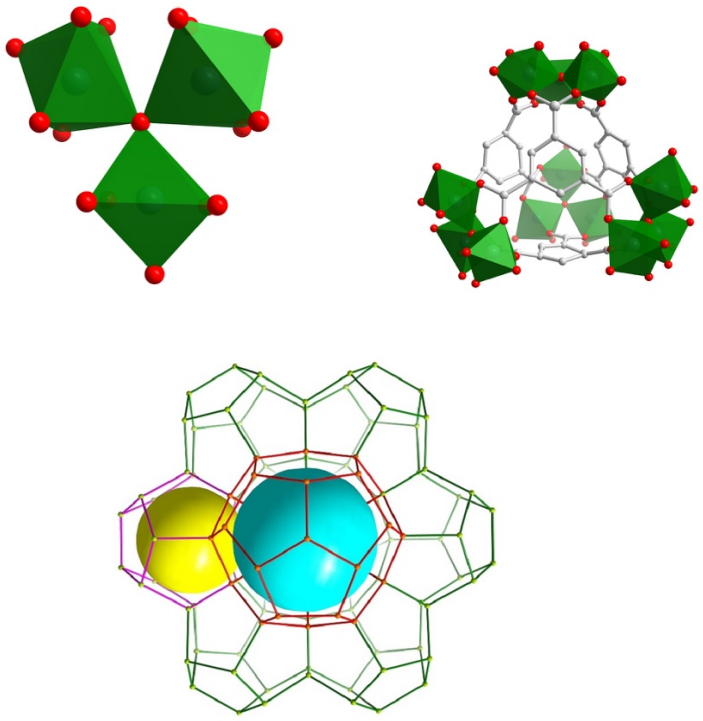

Figure 3- 1. Structure of MIL-100 trimer (top left), supertetrahedra (top right) and MTN zeolitic topology (bottom).

The removal of strongly bonded F^- on Cr^{3+} or Fe^{3+} in MIL-100-Cr-F or MIL-100-Fe-F was achieved by soaking their respective pristine powders into $AlCl_3$ solutions. For charge balance, chloride ions enter the pore to replace F^- (Figure 4-2). Following the modification, the solid was collected by filtration and washed several times to remove extra ions that might be adsorbed on the solid surface. Considering that Hydroxide ion conductors are a desirable target in fuel cells, MIL-100-Cr-Cl powders were further soaked in sodium hydroxide solution to exchange Cl^- with OH^-. While the conversion of MIL-100-Cr-Cl into MIL-100-Cr-OH was successful, the conversion of MIL-100-Fe-Cl failed since it appeared unstable under the alkaline conditions used here.

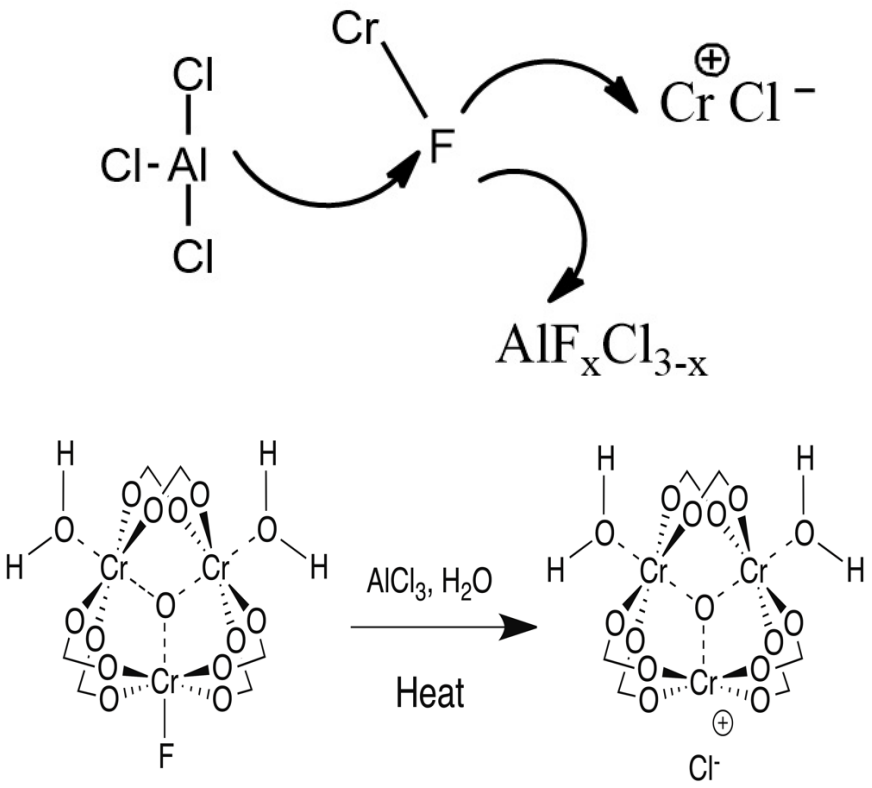

Figure 3- 2. An illustration of the anion stripping process.

3.3.2 Structural Analysis

Crystallinity and porosity of samples after the modifications were monitored by PXRD and nitrogen adsorption measurements. As indicated by the PXRD results in Figure 4-3a, modified samples (MIL-100-Cr-Cl and MIL-100-Cr-OH) remained highly crystalline, even though some peaks were broadened, likely due to the reduced particle size during the modification steps. As for MIL-100-Fe-Cl, no any loss of crystallinity was detected by the PXRD analysis (Figure 4-3b).

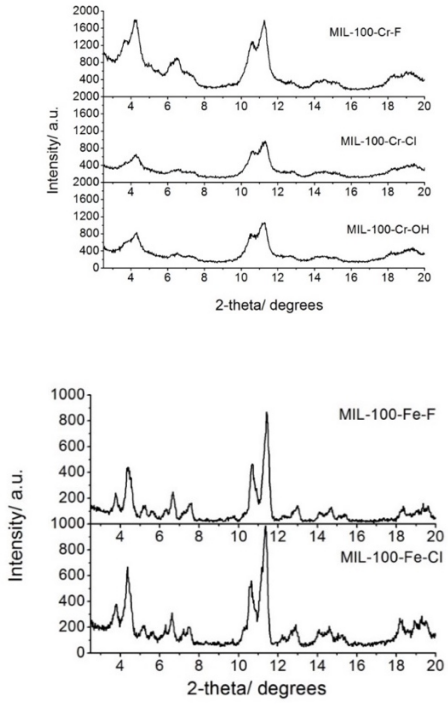

Figure 3- 3. PXRD patterns of MIL-100-Cr-F (a), MIL-100-Fe-F (b) and their modified forms.

Furthermore, the porosity of MIL-100-Cr-Cl and MIL-100-Fe-Cl remained intact as shown by the nitrogen adsorption data (Figure 4-4).

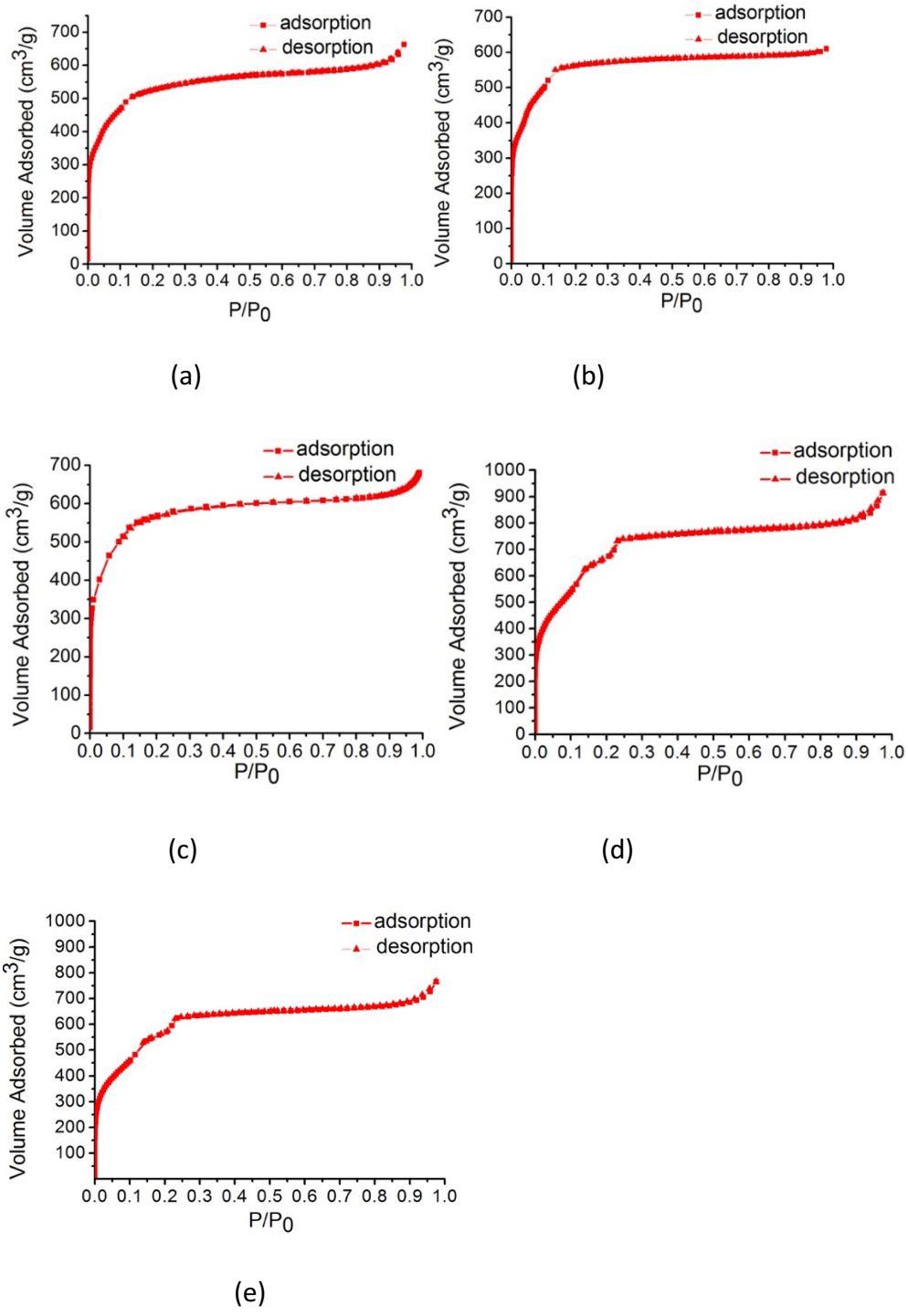

Figure 3- 4. Adsorption and desorption isotherms of nitrogen at 77 K MIL-100-Cr-F (a), MIL-100-Cr-Cl (b), MIL-100-Fe (c), MIL-100-Fe-Cl (d), MIL-101-Cr-F (e), and MIL-101-Cr-Cl (f).

MIL-101-Cr-Cl[15] also stayed intact after the modification (Figure 4-5)

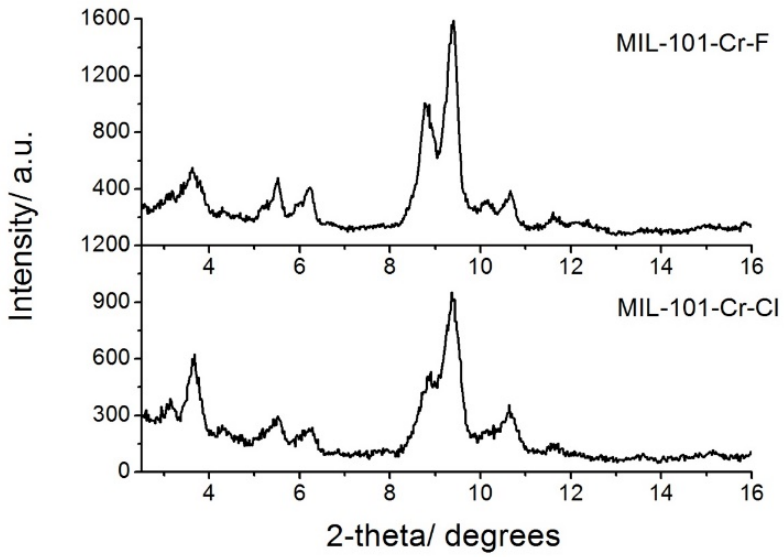

Figure 3- 5. PXRD patterns of MIL-101-Cr-F and MIL-101-Cr-Cl

3.3.3 Morphology and Composition Analysis

The successful replacement of F^- by Cl^- ions in both MIL-100-Cr and MIL-100-Fe was confirmed by the EDX analysis. The SEM images (Figure 4-6) show the as-prepared powder samples as small octahedra.

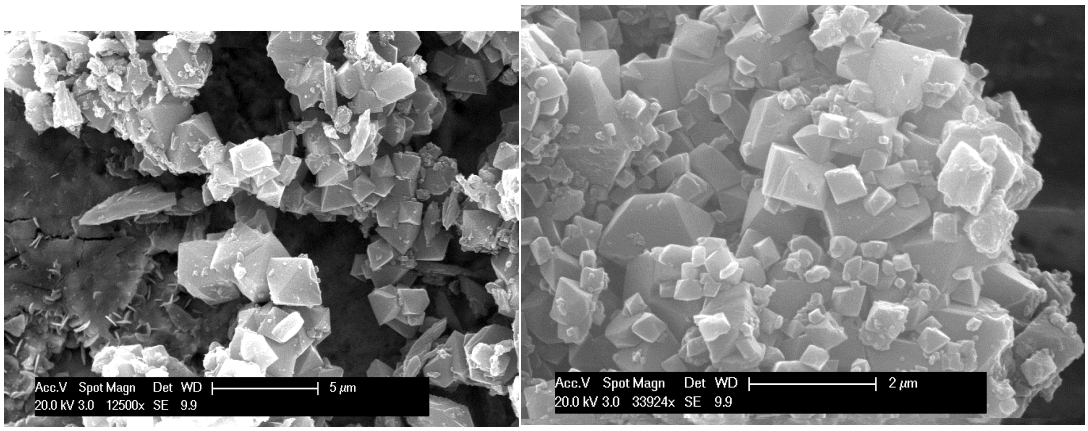

(a) (b)

Figure 3- 6. SEM image for as prepared and MIL-100-Cr-F (a) and MIL-100-Fe-F (b)

Both as-synthesized MIL-100-Cr-F and MIL-100-Fe-F have apparent F peaks from the EDX spectra (Figure 4-7), in accordance with the fact that F is bonded to Cr^{3+} or Fe^{3+} in the metal trimmers. However, no F peaks were detected for MIL-100-Cr-Cl or MIL-100-Fe-Cl while new chloride peaks appeared (Figure 4-8), proving the successful replacement of F by Cl.

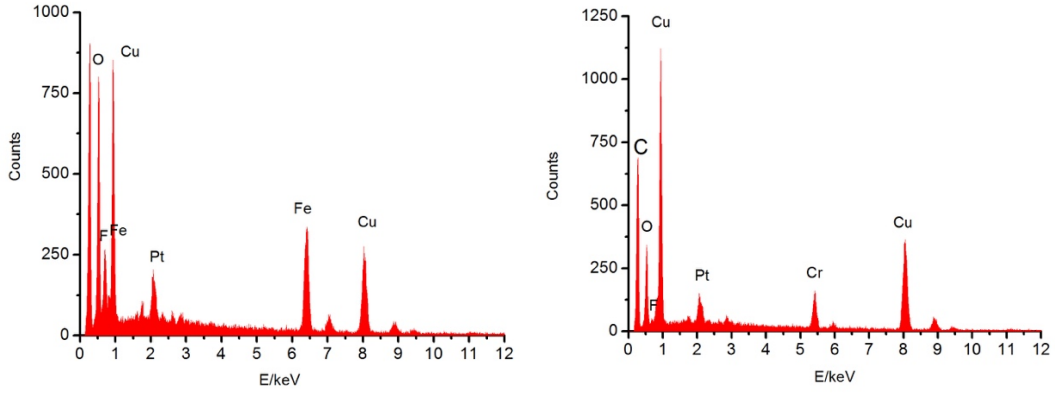

Figure 3- 7. EDX spectra of MIL-100-Cr-F (Left) and MIL-100-Fe-F (Right)

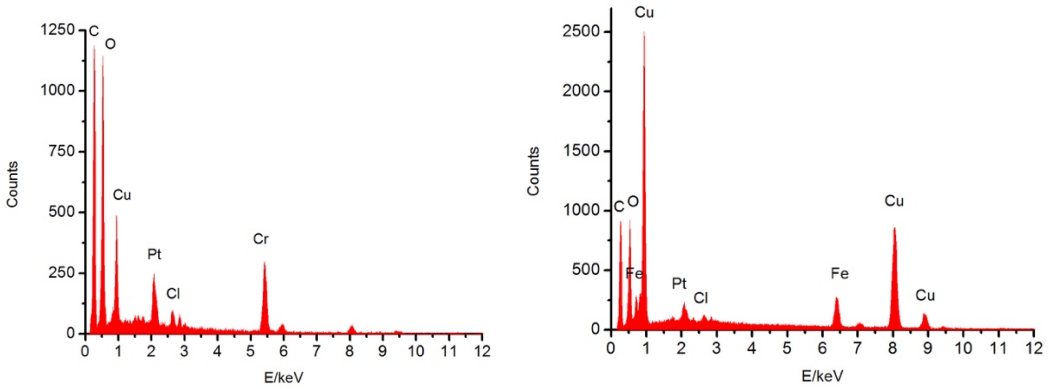

Figure 3- 8.EDX spectra of MIL-100-Cr-Cl (a) and MIL-100-Fe-Cl (b)

The evidence for the successful replacement of F^- by Cl^- and for the mobility of Cl^- ions in the modified framework was further shown by the precipitation experiment with $AgNO_3$ (See Experimental Section). By soaking MIL-100-Cr-Cl in the $AgNO_3$ solution, no precipitation was observed, ruling out the possible surface-adsorbed Cl^- residues on the powder. Next, the Cl^- was displaced out of the pores into the solution by anion exchange with the concentrated $NaNO_3$ solution. As a result, the NO_3^- exchanged solution readily underwent the precipitation reaction with Ag^+ ions in the solution (Figure 4-9). Such experiments not only confirmed the presence of Cl^- ions in the pores, but also but also their mobility.

Figure 3- 9. Precipitation reaction for MIL-100-Cr-Cl

The exchange of OH^- for Cl^- in MIL-100-Cr-OH could first be inferred from the decreased Cl/Cr ratio (based on the EDX data) following the exchange of Cl^- with OH^- Because a fixed amount of anions are required to balance the charge, the decreased Cl/Cr ratio following the exchange with OH^- suggests that some Cl^- anions had been replaced with OH^- anions.

	MIL-100-Cr-Cl	MIL-100-Cr-OH
Cr/Cl	9.8	25.1

Further support for the inclusion of the OH^- anion into the framework comes from solid-state NMR spectroscopy. Figure 4-10 shows ^1H spectra for MIL-100-Cr-F and MIL-

100-Cr-OH under conditions of low and ambient exposure to moisture. Inclusion of OH^- correlates with an additional peak at -0.2 ppm, while increasing hydration leads to increased downfield peak intensity at 6.1 ppm.

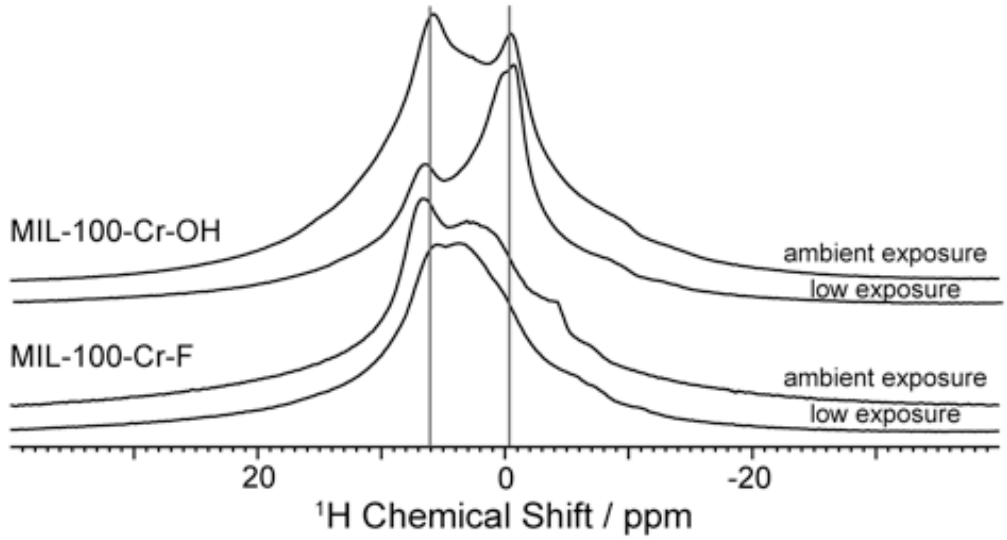

Figure 3- 10. ^{1}H spectra for MIL-100-Cr-F and MIL-100-Cr-OH obtained from solid-state NMR

We therefore assign these peaks to the hydrogens of hydroxide and water, respectively. Both peaks are found to relax quickly (Figure 4-11), consistent with direct association with the paramagnetic Cr sites. A third spectral component, centered at ~3.7 ppm, is assigned to hydrogens on the aromatic ligands. These assignments are consistent with similar observations in other paramagnetic MOF systems.[16] Two-dimensional chemical-shift – chemical-shift correlation experiments allow better resolution of the three sites, as shown in the Supporting Information. Also evident in the 2D spectrum is a

'ridge' of more slowly relaxing hydrogens that we tentatively assign to non-specifically adsorbed water within the porous framework.

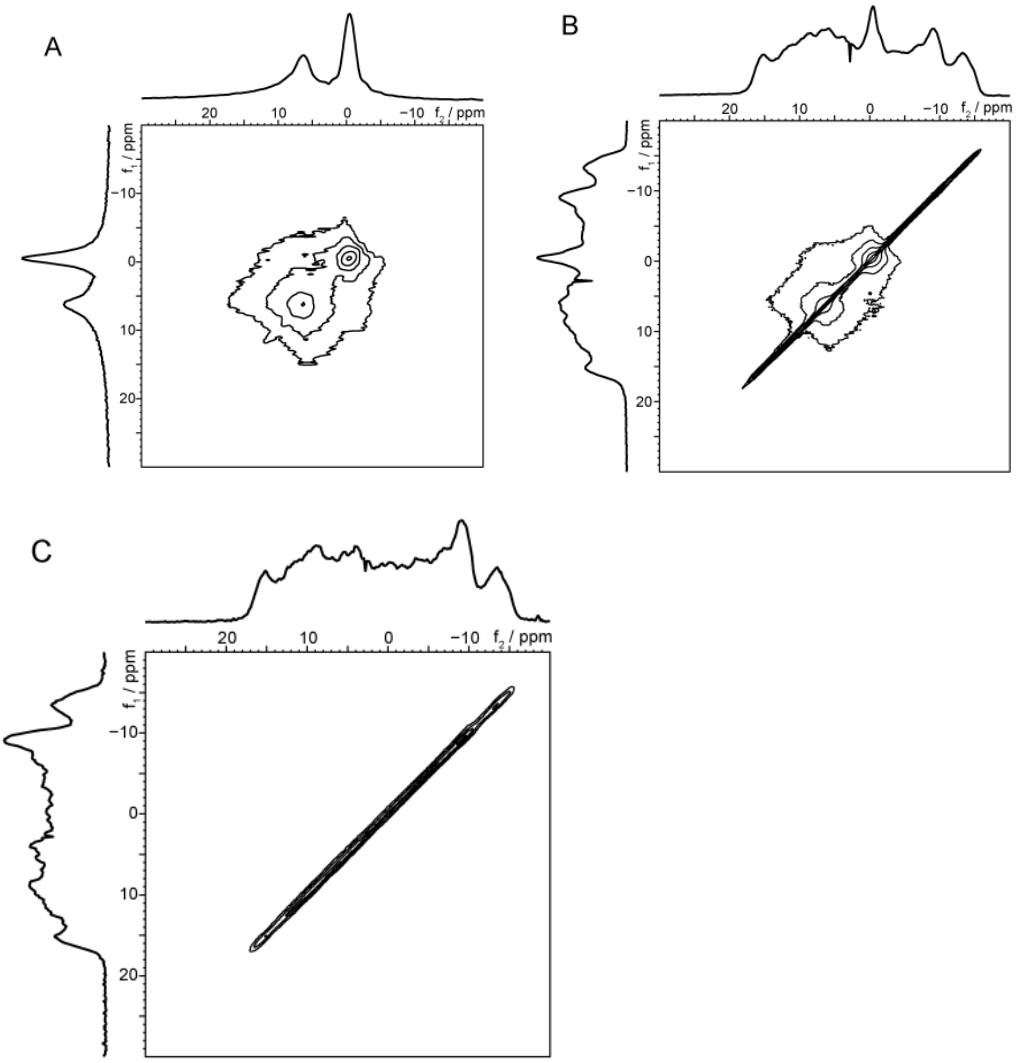

Figure 3- 11. Two-dimensional chemical-shift – chemical-shift correlation spectroscopy of MIL-100-Cr-OH under conditions of ambient exposure to moisture. A. Fast relaxing components directly bonded to Cr are selected by a short recycle (relaxation) delay and 0 s exchange mixing time. B. Fast and slow relaxing components selected using a recycle delay of 1 s and 0 s exchange mixing time. C. Slow relaxing components (tentatively assigned to adsorbed water in the framework channels) selected by a recycle delay of 1 s and a mixing time of 0.5 s.

3.3.4 Ion Exchange with Organic Dyes

The mobility of Cl^- anions was further confirmed by ion exchange[17] with anionic organic dye molecules (See Experimental Section). Figure 4-12 shows the UV-VIS spectra for a series of Orange G (OG) solutions that were treated by the original MIL-100-Cr-F and modified MIL-100-Cr-Cl (labeled as MIL-100-Cr-Cl-0, 1, 3, and 5 respectively, corresponding to different amount of $AlCl_3$ used for anion stripping, details in supporting information). The decreasing absorbance of OG solutions (following exchange with Cl^-) was the direct evidence of increased anion-exchange abilities of modified MIL-100-Cr-Cl, due to the high mobility of Cl^-. For the original unmodified MIL-100-Cr-F, the only way to trap OG is physical adsorption of both organic anions (OG^{2-}) and its counter cations (i.e., Na^+). But for modified MIL-100-Cr-Cl with mobile Cl^- ions, the exchange of Cl^- anions with OG^{2-} anions could take place, leading to an improved uptake of OG^{2-} anions. With more mobile Cl^- ions introduced into the framework, more OG^{2-} can be exchanged into the pores, as evidenced in Figure 4-12.

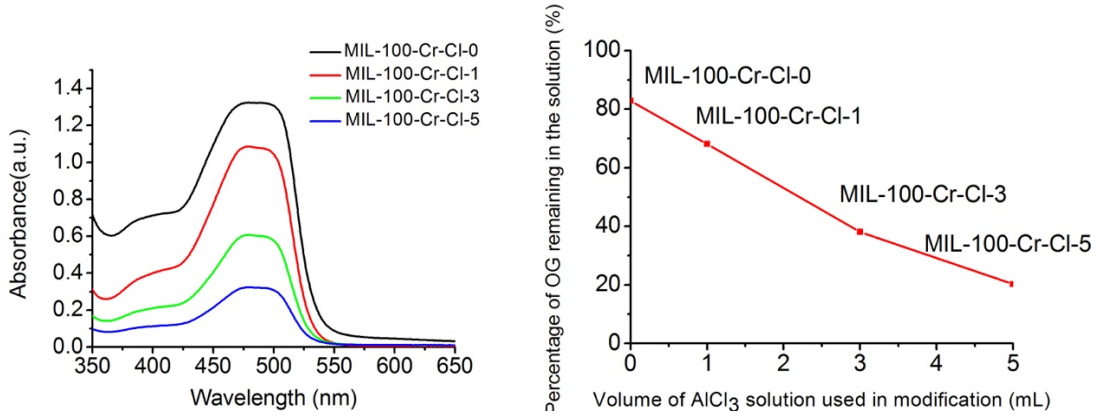

Figure 3- 12. UV-VIS absorbance (Left) and remaining percentage of Orange G (Right) treated by MIL-100-Cr-F and its modified forms

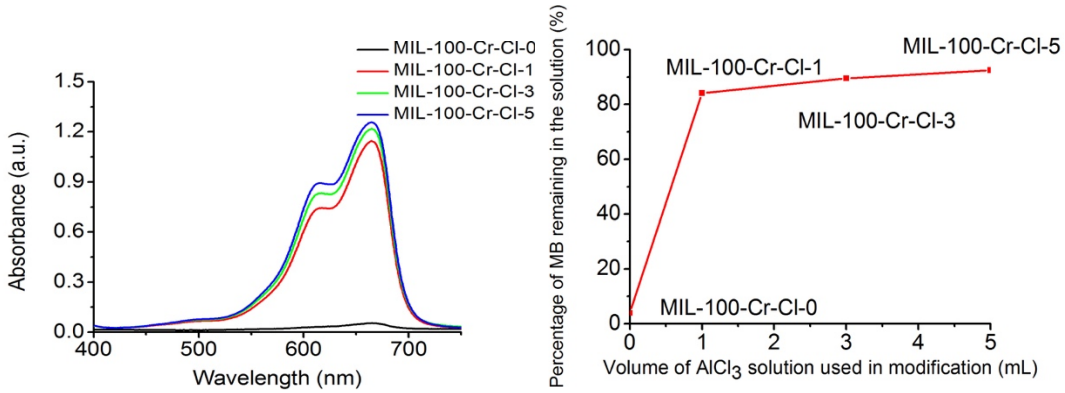

Figure 3- 13. UV-VIS absorbance (Left) and remaining percentage of Methylene Blue (Right) treated by MIL-100-Cr-F and its modified forms

In addition to significantly improved anion exchange property, the conversion of neutral MIL-100-Cr-F into cationic MIL-100-Cr-Cl had a dramatic effect on their cation exchange properties.[18] Positively charged methylene blue (MB) was chosen here. The MB solution turned almost clear when unmodified neutral MIL-100-Cr-F was soaked in them for one day, showing a good adsorption ability by neutral MIL-100-Cr for MB. The higher

adsorption ability of neutral MILs for MB^{+} than for OG^{2-} is likely due to relatively smaller size of MB cation than OG anion (Figure 4-14).

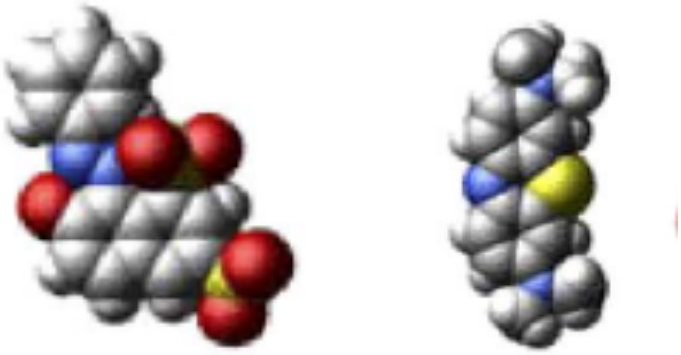

Dye	MLB	OG
x (Å)	4	5.44
y (Å)	7.93	10.14
z (Å)	16.34	15.64

Figure 3- 14. 3D drawing of dye molecules, Orange G (Top Left) and Methylene Blue (Top Right). The actual sizes of two dye molecules

However, a dramatic decrease in the adsorption ability for MB cations took place even after neutral MIL-100-Cr-F was treated with a small amount of $AlCl_3$ (Figure 4-13). This result can be explained by the fact that the cationic framework MIL-100-Cr-Cl obtained from our modification repels cationic dyes, while neutral unmodified MIL-100-Cr-F is more receptive to cationic dyes. Similar results were obtained for both MIL-100-Fe (Figure 15&16) and MIL-101-Cr (Figure 17)

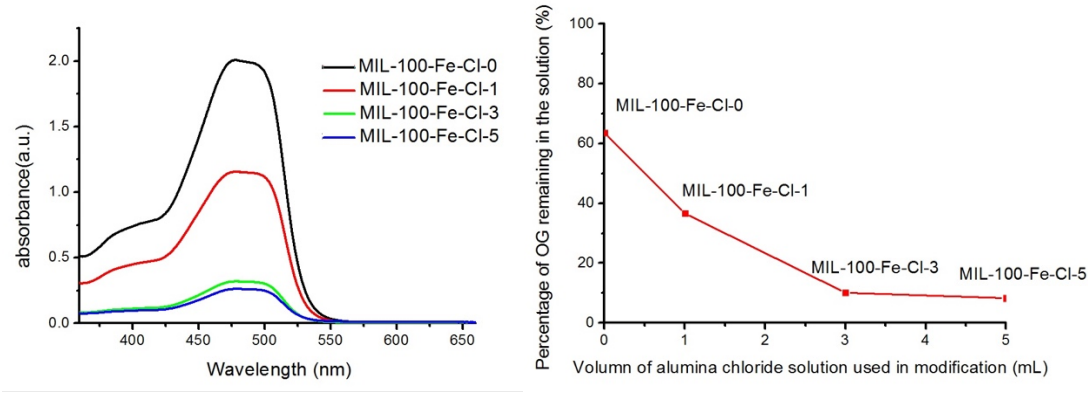

Figure 3- 15. UV-VIS absorbance (Left) and remaining percentage of Orange G (Right) treated by MIL-100-Fe-F and its modified forms

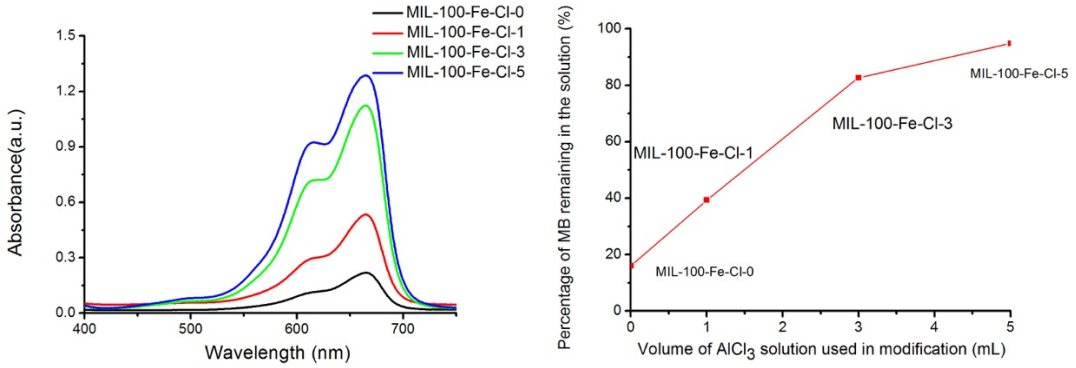

Figure 3- 16. UV-VIS absorbance (Left) and remaining percentage of Methylene Blue (Right) treated by MIL-100-Cr-F and its modified forms

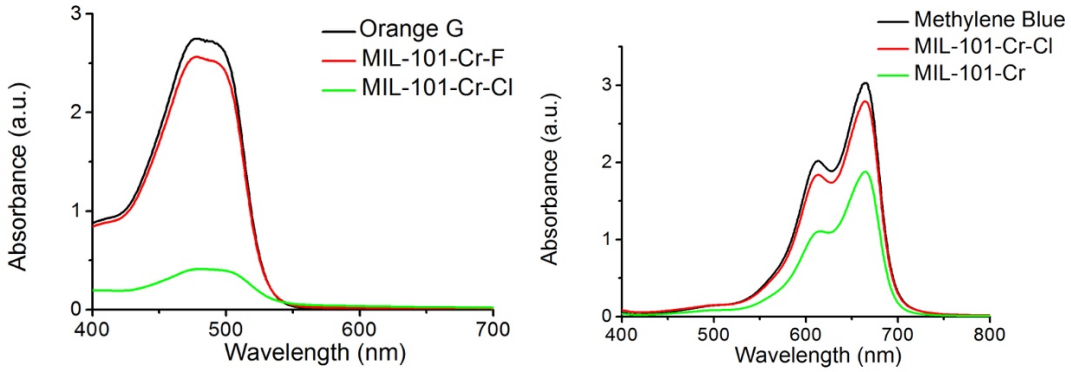

Figure 3- 17 UV-VIS absorbance of Orange G (Left) and Methylene Blue (Right) treated by MIL-101-Cr-F and MIL-101-Cr-Cl

3.3.4 Ionic Conductivity and Activation Energy

The conversion of neutral MIL-100-Cr-F (as well as the Fe form) into MIL-100-Cr-Cl with mobile chloride led to a dramatic enhancement in their ion-conduction properties. To characterize the anion conductivity of MIL-100-Cr-Cl, AC impedance measurement was performed on pellet samples (See supporting information). A representative Nyquist plot is shown in Figure 4-18, which consists of a semicircle at high frequency region and a spike tail at low frequency region. The low-frequency tail corresponds to the blocking effect at the electrolyte-electrode interface, consistent with the fact that the anions are unable to diffuse into the stainless steel plate.

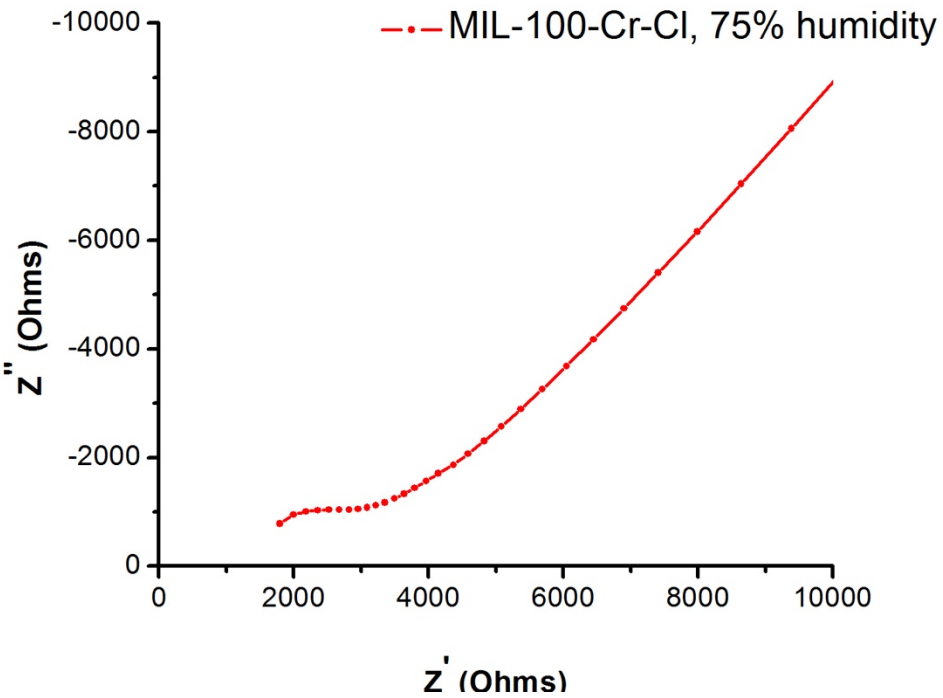

Figure 3- 18. A representative Nyquist plot for MIL-100-Cr-Cl

Here, bulk and boundary contributions to the total resistivity are not resolved clearly into two separate semicircles at the high frequency region. Analysis on MIL-100-Cr-Cl in ambient environment gave a conductivity of 1.4×10^{-6} S $cm^{-1}$and rose all the way up to 1.6×10^{-5} S cm^{-1} as the relative humidity increased to 99.9% (Figure 4-19).

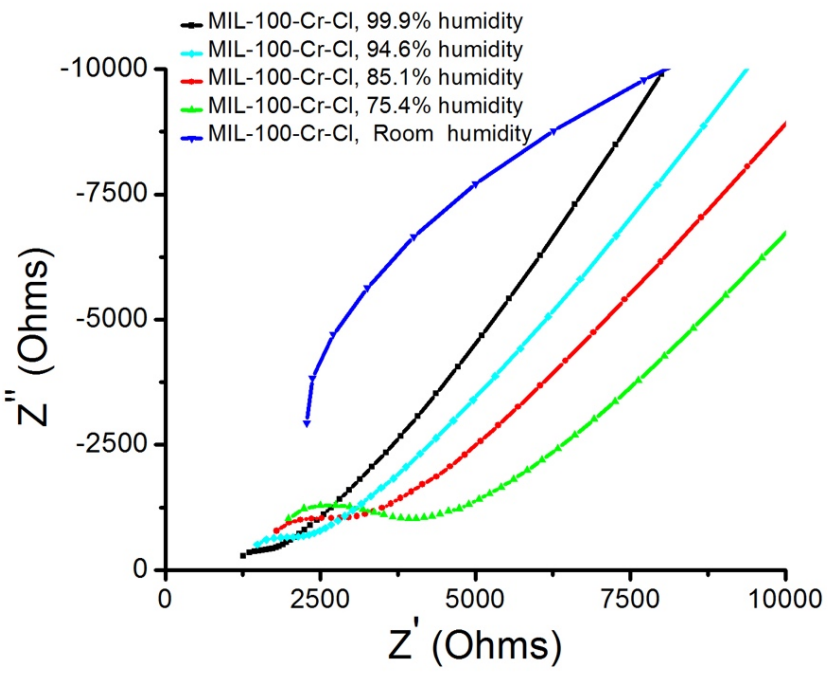

Figure 3- 19. Nyquist plot of MIL-100-Cr-Cl under different humidity

Similar trend was observed for MIL-100-Fe-Cl (Figure 4-20), which had a lower conductivity of about 1.3×10^{-6} S cm^{-1} at low humidity, but reached 6.0×10^{-5} S cm^{-1} at 99.9% RH. Considering the comparable charge carrier concentration, significant difference in conductivities between MIL-100-Cr-Cl and MIL-100-Fe-Cl might be related to the differing Cl^- mobility within the framework, resulting from different interaction between Cl^- ions and frameworks, especially the metal ions (Cr^{3+} vs. Fe^{3+}) with open metal sites but different Lewis hardness. And the conductivity shown here are within the range of other MOF based ion conductors, which varies from 10^{-3} S cm^{-1} to 10^{-7} S cm^{-1}.[5d]

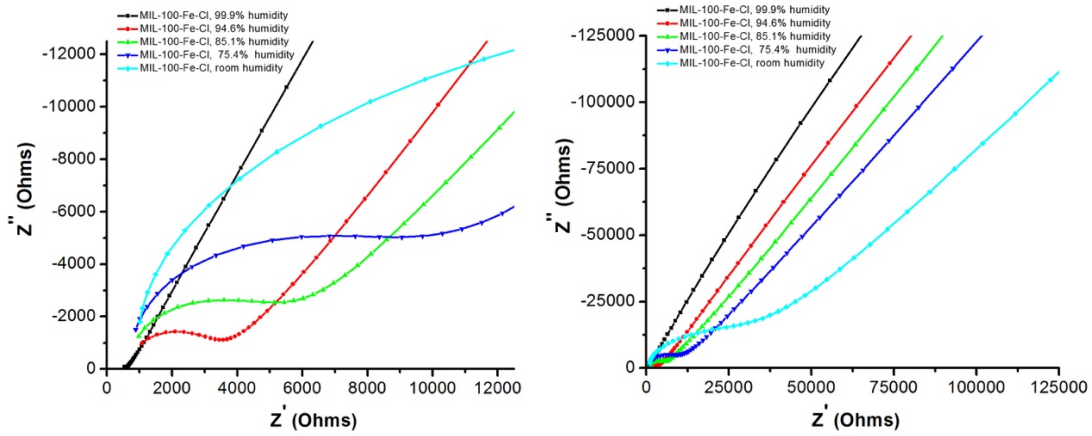

Figure 3- 20. S13 Nyquist plots of MIL-100-Fe-Cl under different humidity, the enlarged figure (Left) and the full view (Right)

To further demonstrate the significant enhancement in conductivity following our post-synthetic modification, The AC measurement was also performed on unmodified MIL-100-Cr-F and MIL-100-Fe-F at 99.9% RH (Figure 4-21) but the radius of the semicircle at the high-frequency region was significant larger than the modified one, indicating the poor conducting nature of unmodified MIL-100-Cr-F and MIL-100-Fe-F where no mobile anions were present.

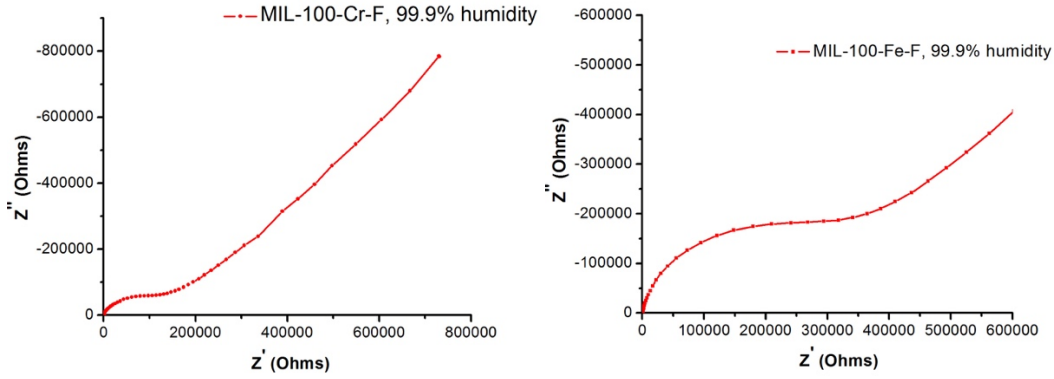

Figure 3- 21. Nyquist plots for MIL-100-Cr-F and MIL-100-Fe-F under 99.9% humidity

When Cl^- ions were partially replaced by OH^- in MIL-100-Cr, we could still observe increasing conductivity for MIL-100 Cr-OH as the humidity increased (Figure 4-22). However, it was lower than that of MIL-100-Cr-Cl. The decreased conductivity might be due to the stronger interaction between OH^- and the framework, resulting in the lower mobility of OH^- compared to Cl^- ions.

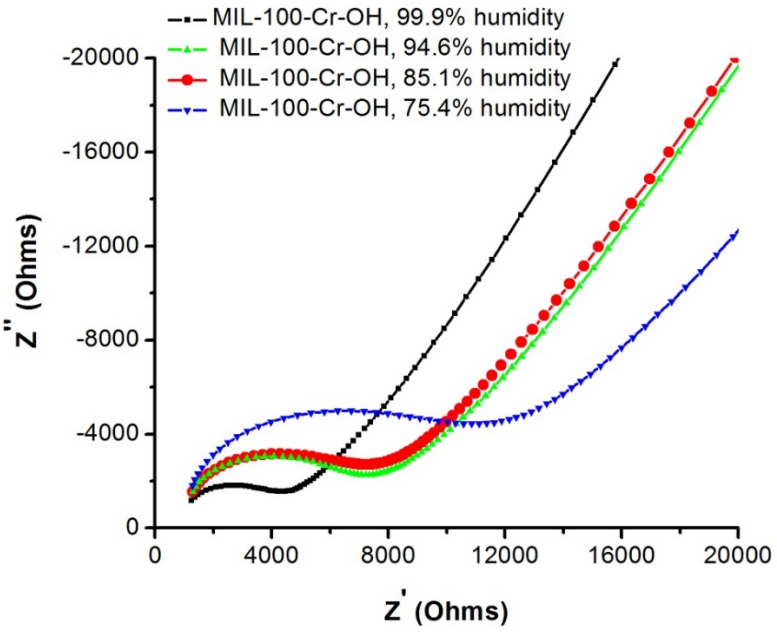

Figure 3- 22. The Nyquist plot of MIL-100-Cr-OH under different humidity

When the sample was heated up while maintaining the same relative humidity, pressed semicircle appeared at the high-frequency region, corresponding to an enhanced conductivity. This trend was expected from the Arrhenius relationship, which indicated the temperature dependence of charge carrier mobility. In fact, the conductivity of MIL-

100-Cr-OH was found to follow the linear relationship with temperature in the Arrhenius plot, as shown in Figure 4-23.

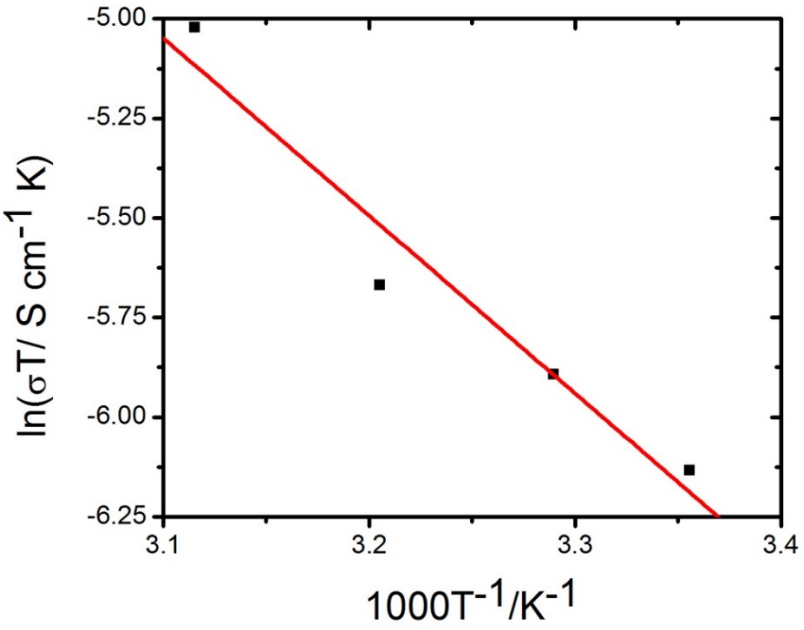

Figure 3- 23. The Arrhenius plot for MIL-100-Cr-OH

3.4 Conclusion

In summary, we have presented an effective approach to produce cationic metal-organic frameworks with mobile anions by post-synthetic modification on a neutral framework. A dramatic enhancement in the ion conductivity was observed following the F^- stripping, coupled with the introduction of mobile Cl^-/OH^- anions. The mobility of extra-framework anions were also confirmed by anion exchange with anionic or cationic organic dyes. The synthetic method reported here should be generally applicable to other materials as well and represents a new avenue for the development of cationic

framework materials with mobile and conducting anions with potential applications in fuel cells.

3.5 References

1. a) Zheng, S.; Bu, J. T.; Li, Y.; Wu, T.; Zuo, F.; Feng, P.; Bu, X. J. Am. Chem. Soc., 2010, 132, 17062–17064. b) Li, J.-R.; Kuppler. R. J.; Zhou, H.-C. Chem. Soc. Rev., 2009, 38, 1477-1504. c) Xiao, B.; Wheatley, P.S.; Zhao, X.B.; Fletcher, A.J.; Fox, S.; Rossi, A.G.; Megson, I.L.; Bordiga, S.; Regli, L.; Thomas, K.M.; Morris, R.E. J. Am. Chem. Soc., 2007, 129, 1203-1209. d) Nugent, P.S; Belmabkhout, Y.; Burd, S. D.;Cairns, A. J.; Luebke, R.; Forrest, K.; Pham, K.; Ma, Q.; Space, B.; Wojtas, L.; Ed-daoudi, M.; Zaworotko, M. J. Nature, 2013, 495, 80-84.

2. a) Wang,C.; DeKrafft, K. E.; Lin,W. J. Am. Chem. Soc., 2012, 134, 7211–7214, b) Gao,J.; Bai, L.; Zhang, Q.; Li, Y.; Rakesh, G.; Lee, J.-M.; Yang, Y.; Zhang, Q.; Dalton Trans., 2014, 43, 2559-2565, c) Pullen, S.; Fei, H.; Orthaber, A.; Cohen, S. M.; Ott, S. J. Am. Chem. Soc., 2013, 135, 16997-17003, d) Dau, P. V.; Cohen, S. M. Chem. Commun., 2013, 49, 6128-6130.

3. Horcajada, P.; Gref, R.; Baati, T.; Allan, P. K.; Maurin, G.; Cou-vreur, P.; Ferey, G.; Morris, R.E.; Serre, C. Chem. Rev., 2012, 112, 1232-1268.

4. a) Morozan, A.; Jaouen, F.; Energy Environ. Sci., 2012, 5, 9269-9260. b) Narayan, T.C.; Seki, S.; Dincă, M. J. Am. Chem. Soc., 2012, 134, 12932-12935. c) Wade, C.R.; Li, M.; Dincă, M. Angew. Chem. Int. Ed., 2013, 52, 13377-13381. d) Dan-Hardi, M.; Serre, C.; Frot, T.; Rozes, L.; Maurin, G.; Sanchez, C.; Ferey, G.; J. Am. Chem. Soc., 2009, 131, 10857-10859. e) Hendon, C.H.; Tiana, D.; Fontecave, M.; Schanze, C.; D'arras, L.; Sassoye, C.; Rozes, L.; Mellot-Draznikes, C.; Walsh, A.; J. Am. Chem. Soc., 2013, 135, 10942-10945. f) Gao, J.; Miao, J.; Li, P.-Z.; Teng, W.Y.; Yang, L.; Zhao, Y.; Liu, B.; Zhang, Q.; Chem. Commun., 2014, 50, 3786-3788

5. a) Sadakiyo, M.; Yamada, T.; Kitagawa, H. J. Am. Chem. Soc., 2009, 131, 9906-9907. b) Yamada, T.; Sadakiyo, M.; Kitagawa, H. J. Am. Chem. Soc., 2009, 131, 3144-3145. c) Shigematsu, A.; Yamada, T.; Kitagawa, H. J. Am. Chem. Soc., 2011, 133, 2034-2036. d) Yoon, M.; Suh, K.; Natarajan, S.; Kim, K. Angew. Chem. Int. Ed., 2013, 52, 2688-2700. e) Zhao, X.; Mao, C.; Bu, X.; Feng, P. Chem. Mat., 2014, 26, 2492- 2495. f) Ponomareva, V. G.; Kovalenko, K. A.; Chupakhin, A.P.; Dybesev, D.N.; Shutova, E. S.; Fedin, V.P. J. Am. Chem. Soc., 2012, 134, 15640-15643. g) Jeong, N. C.; Samanta, B.; Lee, C. Y.; Farha, O. K.; Hupp, J. T. J. Am. Chem. Soc., 2012, 134, 51-54. h) Sahoo, S. C.; Kundu, T.; Banerjee, R. J. Am. Chem. Soc., 2011, 133, 17950-17958. i) Pardo, E.; Train, C.; Gontard, G.; Boubekeur, K.;

Fabelo, O.; Liu, H.; Dkhil, B.; Lloret, F.; Nakagawa, K.; Tokoro, H.; Ohkoshi, S.; Verdaguer, M. J. Am. Chem. Soc., 2011, 133, 15328-15331.

6. a) Bureekaew, S.; Horike, S.; Higuchi, M.; Mizuno, M.; Kawamu-ra, T.; Tanaka, D.; Yanai, N.; Kitagawa, S. Nat. Mater., 2009, 8, 831-836. b) Hurd, J.A.; Vaidhyanathan, R.; Thangadurai, V.; Ratcliffe, C. I.; Moudrakovski, I. L.; and Shimizu, G. H. K. Nat. Chem., 2009, 1, 705-710.

7. a) Rather, B.; Zaworotko, M. J. Chem. Commun. 2003, 7, 830-831. b) Cheng, J.; Zhang, J.; Zheng, S.; Zhang, M.; Yang, G. Angew. Chem. Int. Ed., 2006, 45, 73-76. c) Lin, H. Y.; Chin, C. Y.; Huang, H. L.; Huang, W. Y.; Sie, M. J. ; Huang, L. H.; Lee, Y. H.; Lin, C. H.; Lii, K. H.; Bu, X.; Wang, S. L. Science, 2013, 339, 811-813. d) Zheng, S.; Mao, C.; Wu, T.; Lee, S.; Feng, P.; Bu, X. J. Am. Chem. Soc., 2012, 134, 11936-11939.

8. Steele, B.C.H.; Heinzel, A. Nature, 2011, 414, 345-352.

9. Hickner, M. A.; Ghassemi,H.; Kim, Y. S.; Einsla, B. R.; McGrath, J. E. Chem. Rev., 2004, 104, 4587-4612.

10. a) Varcoe J.R.; Slade, R. C. T. Fuel Cells, 2005, 5, 187-200. b) Gu, S.; Skovgard, J.; Yan, Y.S. ChemSusChem, 2012, 5, 843-848

11. Sadakiyo, M.; Kasai, H.; Kato, K.; Takata, M.; Yamauchi, M. J. Am. Chem. Soc., 2014, 136, 1702-1705.

12. a) Fei, H.; Oliver, S. R. J. Dalton Trans. 2010, 39, 11193-11200. b) Chang, Y. C.; Wang, S. L. J. Am. Chem. Soc., 2012, 134, 9848-9851.

13. a) Cohen, S. M. Chem. Rev., 2012, 112, 970-1000 b) Fei, H.; Cahill, J. F.; Prather, K. A.; Cohen. S. M. Inorg. Chem., 2013, 52, 4011-4016. c) Zhang, Z.; Zhang, L.; Wojtas, L.; Nugent, P.; Eddaoudi, M.; Zaworotko, J. M. J. Am. Chem. Soc., 2012, 134, 924-927. d) Zhang, Z.; Gao, W.; Wojtas, L.; Ma, S.; Eddaoudi, M.; Zaworotko, J. M. Angew. Chem. Int. Ed., 2012, 51, 9330 –9334. e) Wade, C. R.; Corrales-Sanchez, T.; Narayan, T.; Dincă, M. Energy Environ. Sci., 2013, 6, 2172-2177.

14. a) Ferey, G.; Serre, C.; Mellot-Draznieks, C.; Millange, F.; Surblé, S.; Dutour, J.; Margiolaki, I. Angew. Chem. Int. Ed., 2004, 43, 6296 –6301. b) Kim, M.; Cahill, J. F.; Fei, H.; Prather, K. A.; Cohen, S. M. J. Am. Chem. Soc., 2012, 134, 18082-18088.

15. Ferey, G.; Mellot-Draznieks, C.; Serre, C.; Millange, F.; Dutour, J.; Surblé, S.; Margiolaki, I. Science, 2005, 309, 2040-2042

16. Gul-E-Noor, F.; Jee, B.; Poppl, A.; Hartmann, M.; Himsl, D.; Bertmer, M. Phys. Chem. Chem. Phys., 2011, 13, 7783-7788.

17. a) Fei, H.; Rogow, D. L.; Oliver, S. R. J. J. Am. Chem. Soc., 2010, 132, 7202-7209. b) Fei, H.; Bresler M. R.; Oliver, S. R. J. J. Am. Chem. Soc., 2011, 133, 11110-11113.

18. Zhao, X.; Bu, X.; Wu, T.; Zheng, S.; Wang,.L; and Feng, P. Nat. Commun., 2013, 4, 2344.

19. Vimont, A.; Goupil, J. M.; Lavalley, J. C.; Daturi, M.; Surblé, S.; Serre, C.; Millange, F.; Férey, G.; Audebrand, M. *J. Am. Chem. Soc.,* **2006,** 128, 3218-3227

20. Yoon, J.; Seo, Y.; Hwang, Y. K.; Chang, J.; Leclerc, H.; Wuttke, S.; Bazin, P.; Vimont, A.; Daturi, M.; Bloch, E.; Llewellyn, P. L.; Serre, C.; Horcajada, P.; Grenèche, J.; Rodrigues, A. E.; Férey, G. *Angew. Chem. Int. Ed.,* **2009,** 49, 5949–5952

21. J. Jeener, B. H. Meier, P. Bachmann, R. R. Ernst., *J. Chem. Phys.,* **1979**, 71, 4546-4563

Chapter 4
Metal Organic Frameworks derived carbon materials for efficient oxygen electrochemical reduction reactions

4.1 Introduction

Metal-organic frameworks (MOFs) have received increasing attention due to their potential applications in many areas such as gas adsorption[1-4] and separation,[5, 6] catalysis,[7, 8] photoluminescent,[9-12] drug delivery,[13] photoelectrochemistry[14-17] and ionic conductivity.[18-20] Recently, MOFs have also been used as precursors or templates to synthesize new forms of porous carbons because they offer a number of unique advantages.[21] One is their highly ordered porous structures with abundant and varied organic species, which makes it feasible to obtain carbon with hierarchical pore structures under proper thermolysis conditions.[22] Another advantage is their regular arrangement of metal nodes and heteroatoms (e.g., nitrogen), which makes them predisposed to form uniformly distributed metal species and other dopants. Moreover, the topology and metal ion variation in MOFs allow the tuning of different product morphologies such as disks, fibers and tubes.[23-26]

The past several years have witnessed significant progresses in using MOFs as staring materials for carbon composite synthesis. For example, the N-rich composition in imidazole has made zeolitic imidazolate frameworks (ZIFs) widely used as precursors in preparing N-doped carbon materials with high electrocatalytic performance.[27, 28] ZIFs coupled with phenanthroline and ferrous

acetate can produce a Fe-based electrocatalyst with the power density comparable to that of a state-of-the-art Pt-based cathode.[29] The presence of additives such as dicyandiamide (DCDA) can promote the formation of various morphologies such as nanotubes[23, 30] and nanopolyhedra.[25] Other MOFs (e.g., MOF-5) have also been employed as precursors to develop porous carbons and investigate the effects of dopants.[31] The richness in design strategies and synthetic possibilities have inspired great interest in applying MOF-derived carbons in energy conversion and storage.

One particular area in which MOF-derived heteroatom-decorated carbon materials can play an important role is the catalysis for oxygen reduction reactions in fuel cells. Due to their higher efficiency and lower emission over conventional combustion engine, fuel cells (FCs) have earned enormous attention and growing market share.[32] However, the sluggish kinetics of cathodic oxygen reduction reaction (ORR) seriously impedes its further development and use.[33] Current catalyst technology is dependent on platinum[34-36] that is not only scarce and expensive but also disproportionately geographically distributed. Moreover, it has intrinsic drawbacks such as poor stability and susceptibility to methanol crossover.[37] As an alternative to Pt-based materials, carbon materials[38, 39] possess several notable advantages such as high poisoning tolerance, long-term operational stability and cost-effectiveness.[40, 41] In particular, carbon composites containing heteroatoms such as N[42, 43] and transition metals[44-46] have shown

promising activity towards ORR in multiple media as these heteroatoms can play a critical role in active sites evolution.

4.2 Experimental Section

4.2.1 Preparation of MIL-100

MIL-100-Fe-F was prepared by hydrothermal reactions following the procedures reported by Ferey et. al.[60] A reaction mixture of molar composition 1.0 Fe: 0.66 trimesic acid: 2.0 HF: 1.2 HNO_3: 280 H_2O was held at 150^{o}C in a Teflon-lined autoclave for 12h. The light-orange solid product was recovered by filtration and washed with deionized water, followed by treatment in hot DI water (80^{o}C) and hot ethanol (60^{o}C) sequentially to remove residual trimesic acid. The as-prepared material was degassed under vacuum at 150^{o}C overnight before further treatment.

4.2.2 Hydrolysis of MIL-100 and N-Containing Organic Molecules

MIL-100-Fe (200 mg) was mixed with 5-aminotetrazole (400 mg) and grounded with pestle and mortar for 30 min. The mixture was sealed in the quartz tube and moved to the tube furnace, followed by a heating in the Ar flow for 3 h. The ramp was 6 ^{o}C /min and target temperature was set as X ^{o}C, where X= 600, 700, 800 and 900 respectively. The as-obtained samples were named as Fe-NC-600, 700, 800 and 900, respectively.

The as-obtained Fe-NC-X was placed in 5 M HCl aqueous solution and kept under stir for 24 h. The sample was then recovered by filtration and washed with H_2O and ethanol. The as-obtained samples were named as NC-600, 700, 800 and 900, respectively.

200 mg MIL-100-Fe was mixed with 400 mg dicyandiamide, urea or melamine and grounded with pestle and mortar for 30 min. The mixture was sealed in the quartz tube and moved to the tube furnace, followed by a heating in the Ar flow for 3 h. The ramp was 6 ^{o}C /min and target temperature was set as 800 ^{o}C. The as-obtained samples were placed in 5 M HCl aqueous solution and kept under stir for 24 h. The sample was then recovered by filtration and washed with H_2O and ethanol. The as-obtained samples were named as MIL- dicyandiamide, urea and melamine respectively.

400 mg MIL-100-Fe was grounded with pestle and mortar for 30 min. The solid was sealed in the quartz tube and moved to the tube furnace, followed by a heating in the Ar flow for 3 h. The ramp was 6 ^{o}C /min and target temperature was set as 800 ^{o}C. The as-obtained samples were placed in 5 M HCl aqueous solution and kept under stir for 24 h. The sample was then recovered by filtration and washed with H_2O and ethanol. The as-obtained sample was named as MIL-C.

4.2.3 Characterization

Powder X-ray diffraction data were collected using a Bruker D8 Advance powder diffractometer operating at 40 kV, 40mA with Cu Kα (λ =1.5418 Å) radiation. N_2 adsorption/desorption measurements were carried out at 77 K on a Micromeritics ASAP 2020 analyzer. The morphology of products were examined by using a Philips FEI XL30 field emission scanning electron microscope (FESEM). Semi-quantitative elemental analyses and elemental mappings of different

samples were carried out using a PGT-IMIX PTS energy dispersive spectroscopy (EDS) detector attached to the FESEM. Transmission electron microscopy (TEM) was performed with an FEI-Philips CM300 microscope, equipped with a LaB_6 electron gun. Selected-area electron diffraction (SAED) patterns and high-resolution images were obtained to distinguish different phases within the material. X-ray photoelectron spectroscopy (XPS) characterization was carried out by using a Kratos AXIS ULTRADLD XPS system equipped with an Al Kα monochromated X-ray source and a 165-mm mean radius electron energy hemispherical analyzer.

4.2.4 Electrochemical Measurement

The electrochemical experiments were carried out in a voltammetric cell at room temperature using a three-electrode configuration. A glassy carbon rotating disk electrode (RDE) was utilized as working electrode, an Ag/AgCl electrode as a reference electrode, and a Pt electrode served as counter electrode. Prior to the measurements, the working electrode was polished first and then modified by pipetting the catalyst slurry. The slurry was prepared through dispersing 5 mg of active materials in 0.64 ml alcohol solution containing 40 μL of a 5 wt% Nafion solution by sonication. Then the electrode was dried at room temperature before the test. The general loading mass of active materials on the working electrode is

0.1 mg cm^{-2}. A commercially available 20wt% Pt-C catalyst obtained from Alfa Aesar was used for comparison.

Cyclic voltammetry (CV) experiments were carried out in O_2 or N_2 saturated 0.1 M KOH solution. The potential was varied from 0 V to 1.2 V at a scan sweep of 10mV/s. In rotating disk electrode (RDE) tests, the linear sweep voltammograms (LSVs) were carried out in O_2 or N_2 saturated 0.1 M KOH solution. The potential was scanned from 1.2 V to 0 V at a scan sweep of 10mV/s at various rotating speeds from 400 to 2500 rpm.

All the potentials are calibrated to the RHE potential according to the method reported in the literatures. The ORR current density is obtained by subtracting the current density measured in Ar-saturated electrolyte from the current density measured in O_2-saturated electrolyte. The onset ORR potential was defined as the electrode potential where ORR current density is 3 μA cm^{-2} in RDE polarization curves. The Koutecky-Levich (K-L) equations have been used to calculate the kinetic parameters:

$$\frac{1}{J} = \frac{1}{J_K} + \frac{1}{J_L} = \frac{1}{J_K} + \frac{1}{B\omega^{\frac{1}{2}}}$$

$$B = 0.62nFC_0D_0^{\frac{2}{3}}v^{-\frac{1}{6}}$$

$$J_K = nFkC_0$$

, Where J, J_K and J_L are the measured current density, kinetic- and diffusion-limiting current densities, respectively; ω is the angular velocity of the rotating disk, n is the electron-transfer number in ORR, F is the Faraday constant (F=96485 C/mo), C_0 is the bulk solubility of O_2, D_0 is diffusion coefficient of O_2, v is the kinetic viscosity of the electrolyte,

and k is the electron transfer rate constant. The number of electrons transferred (n) and J_K can be obtained from the slope and intercept of the K-L plots (In 0.1 M KOH, $C_0=1.2\times10^{-3}$ mol L^{-1}, $D_0=1.9\times10^{-5}$ cm s^{-1}, v= 0.01 cm^2 s^{-1}).

Durability test was carried out in O_2 saturated 0.1 M KOH solution. The working electrode with active materials was rotating at a speed of 1600 rpm for over 11h and the potential was set at 0.55 V. In methanol tolerance test, the reaction time was set as 20000 s while 3 mL methanol was added to KOH solution at 1000 s for NC-800. For Pt-C, the reaction time was set as 15000 s while 3 mL methanol was added to KOH solution at 300 s.

4.3 Results and Discussion

4.3.1 Materials Synthesis and Crystallinity

Here, we report the synthesis, characterizations, and electrocatalytic activities of nitrogen doped hierarchically porous spherical carbon shells embedded with Fe nanoparticles through the simultaneous decomposition and evolution of an iron containing $Fe^{III}_3O(H_2O)_2F$[illegible]$\{C_6H_3(CO_2)_3\}_2$[illegible]$nH_2O(n\approx14.5)$ template (MIL-100-Fe), which also acts as carbon and iron precursors (Figure 5-1).[47, 48] MIL-100-Fe was chosen because of its unique combination of topological and compositional features. Its high surface area helps promote both meso- and micro-porosity in the resulting catalyst, which contributes to enhanced mass transportation and greater accessibility to active sites in ORR process. Importantly, the presence of Fe contributes to enhanced crystallinity in the formed graphitic carbon during

carbonization because Fe embedded in the MIL structure could form Fe species upon heating, which could subsequently act as catalysts to promote the in situ crystallization of carbon and control its morphology.[23, 49] Furthermore, we identified two Fe-forms upon carbonization: Fe_3C which is susceptible to acid leaching and leads to porosity; and embedded metallic Fe nanoparticles which serves as potential active sites as well as significantly enhance stability and poisoning tolerance of carbon catalysts synthesized here. To achieve greater catalytic activity, in this work we have experimented with a number of N-containing additives to search for the best possible N-doping conditions by systematically studying the effects of different nitrogen additives and carbonization temperature on catalytic activities.[50]

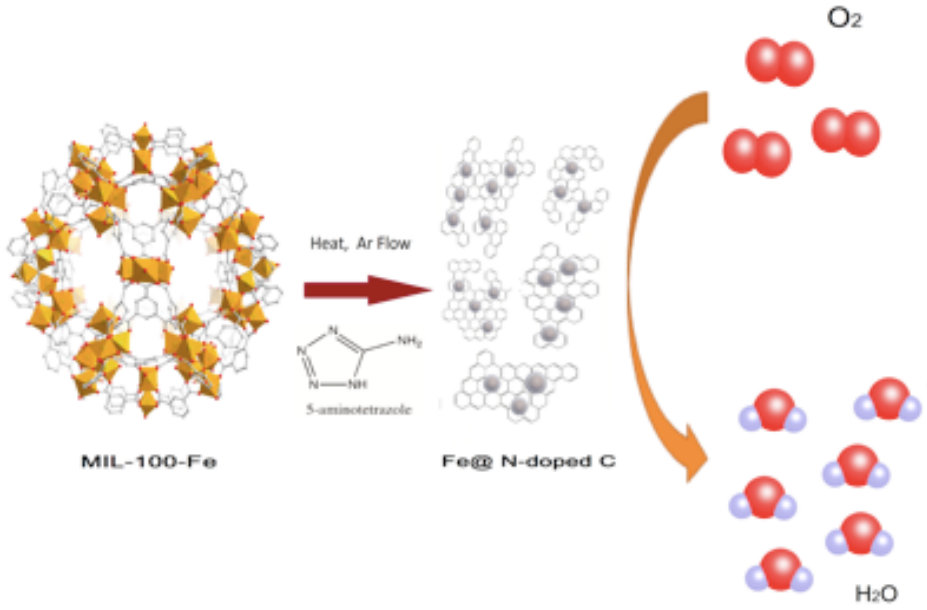

Figure 4- 1. Carbon shells embedded with Fe nanoparticles prepared from MOFs for oxygen reduction reactions

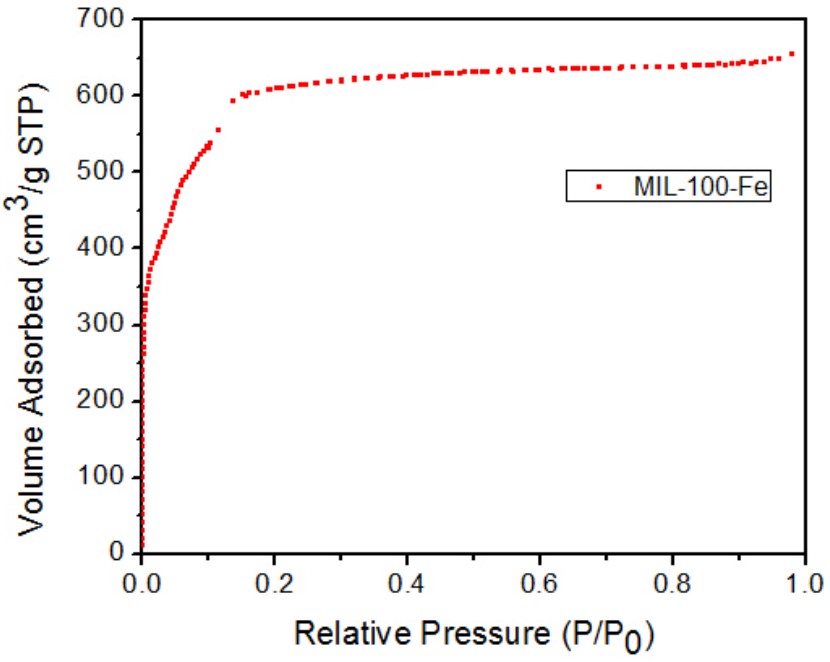

Figure 4- 2. The nitrogen adsorption-desorption isotherms of MIL-100-Fe.

As-obtained MIL-100-Fe has a high surface area of 1794.40 m^2/g (Figure 5-2). Pyrolysis of the MIL-100-Fe precursor and nitrogen containing organics mixture at temperature ranging from 600 to 900° C gave Fe-containing carbons (named as Fe-NC-X, where X is pyrolysis temperature), as revealed in powder X-ray diffraction (PXRD, Figure 5-3).

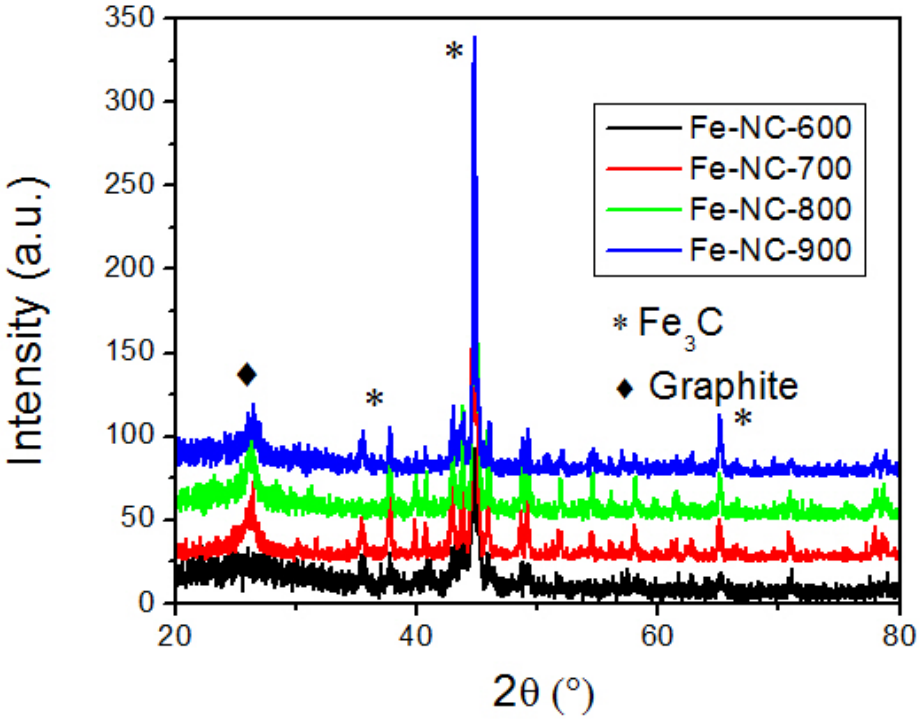

Figure 4- 3. PXRD patterns of Fe-NC-600, 700, 800 and 900.

This suggests that MIL-100-Fe decomposed during pyrolysis while Fe was transformed to various species.[30] Most Fe species can be removed by acid leaching and remaining carbon materials (named as NC-X) can be recovered by filtration and

thorough wash. The appearance of sharp diffraction peaks of NC-700, 800 and 900 around 26° after acid leaching can be assigned to the (002) diffraction of graphite and confirm the formation of highly crystalline graphitic carbon (Figure 5-4) while NC-600 has a lower crystallinity. In addition, the increase of this characteristic peak intensity correlates well with the elevated pyrolysis temperature, indicating the critical role of temperature in crystallization. Moreover, the small diffraction peaks around 44.8° indicates the existence of some metallic Fe species even after the acid leaching.[51]

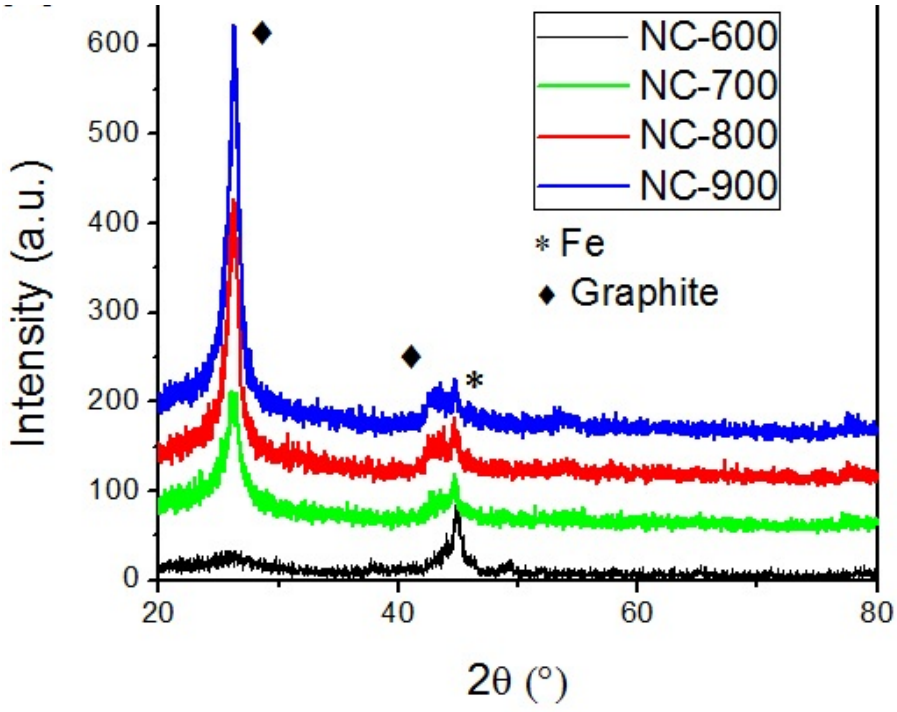

Figure 4- 4. PXRD Patterns of NC-600, 700, 800 and 900.

4.3.2 Electron Microscopy and Porous Structure

Figures 5-5A&B display typical transmission electron microscopy (TEM) images of NC-800, which mostly consist of a carbon shell embedded with iron particles. The shell has a diameter of around 40 nm while the particles encapsulated inside is around 25 nm. The selected area electron diffraction (SAED) patterns of such a core-shell structure give several rings superimposed by some scattered dots, as shown in Figure 5-5C. Rings can be assigned to the graphitic carbon shells, while scattered dots come from the diffraction of metallic iron within the shell. The presence of such metallic iron nanoparticles confirms that the small diffraction peaks in NC-X come from crystallized metallic Fe. Also, the formation of carbon shells is consistent with previous reports that Fe species are favorable for morphology control of carbon materials.[23, 49, 52] The interplane spacing of the shell is calculated to be 0.34 nm from the SAED patterns, in agreement with the interlayer distance of graphite.

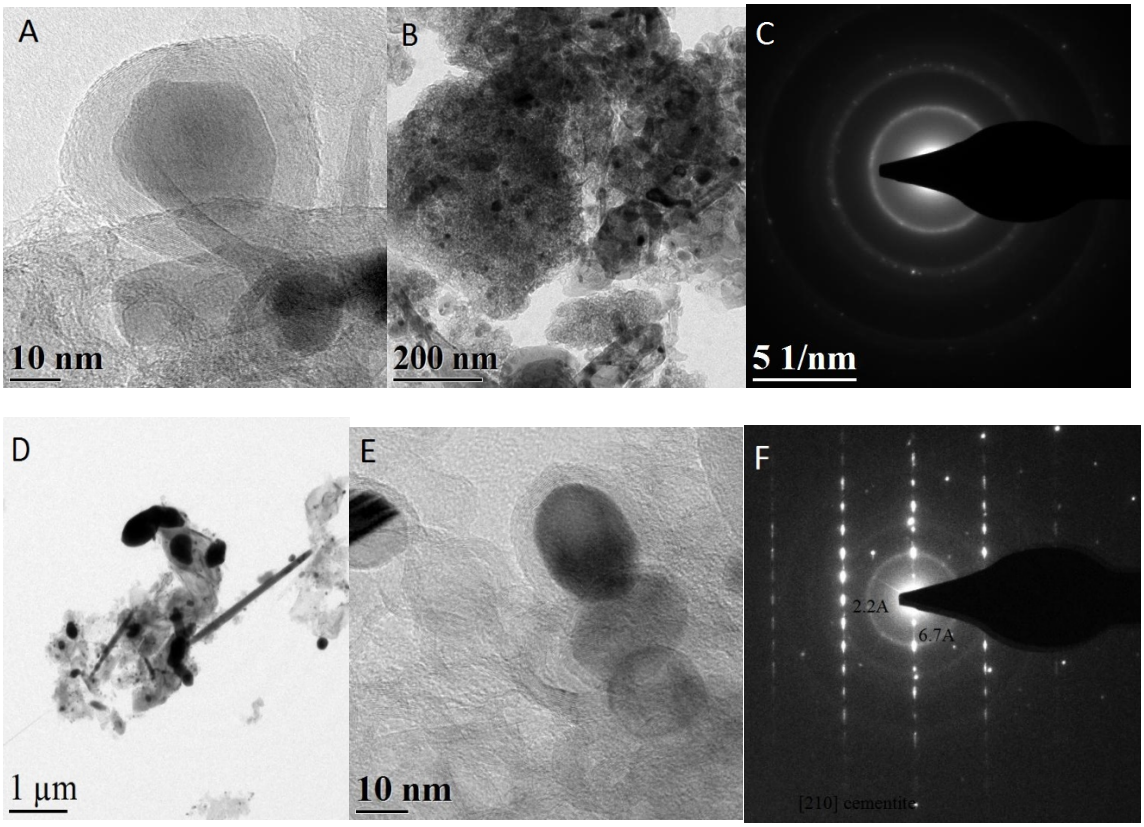

Figure 4- 5. Typical TEM images of NC-800 (A, B). SAED patterns of NC-800 (C). Typical TEM images of Fe-NC-800 (D, E). SAED patterns of Fe-NC-800 (F).

Energy dispersive X-ray spectroscopy (EDS) spectrum was collected on the same sample (Figure 5-6A). Besides carbon and Fe, nitrogen was also identified, proving the successful introduction of nitrogen into graphitic carbon. Elemental mapping further illustrates the co-existence of carbon and nitrogen and the uniform distribution of such elements throughout the as-obtained compound (Figure 5-7).

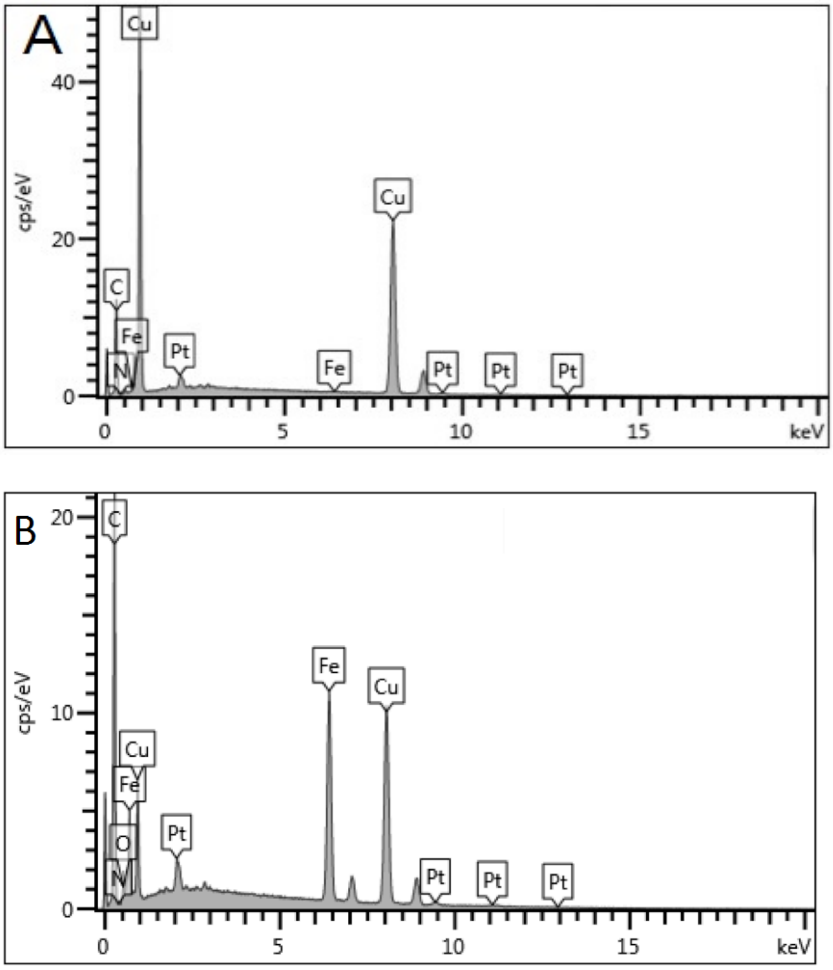

Figure 4- 6. EDS images of NC-800 (A). EDS spectrum of Fe-NC-800 (B). Pt signal comes from coating during SEM sample preparation and Cu signal comes from the SEM sample substrate we used.

Samples of Fe-NC-800 were also examined by TEM and similar core-shell structures were observed in TEM images (Figures 5-5D&E). Moreover, big black aggregates and rod-like species are also shown in TEM images. The SAED of such species (Figure 5-5F) gives a [210] diffraction pattern of cementite, a well-crystallized Fe_3C species, indicating the formation of such phases in the carbonized samples.

EDS spectrum (Figure 5-6B) also shows a more prominent Fe peak compared to the acid-leached samples. This phenomenon matches well with the strong Fe_3C signals of Fe-NC-X samples from PXRD analysis (Figure 5-3). The lack of such aggregates and rods in samples of NC-X and the disappear of corresponding diffraction patterns in PXRD and SAED confirm the effectiveness of acid leaching in removing Fe3C species and stability of iron nanoparticles encapsulated in carbon spheres. Similar constructions of iron species as the core and carbon tubes as the protective wall was reported previously and was believed to contribute to the stability and activity of such carbon materials in ORR.[50-52]

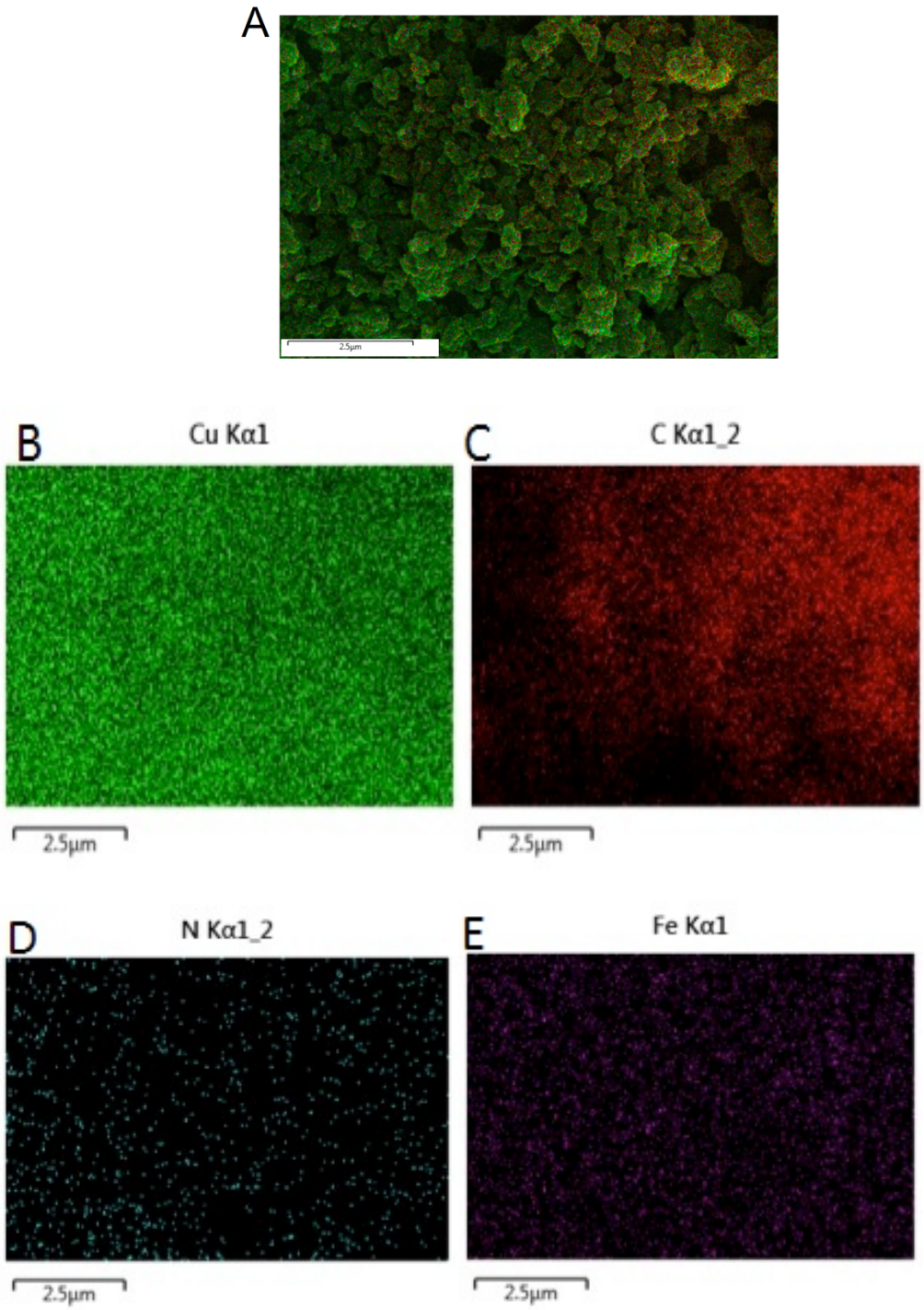

Figure 4- 7.Space EDS mapping of NC-800 and corresponding elements. Cu comes from the substrate we use.

Pore structure is another pivotal factor determining the ORR catalytic performance. As shown in Figure 5-8, the as-obtained Fe-NC-800 possesses a typical type IV isotherm with a capillary condensation step and a hysteresis loop in the desorption branch, indicating the presence of both micropores and mesopores. The presence of mesopores promotes mass transportation to allow reactants such as O_2 to reach the active sites within catalysts.[53, 54] Simultaneously, micropores can trap O_2 molecules and expose more active sites, which promotes the catalytic process.[40, 45] Moreover, by removing Fe_3C species in the composite, micropores area doubled from 55 m^2/g to 125 m^2/g and mesopores area also increased. As a result, the overall surface area of NC-800 increased to 275 m^2/g, compared to 180 m^2/g for Fe-NC-800. All characterizations above confirm the formation of N-doped carbon shell embedded with metallic Fe nanoparticles as the final product. Such a nitrogen doped carbon composite with hierarchical porous structure constitutes an ideal nano-reactor for ORR reactions.

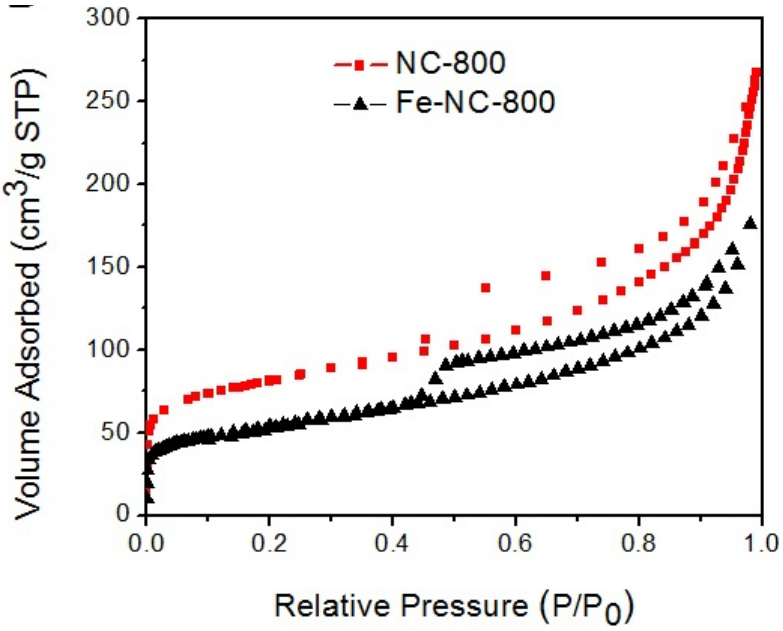

Figure 4- 8. The nitrogen adsorption-desorption isotherms of NC-800 and Fe-NC-800.

4.3.3 Electrochemical Analysis

Motivated by its unique configuration of carbon shells and Fe core, electrocatalytic properties of these new carbon materials were assessed for oxygen reduction reactions. Linear sweep voltammograms (LSVs) were carried out in oxygen saturated 0.1M KOH solution to screen the materials (details in Experimental Section). As seen in Figure 5-9A, the current density was enhanced for samples made with the increasing pyrolysis temperature from 600 to 800° C, as well as the gradually positively shifted onset potential and half wave potential. This is consistent with the degree of crystallinity of these carbon materials since a better graphitic crystallinity would facilitate electron transfer within the electrode. Notably, NC-800 shows the highest catalytic activities based on onset potential and

current density, which is close to the commercial Pt-C catalyst, validating the effectiveness of dopants[55, 56] formed during pyrolysis. Especially, there is increasing evidence that metallic Fe would likely lower the local work function of exterior carbon and increase their activity for electron transfer. Such a process could work in synergy with N dopants in carbon materials to enhance ORR activity.[52] On the other hand, NC-900 has the lowest current density despite its high crystallinity. The apparently negatively shifted onset potential of NC-900 also indicates the lack of active sites. Considering that N is prone to escape by forming gaseous species under high temperature instead of being embedded into carbons, it's believed that the lack of N dopants within the carbon materials results in the deterioration in activity, in agreement with the lower content of N atoms detected by EDS spectrum.

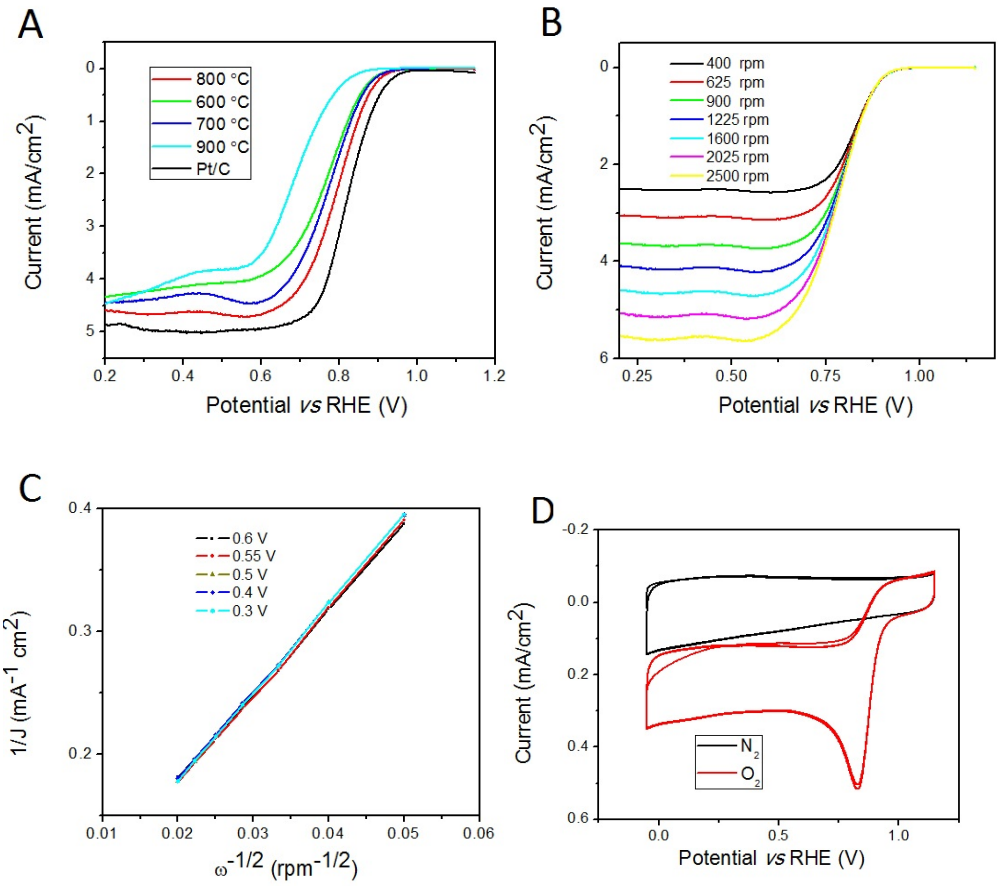

Figure 4- 9. Polarization curves of ORR for MILs annealed under different temperatures at a rotation speed of 1600 rpm in 0.1 M KOH solution (A). LSV plots of ORR for NC-800 with different rotation speeds in 0.1 M KOH solution(B). K-L plots on NC-800 electrode(C). CV of NC-800 in nitrogen and oxygen saturated 0.1M KOH electrolyte(D).

Carbon materials prepared from MIL-100-Fe mixed with several other types of N-containing organics were also tested (Figure 5-10) and they all showed some kind of catalytic activity. Furthermore, the pyrolysis product of pure MIL-100-Fe without any N source showed the lowest activity in terms of onset potential and half-wave potential. These results clearly demonstrate that doped N plays a key role in improving the catalytic performance for ORR.[42]

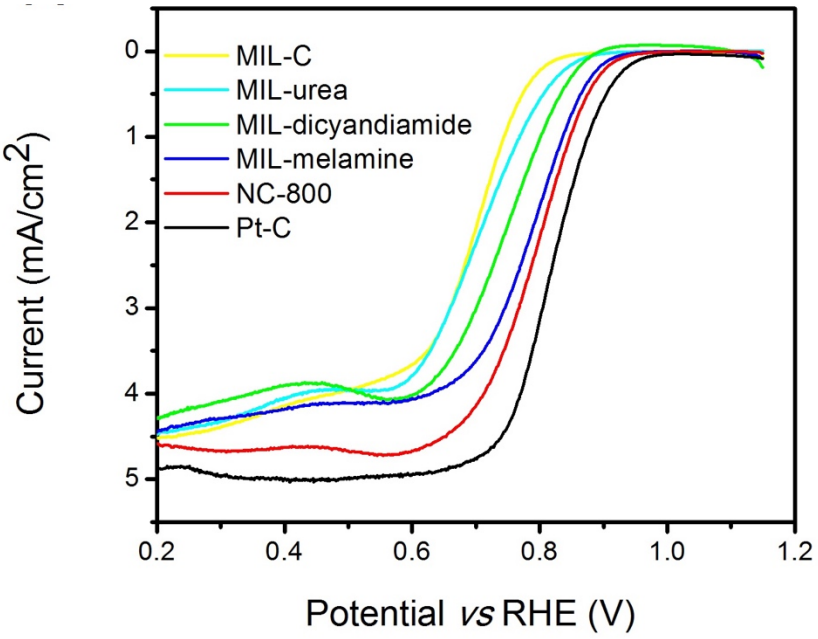

Figure 4- 10. Polarized curves of MILs annealed with different nitrogen-containing organics at a rotation speed of 1600 rpm

To gain further insight into ORR with NC-800 catalyst, the LSVs were performed at different rotating speeds from 400 to 2500 rpm in 0.1 M KOH solution. As seen in Figure 5-9B, the onset potential stayed constant while the enhanced current corresponded well to the increasing rotating speed, due to the facilitated diffusion of oxygen at higher rotating speed. The corresponding Koutecky-Levich (K-L) plots over the potential from -0.4 to -0.7 V vs. RHE show good linearity (Figure 5-9C), implying the first-order reaction kinetics toward O2 reduction in this potential range. According to the K-L equation, the electron-transfer number (n) for ORR in NC-800 was calculated to be from 3.9- 4.1 from -0.4 to -0.7V (Figure 5-11). The closeness to 4 suggests that ORR in NC-800 electrode

predominantly proceeds with the 4-electron transfer pathway with water as the main product.[53]

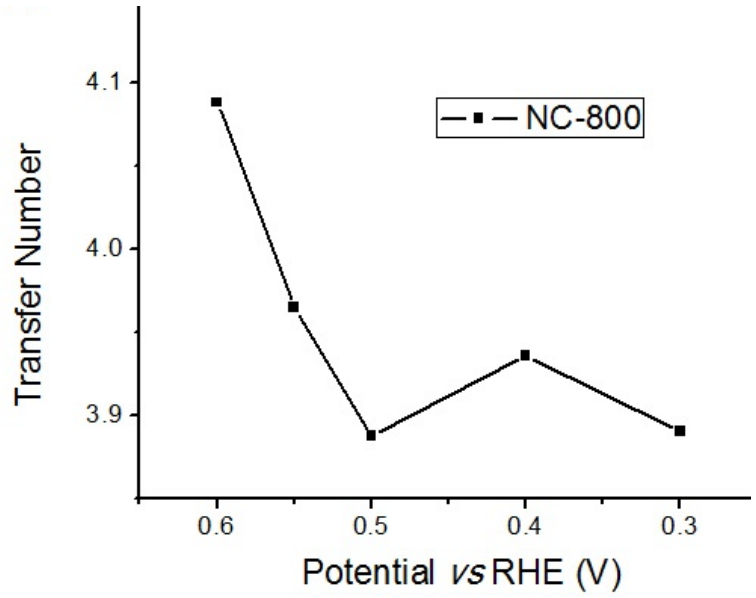

Figure 4- 11. Electron transfer number of NC-800 at various potentials.

Cyclic voltammograms (CVs) were also performed on the best NC-800 electrode in both oxygen and nitrogen saturated 0.1 M KOH solution electrolyte. A featureless CV profile (Figure 5-9D) was obtained in nitrogen saturated electrolyte, indicating no self–oxidization or reduction within the active material. Significantly, a single reduction peak at 0.83 V vs. RHE was spotted in oxygen saturated electrolyte, verifying a good selectivity of full oxygen reduction into water. On-set potential and half-wave potential were determined to be 0.89 V and 0.96 V from the CV profile. The high reduction reaction potentials shown here demonstrate a

superior oxygen reduction activity, even better than previously reported best metal-free N-doped carbon materials.[57] The outstanding activity could be attributed to possible Fe involvement in this carbon material.[29, 58] In contrast, Fe-NC-800 without Fe_3C removal showed an undesired peak at low potentials (Figure 5-12A), which may be associated with the deterioration of the catalyst. Also, the electron-transfer number (n) for ORR in Fe-NC-800 was only 3.6 at -0.5V vs RHE (Figure 5-12B), indicating the existence of two-electron transfer side reaction related to H_2O_2 formation.[55] Both behaviors confirm the necessity of Fe_3C removal to obtain an active catalyst with high selectivity.

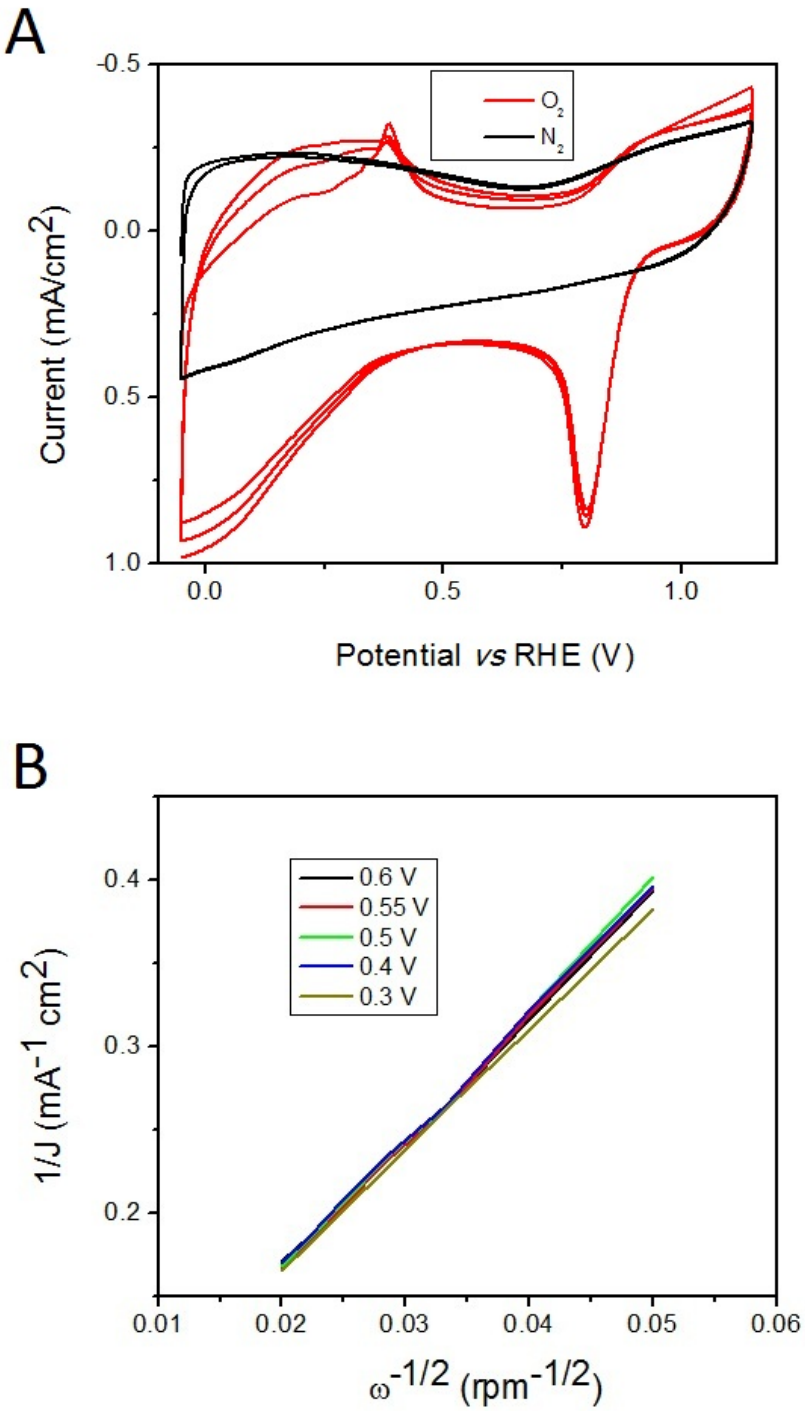

Figure 4- 12. CV of Fe-NC-800 in nitrogen and oxygen saturated electrolyte (A) K-L plots on Fe-NC-800 electrode (B).

4.3.4 X-ray photoelectron spectroscopy

To illustrate the origin of high activity in NC-800, X-ray photoelectron spectroscopy (XPS) was used to investigate the most active NC-800 carbon materials. The total N content in the composite was estimated to be 4.8 % (Table S1) by EDS analysis. The N1s XPS spectrum shown in Figure 5-13A can be deconvoluted into three types of nitrogen atoms, corresponding to pyridinic-N (398.7 eV), pyrrolic-N (400.1 eV) and graphitic-N (401.1 eV), respectively.[44] Though the activity order of these three types of nitrogen is still in debate[57], the presence of all three nitrogen types in NC-800 contributes to the highly active nature of our NC-800 materials. Another small peak at 397 eV may be associated with Fe-N_x species. Fe 2p signals were also collected by XPS (Figure 5-13B). Peaks at 706.9 eV and 719.8 eV could be assigned unambiguously to metallic iron, which is consistent with the observation of metallic iron particles embedded within carbon shells. The remaining peak at 711.0 eV also indicates the presence of Fe-N_x species.[59] All these N species, along with the encapsulated iron nanoparticles, are believed to contribute to the overall high oxygen reduction activity of NC-800 carbon materials.

A

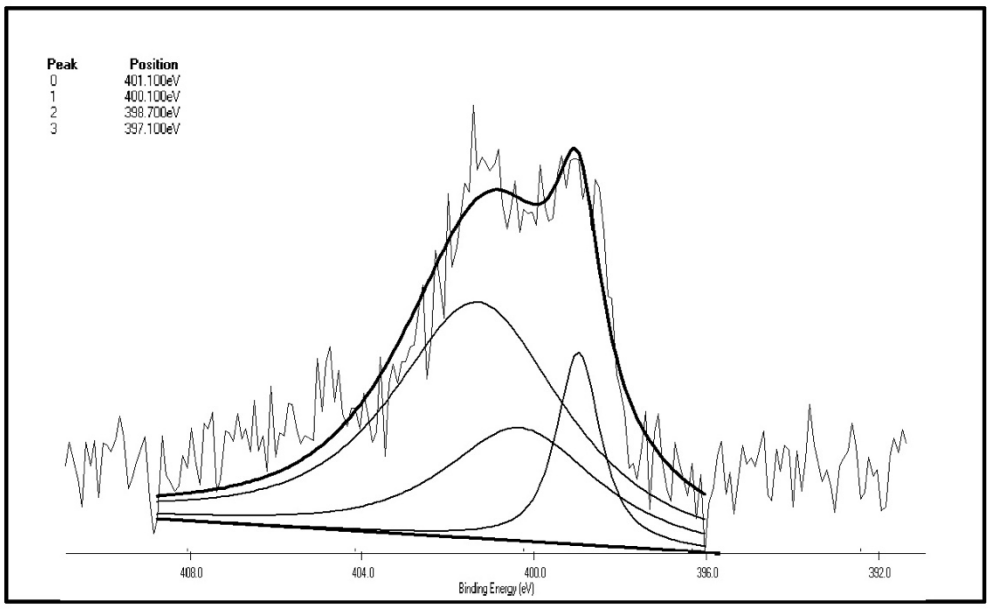

B

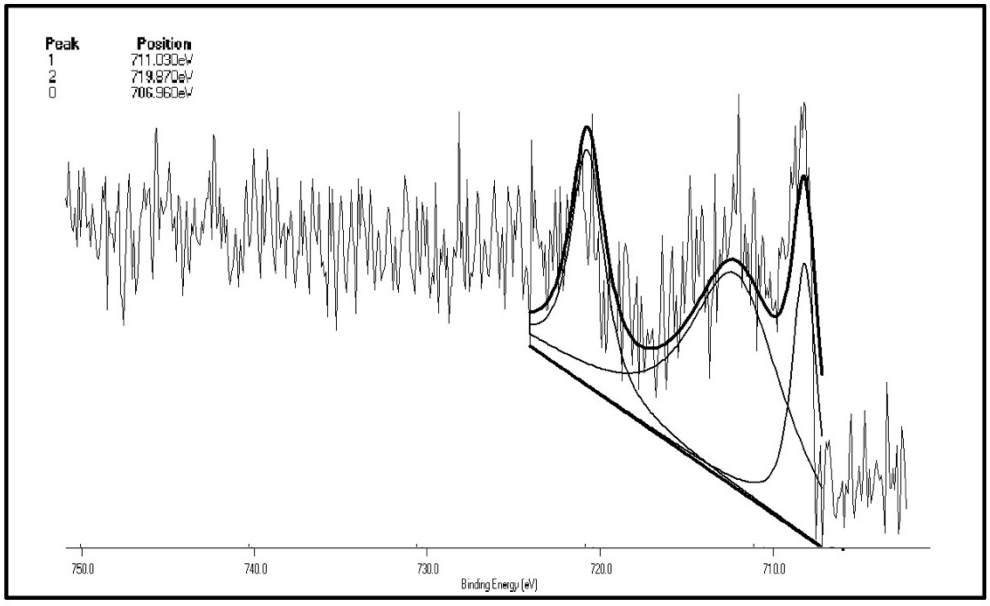

Figure 4- 13. Deconvoluted XPS spectra of N 1s (A) and Fe 2p from NC-800 (B).

4.3.5 Poison Tolerance and Durability

Methanol tolerance and durability of catalysts for ORR are critical for the practical applications to FCs. The chronoamperometric responses of methanol introduction into an O_2-saturated 0.1M KOH solution were measured for both NC-800 and commercial Pt-C catalyst. As seen in Figure 5-14, no noticeable decay of ORR current was observed on NC-800 catalyst upon the injection of 3.5 mL methanol and the current remained 96% after 2000s. In contrast, Pt-C catalyst lost 90% of ORR current immediately after the addition of methanol, due to the activity of Pt-C catalyst towards methanol oxidation and its sensitivity to the fuel crossover effect. The results here exhibited superior ORR selectivity of as-prepared NC-800 catalyst and the ability of avoiding crossover effects, which is extremely important in direct methanol fuel cells.

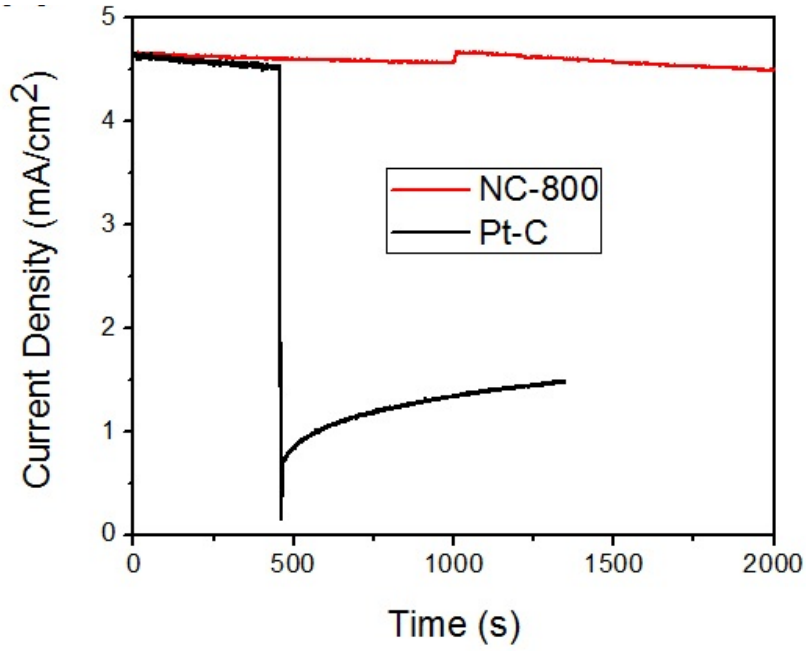

Figure 4- 14. Current-time chronoamperometric responses of NC-800 and Pt-C in oxygen saturated electrolyte followed by methanol introduction

Figure 5-15 shows the resulting chronoamperometric response for NC-800 and commercial Pt-C catalysts in 0.1 M KOH with continuous oxygen reduction. Nearly 90% of the initial current was retained at NC-800 electrode after 11 h, compared to a 25% current loss at commercial Pt-C catalyst after 7h. The remarkably enhanced stability may be attributable to the strong bonding between dopants to carbon and less likely loss of active sites. Moreover, carbon shells work as an effective protective layer for embedded iron nanoparticles, preventing iron dissolution and particle aggregation. The dramatically improved stability and methanol tolerance of NC-800 make such carbon material a feasible candidate for ORR, especially for DMFCs.

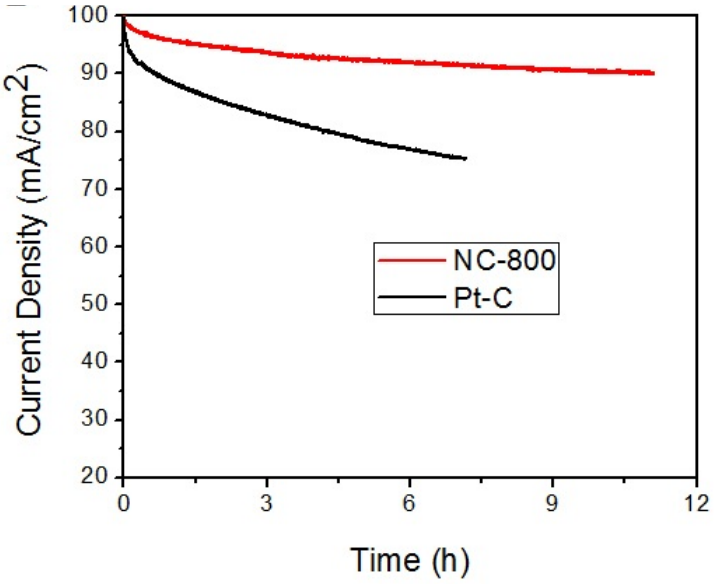

Figure 4- 15. Current-time chronoamperometric responses of NC-100 and Pt-C in a durability test

4.4 Conclusion

In summary, we have developed a facile method to convert Fe-containing MIL materials into nitrogen-doped graphitized carbon spheres with encapsulated iron nanoparticles and hierarchical porous structure in the presence of nitrogen additives. The removal of Fe_3C phase outside the carbon sphere improves the reaction activity as well as selectivity. The as-synthesized NC-800 shows an ORR activity comparable to commercial Pt-C catalyst in alkaline condition. In particular, we have demonstrated its superior stability and methanol tolerance compared to commercial Pt-C catalyst. The reported carbon material could be a potential candidate to replace costly platinum-based materials in FCs, especially DMFCs. Our strategy for converting MIL-100-Fe into ORR catalysts with specific morphology can also be extended to an enormous pool of MOF materials, which provides an avenue to develop various doped carbon materials for fuel cells and other applications.

4.5 References

1. J.-R. Li, R. J. Kuppler and H.-C. Zhou, Chem. Soc. Rev., 2009, 38, 1477-1504.

2. P. Nugent, Y. Belmabkhout, S. D. Burd, A. J. Cairns, R. Luebke, K. Forrest, T. Pham, S. Ma, B. Space, L. Wojtas, M. Eddaoudi and M. J. Zaworotko, Nature, 2013, 495, 80-84.

3. J. Lee, O. K. Farha, J. Roberts, K. A. Scheidt, S. T. Nguyen and J. T. Hupp, Chem. Soc. Rev., 2009, 38, 1450-1459.

4. S.-T. Zheng, C. Mao, T. Wu, S. Lee, P. Feng and X. Bu, J. Am. Chem. Soc. , 2012, 134, 11936-11939.

5. P. Li, Y. He, J. Guang, L. Weng, J. C.-G. Zhao, S. Xiang and B. Chen, J. Am. Chem. Soc. , 2014, 136, 547-549.

6. Z. R. Herm, B. M. Wiers, J. A. Mason, J. M. van Baten, M. R. Hudson, P. Zajdel, C. M. Brown, N. Masciocchi, R. Krishna and J. R. Long, Science, 2013, 340, 960-964.

7. P. Miao, G. Li, G. Zhang and H. Lu, Journal of Energy Chemistry, 2014, 23, 507-512.

8. H.-X. Zhang, M. Liu, X. Bu and J. Zhang, Sci. Rep., 2014, 4.

9. Y.-C. Chang and S.-L. Wang, J. Am. Chem. Soc., 2012, 134, 9848-9851.

10. B. J. Deibert and J. Li, Chem. Commun., 2014, 50, 9636-9639.

11. Y.-C. Yang and S.-L. Wang, J. Am. Chem. Soc., 2008, 130, 1146-1147.

12. J. Lin, Q. Zhang, L. Wang, X. Liu, W. Yan, T. Wu, X. Bu and P. Feng, J. Am. Chem. Soc. , 2014, 136, 4769-4779.

13. P. Horcajada, R. Gref, T. Baati, P. K. Allan, G. Maurin, P. Couvreur, G. Férey, R. E. Morris and C. Serre, Chem. Rev., 2011, 112, 1232-1268.

14. J. Gao, J. Miao, P.-Z. Li, W. Y. Teng, L. Yang, Y. Zhao, B. Liu and Q. Zhang, Chem. Commun., 2014, 50, 3786-3788.

15. S. Pullen, H. Fei, A. Orthaber, S. M. Cohen and S. Ott, J. Am. Chem. Soc. , 2013, 135, 16997-17003.

16. H. Yang, X.-W. He, F. Wang, Y. Kang and J. Zhang, J. Mater. Chem., 2012, 22, 21849-21851.

17. J. Lin, Y. Dong, Q. Zhang, D. Hu, N. Li, L. Wang, Y. Liu and T. Wu, Angew. Chem. Int. Edit., 2015, DOI: 10.1002/anie.201500659, n/a-n/a.

18. C. Mao, R. A. Kudla, F. Zuo, X. Zhao, L. J. Mueller, X. Bu and P. Feng, J. Am. Chem. Soc. , 2014, 136, 7579-7582.

19. S. Bureekaew, S. Horike, M. Higuchi, M. Mizuno, T. Kawamura, D. Tanaka, N. Yanai and S. Kitagawa, Nat. Mater., 2009, 8, 831-836.

20. G.-J. Cao, J.-D. Liu, T.-T. Zhuang, X.-H. Cai and S.-T. Zheng, Chem. Commun., 2015, 51, 2048-2051.

21. P. Li, Y. He, Y. Zhao, L. Weng, H. Wang, R. Krishna, H. Wu, W. Zhou, M. O'Keeffe, Y. Han and B. Chen, Angew. Chem. Int. Edit., 2015, 54, 574-577.

22. B. Liu, H. Shioyama, T. Akita and Q. Xu, J. Am. Chem. Soc. , 2008, 130, 5390-5391.

23. Q. Li, P. Xu, W. Gao, S. Ma, G. Zhang, R. Cao, J. Cho, H.-L. Wang and G. Wu, Adv. Mater., 2014, 26, 1378-1386.

24. D. Zhao, J.-L. Shui, L. R. Grabstanowicz, C. Chen, S. M. Commet, T. Xu, J. Lu and D.-J. Liu, Adv. Mater., 2014, 26, 1093-1097.

25. L. Zhang, Z. Su, F. Jiang, L. Yang, J. Qian, Y. Zhou, W. Li and M. Hong, Nanoscale, 2014, 6, 6590-6602.

26. P. Su, L. Jiang, J. Zhao, J. Yan, C. Li and Q. Yang, Chem. Commun., 2012, 48, 8769-8771.

27. P. Zhang, F. Sun, Z. Xiang, Z. Shen, J. Yun and D. Cao, Energy & Environmental Science, 2014, 7, 442-450.

28. A. Aijaz, N. Fujiwara and Q. Xu, J. Am. Chem. Soc. , 2014, 136, 6790-6793.

29. E. Proietti, F. Jaouen, M. Lefèvre, N. Larouche, J. Tian, J. Herranz and J.-P. Dodelet, Nat. Commun., 2011, 2, 416.

30. P. Su, H. Xiao, J. Zhao, Y. Yao, Z. Shao, C. Li and Q. Yang, Chemical Science, 2013, 4, 2941-2946.

31. J.-S. Li, S.-L. Li, Y.-J. Tang, K. Li, L. Zhou, N. Kong, Y.-Q. Lan, J.-C. Bao and Z.-H. Dai, Sci. Rep., 2014, 4.

32. U. D. o. Energy, 2013 Fuel Cell Technologies Market Report, 2014, 1-10.

33. M. K. Debe, Nature, 2012, 486, 43-51.

34. G. Gupta, D. A. Slanac, P. Kumar, J. D. Wiggins-Camacho, X. Wang, S. Swinnea, K. L. More, S. Dai, K. J. Stevenson and K. P. Johnston, Chem. Mater., 2009, 21, 4515-4526.

35. Y. Tan, C. Xu, G. Chen, N. Zheng and Q. Xie, Energy & Environmental Science, 2012, 5, 6923-6927.

36. R. Jin, Y. Yang, Y. Xing, L. Chen, S. Song and R. Jin, ACS Nano, 2014, 8, 3664-3670.

37. A. Chen and P. Holt-Hindle, Chem. Rev., 2010, 110, 3767-3804.

38. W. Zhao, S. Fan, N. Xiao, D. Liu, Y. Y. Tay, C. Yu, D. Sim, H. H. Hng, Q. Zhang, F. Boey, J. Ma, X. Zhao, H. Zhang and Q. Yan, Energy & Environmental Science, 2012, 5, 5364-5369.

39. J. Wu, A. Antaris, M. Gong and H. Dai, Adv. Mater., 2014, 26, 6151-6156.

40. Z. Chen, D. Higgins, A. Yu, L. Zhang and J. Zhang, Energy & Environmental Science, 2011, 4, 3167-3192.

41. X. Huang, H. Yu, H. Tan, J. Zhu, W. Zhang, C. Wang, J. Zhang, Y. Wang, Y. Lv, Z. Zeng, D. Liu, J. Ding, Q. Zhang, M. Srinivasan, P. M. Ajayan, H. H. Hng and Q. Yan, Adv. Funct. Mater., 2014, 24, 6516-6523.

42. H.-W. Liang, X. Zhuang, S. Brüller, X. Feng and K. Müllen, Nat. Commun., 2014, 5.

43. X. Wang, J. S. Lee, Q. Zhu, J. Liu, Y. Wang and S. Dai, Chem. Mater., 2010, 22, 2178-2180.

44. N. Ranjbar Sahraie, J. P. Paraknowitsch, C. Göbel, A. Thomas and P. Strasser, J. Am. Chem. Soc. , 2014, 136, 14486-14497.

45. M. Lefèvre, E. Proietti, F. Jaouen and J.-P. Dodelet, Science, 2009, 324, 71-74.

46. Z. Yang, X. Zhou, Z. Jin, Z. Liu, H. Nie, X. a. Chen and S. Huang, Adv. Mater., 2014, 26, 3156-3161.

47. J.-S. Li, S.-L. Li, Y.-J. Tang, M. Han, Z.-H. Dai, J.-C. Bao and Y.-Q. Lan, Chem. Commun., 2015, 51, 2710-2713.

48. G. Férey, C. Mellot-Draznieks, C. Serre, F. Millange, J. Dutour, S. Surblé and I. Margiolaki, Science, 2005, 309, 2040-2042.

49. H. T. Chung, J. H. Won and P. Zelenay, Nat. Commun., 2013, 4, 1922.

50. Y. Hu, J. O. Jensen, W. Zhang, L. N. Cleemann, W. Xing, N. J. Bjerrum and Q. Li, Angew. Chem. Int. Edit., 2014, 53, 3675-3679.

51. Z. Wen, S. Ci, F. Zhang, X. Feng, S. Cui, S. Mao, S. Luo, Z. He and J. Chen, Adv. Mater., 2012, 24, 1399-1404.

52. D. Deng, L. Yu, X. Chen, G. Wang, L. Jin, X. Pan, J. Deng, G. Sun and X. Bao, Angew. Chem. Int. Edit., 2013, 52, 371-375.

53. J.-S. Lee, G. S. Park, S. T. Kim, M. Liu and J. Cho, Angew. Chem. Int. Edit., 2013, 52, 1026-1030.

54. T.-N. Ye, L.-B. Lv, X.-H. Li, M. Xu and J.-S. Chen, Angew. Chem. Int. Edit., 2014, 53, 6905-6909.

55. D. Zhao, J.-L. Shui, C. Chen, X. Chen, B. M. Reprogle, D. Wang and D.-J. Liu, Chemical Science, 2012, 3, 3200-3205.

56. A. Kong, B. Dong, X. Zhu, Y. Kong, J. Zhang and Y. Shan, Chemistry – A European Journal, 2013, 19, 16170-16175.

57. W. He, C. Jiang, J. Wang and L. Lu, Angew. Chem. Int. Edit., 2014, 53, 9503-9507.

58. G. Wu, K. L. More, C. M. Johnston and P. Zelenay, Science, 2011, 332, 443-447.

59. A. Velázquez-Palenzuela, L. Zhang, L. Wang, P. L. s. Cabot, E. Brillas, K. Tsay and J. Zhang, The Journal of Physical Chemistry C, 2011, 115, 12929-12940.

60. J. W. Yoon, Y.-K. Seo, Y. K. Hwang, J.-S. Chang, H. Leclerc, S. Wuttke, P. Bazin, A. Vimont, M. Daturi, E. Bloch, P. L. Llewellyn, C. Serre, P. Horcajada, J.-M. Grenèche, A. E. Rodrigues and G. Férey, Angew. Chem. Int. Edit., 2010, 49, 5949-5952.